EVOLUTION OF METHODOLOGY FOR OBTAINING ^{1}H MAGNETIC RESONANCE SPECTRA OF THYROID NODULES *IN VIVO*

BY

Scott B. King

A Thesis
Submitted to the Faculty of Graduate Studies
In Partial Fulfillment of the Requirements
For the Degree of

DOCTOR OF PHILOSOPHY

Department of Physics and Astronomy
University of Manitoba
Winnipeg, Manitoba, Canada

and

Institute for Biodiagnostics
National Research Council of Canada
Winnipeg, Manitoba, Canada

THE UNIVERSITY OF MANITOBA

FACULTY OF GRADUATE STUDIES

*****

COPYRIGHT PERMISSION PAGE

Evolution of Methodology for Obtaining ^{1}H Magnetic Resonance Spectra of Thyroid Nodules *in vivo*

BY

Scott B. King

A Thesis/Practicum submitted to the Faculty of Graduate Studies of The University of Manitoba in partial fulfillment of the requirements of the degree of Doctor of Philosophy

ABSTRACT

Thyroid nodules are common (up to 10% of the population), but only a small fraction (<5%) are found to be malignant. Cytology of fine needle aspiration biopsies (FNAB), the standard initial diagnostic modality for thyroid cancer, is unable to discriminate benign from malignant follicular thyroid nodules, which are recognized only by pathologic evidence of capsular or vascular invasion. Therefore, many thyroid surgeries are performed simply to exclude a diagnosis of malignancy. In the benign case, the thyroid gland is removed solely for diagnostic purposes. *Ex vivo* proton MRS on resected tissue as well as on FNAB has been reported to accurately discriminate malignant thyroid nodules from normal tissue. The ability to localize and differentiate normal or benign tissue from their malignant counterpart with MRS *in vivo* would provide a non-invasive and non-subjective diagnosis, reduce surgery for nonmalignant glands, and aid in the clinical management of thyroid nodules.

This thesis describes methods for obtaining ^{1}H MR spectra *in vivo* from normal thyroid and thyroid nodules. Many technical barriers, such as low signal-to-noise, poor resolution, poor localization, and magnetic susceptibility and motion-related artifacts, had to be overcome.

The research began by demonstrating that the poor SNR, resolution and/or water suppression of ^{1}H MR spectra of the thyroid at magnetic fields of 1.5T would not allow for classification of thyroid spectra *in vivo*.

Considerable improvement in SNR and resolution was apparent at a magnetic field of 3T compared to results at 1.5T. Optimizing the slice-selection order, as well as automatic localized shimming and frequency/phase correction, were necessary for achieving

optimal spectral resolution. Using large spoiler gradients, with a large difference between TE and TM gradient areas, minimized the amount of contamination present in the spectra from unwanted coherences. The combined use of STEAM localization and a multi-ring surface coil offered the SNR advantages of a surface coil with homogeneous volume localization, comparable to that of volume coils. With an appropriate multi-ring surface-coil design and optimal placement with respect to the thyroid or tumor, sensitivity to lipid contamination from subcutaneous neck fat can be reduced. Together, the multi-ring surface coil characteristics allowed high-quality spectra to be obtained.

In vivo ^{1}H MR spectra from normal thyroid at 3T had spectral characteristics similar to those of *ex vivo* biopsy spectra at 8.5T. When the same criteria used for classification of the *ex vivo* spectra were applied to the *in vivo* spectra obtained from normal volunteers, all were classified as "normal". Similarly for the benign cases, the 1.7ppm/0.9ppm and the 2.0ppm/0.9ppm metabolite peak height ratios were greater that 1.1 and 1.12, respectively, which would also classify these spectra as "normal". Therefore, the ^{1}H MR spectra obtained from normal thyroid as well as thyroid nodules show that there is potential for classification of thyroid tumors *in vivo* using the previously described 3T methods.

This thesis is dedicated to my father, Kenneth Lawrence King (1940-1998)

I love you and miss you Dad

ACKNOWLEDGEMENTS

First, I would like to thank everyone at the Institute for Biodiagnosics, for their support, friendship and good times. Specifically, I thank: Dr. Jonathan Sharp for his guidance and teaching, from the beginning to the end, Dr. Lawrence Ryner for his continued guidance and advice, and Dr. Boguslaw Tomanek for his friendship and many enlightening discussions.

I would also like to thank the members of my advisory committee – Dr. John Saunders, Dr. Norm Davison, Dr. William Leslie, and my external advisor Dr. Brian Rutt, for guiding my research and seeing me through to the end.

I am very grateful to my medical collaborator, Dr. K. Riese, for providing me with patients for my study. Without him, this research would not have gone as far as it did. I also thank the St. Boniface MRI Center for allowing me to carry out research on the 1.5T system.

To my supervisor, Dr. Ian C.P. Smith, I am forever grateful. He always looked out for me and my career and without his generosity, I would not have the great opportunities that I have today.

I also thank my friends: Pauline for all her help and support, Phil for his encouragement, Drs. Tedros Bezebeh and Lanette Friesen for being such good friends to me and supporting me during the rough times. To my best friends forever, Eduardo, my office mate and workout buddy, who gave me the confidence to carry on, Mike and Jamie for being there for me since high school, your friendships are non-replaceable.

Most of all, I especially thank my family: Jenny, Sean, Tricia, Jazzmin, and my mother and father in law for all these years of support. My sister Stacey, and my auntie Linda, my number one fan. My brother Todd, DeeDee, and Robbie. I am sorry for not seeing you enough, I will miss you Bro. My Mom and Dad, who taught me the drive and ambition to do what ever I wanted. Without their sacrifices I would not be here today. I love you both very much and owe this to you both. Dad, you were my best friend in the world. My daughter Steffany, my little girl, who I am so proud to say, is the nicest and sweetest girl in the world, and the love of my life. Finally, my wife Kristen, my soul mate, who sacrificed so much for me, we made it. Without you I could not have done this. I love you, more than you could imagine.

TABLE OF CONTENTS

LIST OF FIGURES

LIST OF TABLES

GLOSSARY

Adiabatic RF pulse	produces a uniform flip angle in the presence of B_1 inhomogeneity
B_0	static magnetic field of the magnet
B_1	RF magnetic field produced by an RF coil
CP	Circularly-Polarized – equivalent to quadrature
FFT	Fast Fourier Transform
FID	Free Induction Decay
FOV	Field-Of-View
IDL	Interactive Data Language
Isocenter	magnetic center of the magnet defined by the magnetic field gradients
Isochromat	single frequency component
MRI	Magnetic Resonance Imaging
MRS	Magnetic Resonance Spectroscopy
PRESS	Point RESolved Spectroscopy
Quadrature	orthogonal transmission/reception using two RF coils 90° out of phase
RF	RadioFrequency
SAR	Specific Absorption Rate
SNR	Signal-to-Noise Ratio
STEAM	Stimulated Echo Acquisition Mode
TE	Echo Time
TM	Mixing Time
TR	Repetition Time
T_1	spin-lattice relaxation time
T_2	spin-spin relaxation time
T/R	Transmit/Receive
VOI	Volume-Of-Interest
WS	Water Suppression

INTRODUCTION

Cancer is one of the leading causes of death in the world today. The word "cancer" is one of the most feared in our culture, which is why many cancer patients, along with their family and friends, experience extreme emotional anguish.

Thyroid tumors are found in up to 10% of the population, yet less than 5% of these prove to be malignant. Therefore, thyroid cancer is not one of the leading causes of cancer deaths. Unfortunately, there is one form of malignant thyroid tumor that is cytologically indistinguishable from its benign counterpart on FNA, leading to many unnecessary and traumatic surgeries each year.

Nuclear magnetic resonance spectroscopy has the ability to acquire quantitative information about the chemical composition of tissues. It is believed that ^{1}H magnetic resonance spectroscopy (MRS) can detect biochemical changes in the cells of tumors before histological changes. With this hypothesis, *ex vivo* ^{1}H MRS on thyroid biopsies has been shown to differentiate normal from malignant thyroid tumors with close to 100% accuracy.

In this thesis, methods will be developed to obtain high quality ^{1}H MR spectra *in vivo* from normal thyroid and thyroid nodules, overcoming many of the present difficulties such as low signal-to-noise, poor resolution, poor localization, and artifacts related to magnetic susceptibility and motion. Spectra obtained from thyroid nodules will be compared to those obtained from normal thyroids, and the potential for *in vivo* classification will be evaluated. The advantage of the *in vivo* method is that it is non-invasive, requiring no surgical procedures, and is non-subjective, explores the entire nodule, and thereby eliminates the sampling problem of conventional histopathology.

Chapter 1

MAGNETIC RESONANCE THEORY, TECHNIQUES AND APPARATUS

1.1 Nuclear Magnetic Resonance – A Quantum Description

There exists a quantum mechanical property of atomic nuclei known as *spin*, a vector quantity given the symbol **I**. Many nuclei possess a non-zero spin and therefore have a resultant total angular momentum $\mathbf{J} = \hbar\mathbf{I}$ and a magnetic moment $\boldsymbol{\mu}$ in parallel, where $\hbar = h/2\pi$ and h is Planck's constant. They are related through a constant of proportionality γ, the magnetogyric ratio, such that,

$$\boldsymbol{\mu} = \gamma\hbar\mathbf{I}. \qquad [1.1]$$

When this nucleus is placed in an external static magnetic field, $\mathbf{B}_0 = B_0\,\hat{\mathbf{z}}$, the nucleus experiences what is known as the Zeeman interaction. The interaction energy is found from the quantum energy operator, the Hamiltonian (H),

$$\mathbf{H} = -\boldsymbol{\mu} \bullet B_0 = -\gamma\hbar B_0 I_z. \qquad [1.2]$$

Because the nucleus only occupies a discrete number of spin states, eigenvalues of the Hamiltonian take on discrete values. These energy levels are said to be quantized, multiples of the eigenvalues (m) of I_z. The allowed energy levels for the nucleus are

$$\mathbf{E} = -\gamma\hbar B_0 m, \qquad m = I, I\text{-}1, \ldots, -I. \qquad [1.3]$$

In the case of a spin ½ nucleus such as ^{1}H, there are two possible energy levels separated by an energy,

$$\Delta E = \gamma\hbar B_0. \qquad [1.4]$$

Transitions between spin states is allowed only for a change in the magnetic quantum number of $\Delta m = \pm 1$, and therefore the energy of such allowed transitions is given by Eq. [1.4]. It can be shown quantum mechanically (1) that such transitions require a time dependent magnetic field ($\mathbf{B_1}$), directed perpendicular to the static field and oscillating at a frequency (ω_0),

$$\omega_0 = \frac{\Delta E}{\hbar} = \gamma B_0 . \qquad [1.5]$$

This Larmor equation describes what is referred to as the nuclear magnetic resonance condition.

1.2 Nuclear Magnetic Resonance – A Classical Description

There are two approaches one can take in describing nuclear magnetization and excitation/detection of the NMR signal – using quantum or classical mechanics. The classical picture is able to explain all remaining aspects of the work herein and therefore will be used throughout.

1.2.1 Nuclei in a Static Magnetic Field: Nuclear Magnetization

Classically, a particle possessing a magnetic moment placed in a magnetic field will experience a torque. This torque will cause a precession of the magnetic moment about the field (for example, a spinning top under the influence of gravity). This is depicted in Fig. 1.1a for a single nucleus of magnetic moment, μ.

Although classical NMR can be described for a single nucleus, real life macroscopic samples require an ensemble picture that describes populations of spins in specific spin

states. In the case of a macroscopic sample of spin ½ nuclei in a static magnetic field, the two possible spin states or populations are the spin-up (N_+) (spins aligned with the $\mathbf{B_0}$ field) and spin-down (N_-) states (spins anti-aligned with the $\mathbf{B_0}$ field). The distribution of spins in these states is governed by the Boltzmann distribution that depends on the energy difference between states, the temperature (T) of the surrounding environment and the Boltzmann constant k, such that,

$$\frac{N_-}{N_+} = \exp\left(\frac{\Delta E}{kT}\right) \approx 1 + \frac{2\mu B_0}{kT} \quad for\, \Delta E << kT\,. \qquad [1.6]$$

At room temperature and a polarizing field of 1 Tesla, there is an excess number of spins in lower energy spin-up state of ~ 10^{-6}, giving rise to a small, net magnetization, $M = \sum_{i=1}^{N} \mu_i$, parallel to $\mathbf{B_0}$ (Fig. 1.1b).

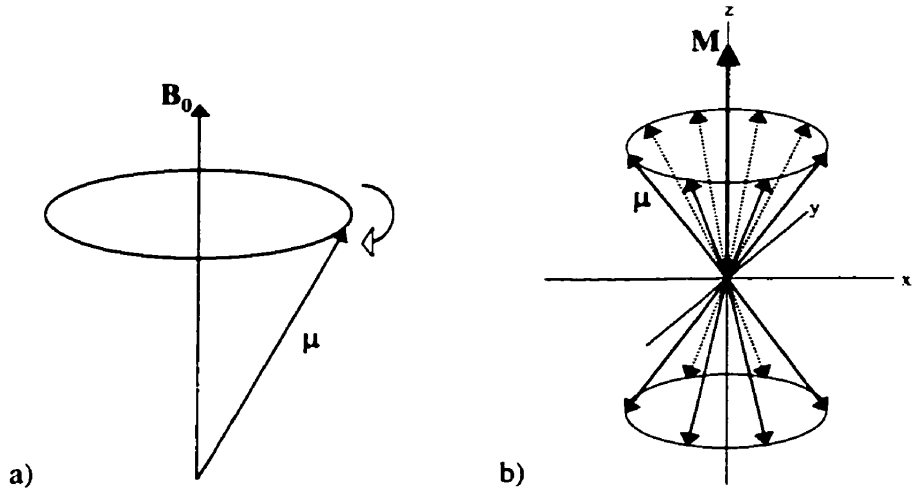

Figure 1.1 (a) Precession of a magnetic moment μ about a magnetic field B0, and (b) precession of an ensemble of spin magnetic moments giving rise to a net magnetic moment M.

The equilibrium magnitude of this magnetization (M_0) is given by the Curie-Langevin formula,

$$M_0 = \frac{\gamma^2 \hbar^2 B_0 N_0}{3kT} I(I+1) = \chi B_0, \qquad [1.7]$$

where N_0 is the number of nuclei per 1 m^3 of the sample. The sample magnetic susceptibility, χ, is a constant dependent on the temperature and composition of the sample.

1.2.2 NMR Excitation by an Alternating Magnetic Field

1.2.2.1 The Laboratory Frame of Reference

In order to describe NMR excitation, we must now consider the equation of motion of the magnetization vector in a magnetic field **B**,

$$\frac{d}{dt}\mathbf{M} = \gamma \mathbf{M} \times \mathbf{B}. \qquad [1.8]$$

As stated earlier, the magnetic resonance condition occurs when an external oscillating magnetic field is applied orthogonal (or transverse) to the static magnetic field. Consider such a $\mathbf{B}_1$ field linearly polarized and oscillating at the Larmor frequency (ω_0) in the x-direction. It can be broken down into two circularly-polarized components; one rotating clockwise or left-circularly polarized ($\mathbf{B}_L$) and the other rotating counter-clockwise or right-circularly polarized ($\mathbf{B}_R$) as depicted in Fig. 1.2.

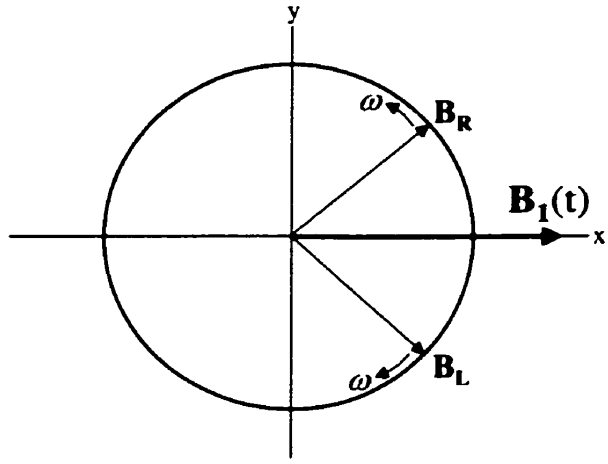

Figure 1.2 Decomposition of a linearly polarized, oscillating field into two circularly polarized components.

The rotating fields are denoted by

$$\begin{aligned} \mathbf{B}_R &= B_1[\mathbf{i}\cos(\omega t)+\mathbf{j}\sin(\omega t)] \\ \mathbf{B}_L &= B_1[\mathbf{i}\cos(\omega t)-\mathbf{j}\sin(\omega t)] \end{aligned} \quad [1.9]$$

The component rotating in the same sense as the nuclear spin precession ($\mathbf{B}_L$) will be responsible for the resonance condition stated earlier when $\omega = \omega_0$. Note that in this case, the counter-rotating component rotates at -2ω off resonance and, as will be shown later, can be ignored. Therefore, the effective B_1 field is then given as

$$\mathbf{B}_1(t) = B_1[\mathbf{i}\cos(\omega t)-\mathbf{j}\sin(\omega t)]. \quad [1.10]$$

It is worth noting that as seen in Fig. 1.2, the effective B_1 field available for resonant excitation is $1/\sqrt{2}$ times smaller than the input B_1 field and consequently ½ the input power is lost. An input B_1 field circularly polarized in the correct sense can be produced from two-perpendicular linearly polarized fields 90° out of phase. This allows the full input power to be used for excitation. Applying the RF B_1 field to the magnetization in the static B_0 field, the equation of motion becomes

$$\frac{d}{dt}\mathbf{M} = \gamma \mathbf{M} \times [\mathbf{B}_0 + \mathbf{B}_1(t)] = \gamma \mathbf{M} \times \mathbf{B}_{eff}. \qquad [1.11]$$

When the spin system is disturbed from its thermal equilibrium state by the B_1 field, a process known as spin-lattice or longitudinal (T_1) relaxation occurs, by which magnetization is restored to its equilibrium position along the polarization, z-axis. This occurs from spins interacting with their surroundings. This process is described by

$$\frac{d}{dt}M_z = -\frac{(M_z - M_0)}{T_1}, \qquad [1.12]$$

where T_1 is known as the longitudinal relaxation time.

The recovery of z-magnetization is accompanied by destruction of the transverse magnetization, occurring due to spins interacting with each other, known as spin-spin or transverse (T_2) relaxation. This relaxation effect on the transverse components of magnetization is described by

$$\frac{d}{dt}M_{x,y} = -\frac{M_{x,y}}{T_2}, \qquad [1.13]$$

where T_2 is known as the transverse relaxation time.

Combining Eq. [1.10], [1.11], [1.12], and [1.13] yields a set of differential equations, known as the Bloch equations (2), which describe the magnetization under influence of a static B_0 field, a time dependent RF B_1 field and relaxation effects (3),

$$\begin{aligned}
\frac{d}{dt}M_x &= \gamma[M_y B_0 + M_z B_1 \sin(\omega t)] - \frac{M_x}{T_2}, \\
\frac{d}{dt}M_y &= \gamma[-M_x B_0 + M_z B_1 \cos(\omega t)] - \frac{M_y}{T_2}, \qquad [1.14] \\
\frac{d}{dt}M_z &= \gamma[-M_y B_1 \cos(\omega t) - M_x B_1 \sin(\omega t)] - \frac{(M_z - M_0)}{T_1}.
\end{aligned}$$

The magnetization response to most RF pulse sequences can be described by numerically solving the Bloch equations.

1.2.2.2 The Rotating Frame of Reference

The effect of the effective magnetic field on the magnetization can be explained more simply by making a transformation from the laboratory (stationary) frame to a rotating frame of reference. Let us consider a reference frame that rotates about the z-axis with the same angular velocity as the $B_1(t)$ field, ω. In this rotating frame, it can be shown that the effective magnetic field experienced by the magnetization vector is given by

$$\mathbf{B}_{eff} = \left(B_0 - \frac{\omega}{\gamma} \right) \mathbf{k} + B_1 \mathbf{j}, \qquad [1.15]$$

where the rotating B_1 field is now stationary and, without loss of generality, chosen to be along the y-axis. It can be seen that when the frequency of the B_1 field (ω) is equal to the Larmor frequency ($\omega_0 = \gamma B_0$), there is zero effective magnetic field in the z-direction, and the magnetization, which always precesses about the effective field, precesses about the B_1 field for the duration (t_p) of the RF B_1 pulse. This 'excitation' is the classical description of the resonance condition. The angle through which the magnetization rotates towards the transverse plane is given by

$$\theta = \gamma B_1 t_p. \qquad [1.16]$$

Using the rotating frame description, numerical solutions of the Bloch equations, for the magnetization response to most RF pulse sequences, are easily described by performing incremental spin rotations about the effective B-field. This method is

computationally much simpler than direct (laboratory frame) solutions, and is also a reasonable approximation since most NMR systems now use digital RF electronics (for example Lawry 1989(4)) (see Ch. 3, Section 3.2.4).

1.2.2.3 The 90° Pulse

With the initial magnetization parallel to $\mathbf{B_0}$ (+z-direction), if the B_1-field is applied along the +x-axis with the Larmor frequency for a time t_{90}, such that the magnetization rotates by 90°, the magnetization will then lie along the +y-axis (Fig. 1.3). This is referred as a 90° pulse. Transverse relaxation (T_2 relaxation) then causes spins to dephase in the transverse plane, and the transverse magnetization reduces to zero from its initial value M_0. Longitudinal relaxation (T_1 relaxation) acts to restore the z-magnetization back to its equilibrium value M_0, with a $T_1 \geq T_2$.

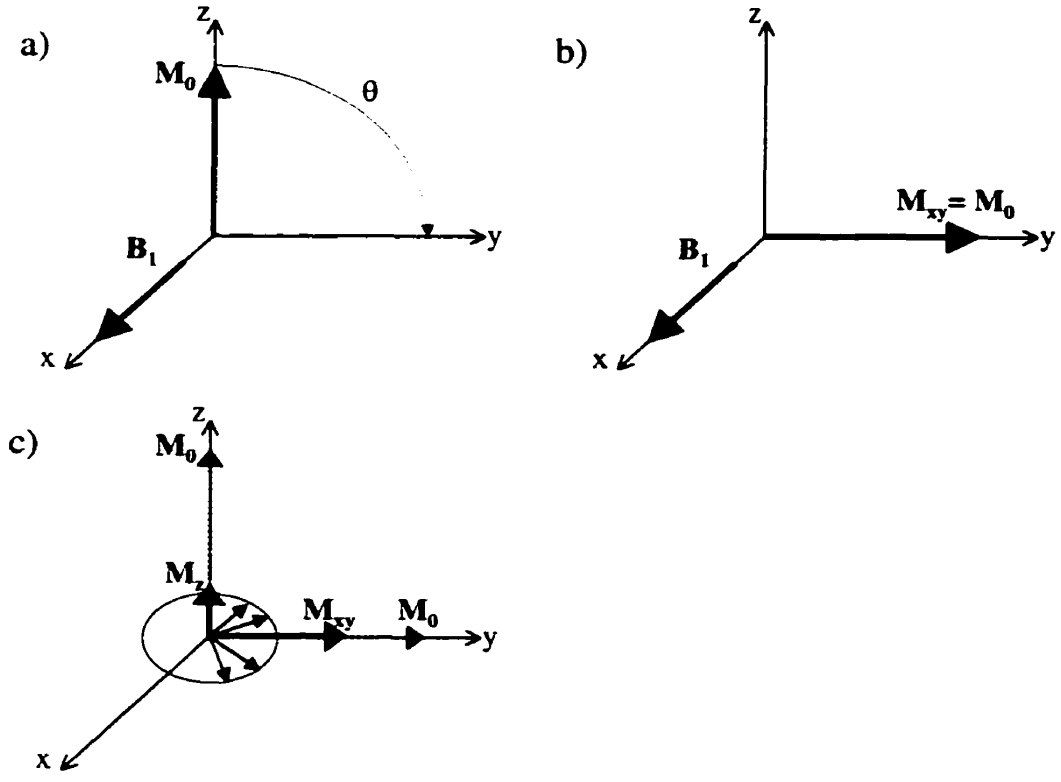

Figure 1.3 Response to a 90° flip for single-isochromat magnetization. a) Initial magnetization M_0, and applied B_1-field direction. b) Transverse magnetization after the B_1-field is applied for duration t_{90}. c) Dephasing of spin components causing T_2-relaxation and hence a reduced transverse magnetization ($\mathbf{M}_{xy}$) with corresponding z-magnetization ($\mathbf{M}_z$) returning to its equilibrium value M_0 due to T_1-relaxation.

The observed transverse relaxation time is shortened if B_0 inhomogeneities are present within the sample. Much like T_2 relaxation, the variation in the local B_0 field causes variation in the precessional frequency of the isochromats, in this case, depending on their position within the sample. Therefore, the effective transverse relaxation time (composed of both T_2 relaxation and the effects of B_0 inhomogeneity) is labelled T_2^*, such that $T_2^* \leq T_2$. The decay of the transverse magnetization is exploited in several ways for both MR imaging and spectroscopy.

1.2.2.4 The Spin Echo

A spin echo, first observed by Hahn in 1950 (5), occurs when a 90° pulse is followed by one or more 180° pulses (twice the length or twice the RF power of the 90° pulse). After a 90° pulse in an inhomogeneous B_0-field, the spins of a single isochromat at different positions will experience T_2^* relaxation, causing the spins to dephase, with some spins precessing slightly faster than ω_0 and some precessing slightly slower than ω_0. This loss of phase coherence is reversible by applying a 180° pulse after a time τ, causing refocusing of transverse relaxation at time 2τ, known as a spin-echo (5). This is shown schematically in Fig. 1.4. In (a), after the 90° pulse along the +x-axis, the magnetization is then on the +y-axis. In (b), the spins dephase due to B_0-field inhomogeneity. Some spins will precess faster (A) than ω_0 and some will precess slower (B) than ω_0, depending on whether they are located in an inhomogeneous field with magnitude that is larger or smaller than B_0 respectively. In (c), a 180° pulse is applied again along the +x-axis after a time τ, flipping the spins as shown. Because each spin remains in the same position and therefore experiences the same effective B_0-field, they retain their precession speed relative to ω_0 as the arrows in (c) indicate. Therefore, after an equal time τ after the 180° pulse (or 2τ after the 90° pulse), the spins refocus onto the –y-axis, forming the spin-echo.

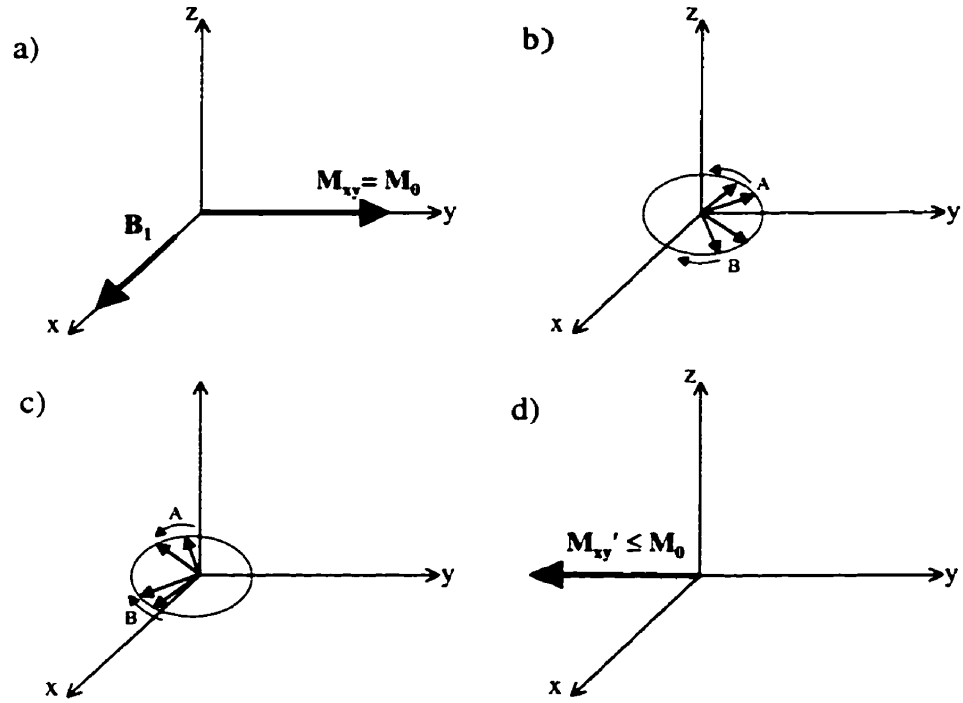

Figure 1.4 Response to a spin-echo pulse sequence for single-isochromat magnetization; (a) after 90° pulse along the +x-axis, (b) during loss of phase coherence over time τ due to B_0 inhomogeneity, (c) immediately after the 180° pulse, and (d) after a time τ after the 180° pulse resulting in a spin-echo with an echo time of TE = 2τ from the first 90° pulse, with amplitude M_{xy}' reduced by T_2-relaxation effects.

1.2.2.5 The Stimulated Echo

A stimulated echo is the result of a sequence of three consecutive 90° RF pulses. The evolution of the magnetization vector in the rotating frame is depicted in Fig. 1.5. In (a), after the 90° pulse along the +x-axis, the magnetization is then on the +y-axis. In (b), the spins dephase due to B_0-field inhomogeneity. In (c), a 90° pulse is applied again along the +x-axis after a time TE/2, causing the x-y plane of spins to flip into the x-z plane. B_0 inhomogeneity during the TM period between the second and third RF pulses causes complete dephasing of the transverse magnetization leaving only a z-

magnetization (d). It is easily shown that ½ of the available magnetization is lost during this period. During this TM period, the z-magnetization experiences only T_1-relaxation. In (e), a third 90° RF pulse then rotates this z-magnetization into the transverse plane. With identical B_0 inhomogeneity to the first TE/2 period, this transverse magnetization forms a stimulated echo at a time TE/2 from the third 90° pulse. Of course, the resultant magnetization is reduced to less than ½ the original magnetization by T_2-relaxation during the TE/2 periods.

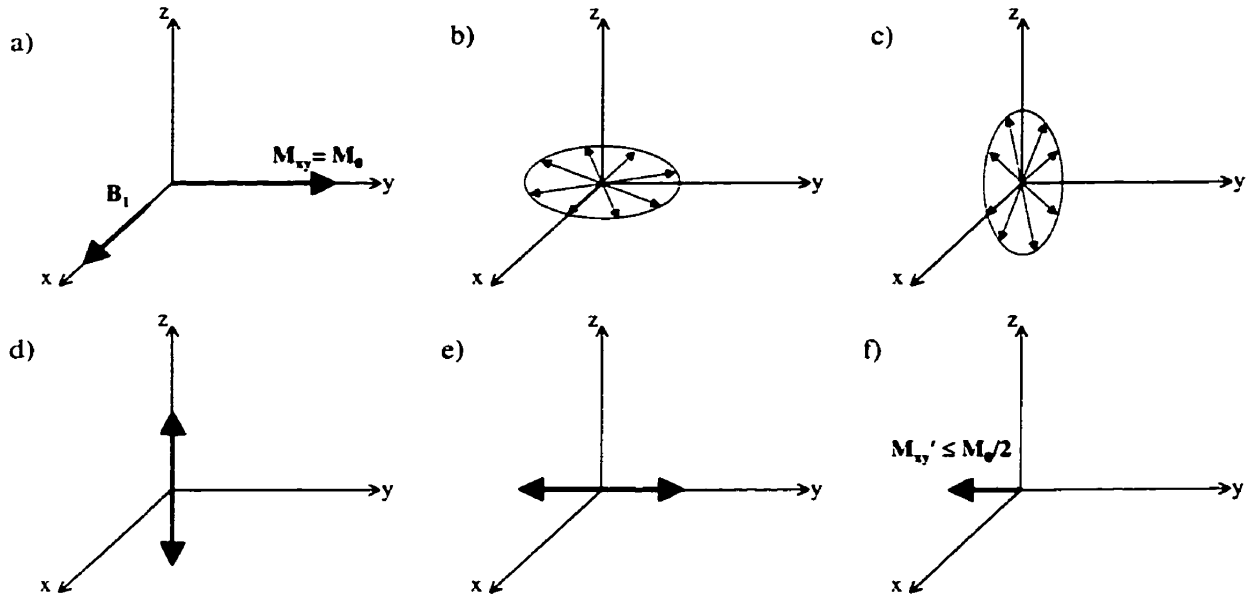

Figure 1.5 Response to a stimulated-echo pulse sequence for single-isochromat magnetization; (a) after 90° pulse along the +x-axis, (b) during loss of phase coherence over time TE/2 due to B_0 inhomogeneity, (c) immediately after the plane rotation of the second 90° pulse, (d) during a time TM, complete dephasing leaves only z-magnetization, (e) after the third 90° pulse which flips the remaining $M_0/2$ magnetization into the transverse plane, (f) the transverse magnetization experiences a B_0 inhomogeneity for a time TE/2 to form the stimulated echo, with amplitude M_{xy}' reduced by T_2-relaxation effects.

1.2.2.6 FID's and Echoes Created from Multi-Pulse Experiments

Any sequence of N- RF pulses, will produce a train of FID's, echoes and stimulated echoes created, representing what are called coherences, with amplitudes dependent on, among other things, the flip angles of the N-pulses. An example of a sequence of three RF pulses with flip angles α_1, α_2, and α_3 is shown in Fig. 1.6. In this illustration, it is assumed that some B_0 inhomogeneity is present that causes each coherence to decay to zero with a small time constant. For each RF pulse, there will be an FID created. Spin echoes will be created from the first and second pulses (SE1-2), the second and third pulses (SE2-3) and the first and third (SE1-3). In addition, the third pulse will create an echo of the spin echo created from the first two RF pulses, resulting in a double spin echo (SEE1-2-3). Finally, a stimulated echo (STE1-2-3) is formed from all three pulses.

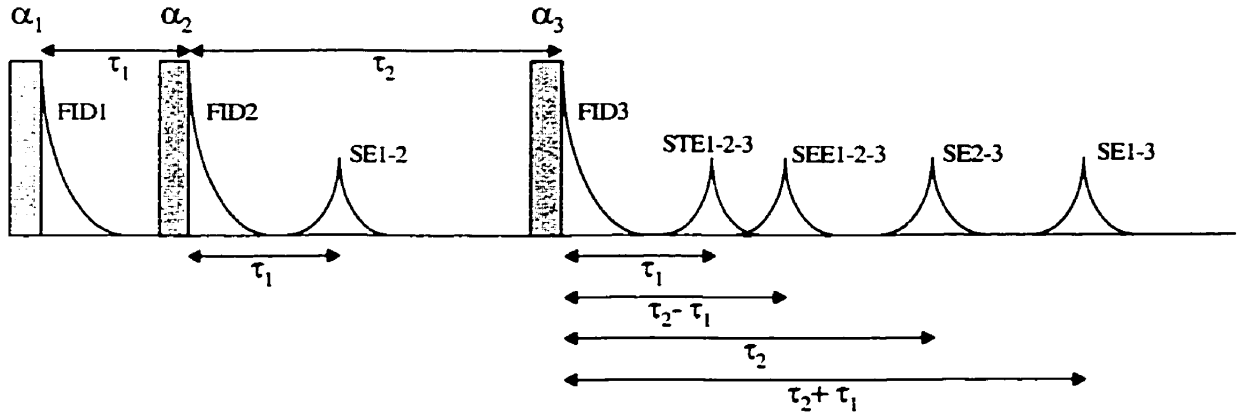

Figure 1.6 Coherences created from a sequence consisting of three RF pulses; three FID's, three spin-echoes, one double spin-echo and one stimulated echo.

1.2.3 Detection of the NMR Signal – The Free Induction Decay (FID)

For the same reason that the B_1-field has to be applied perpendicular to the B_0-field for excitation, only a RF coil with a transverse B_1-field can detect the excited magnetization. Regardless of which experiment is performed, magnetization must be rotated into the transverse plane to be detected, such as the simple 90° pulse described previously, where the magnetization is flipped along the +y-axis. Consider, without loss of generality, the case of only one isochromat resonating at the Larmor frequency. Actual detection of magnetization is done in the laboratory frame, therefore, in this frame of reference, the resulting magnetization will precess about the B_0 field at the Larmor frequency.

If we now place an RF coil, with its B_1-field linearly polarized in the x-direction, Faraday's law states that a current and hence voltage is induced in the RF coil, proportional to the magnitude of magnetization, but with opposite phase. Therefore, with all magnetization originally along the +y-axis, zero current will flow in the RF coil. A short time later, when the magnetization points along the +x-axis, a maximum negative voltage will be induced (the actual sign depends on the polarity of the cable used to propagate the signal). When the magnetization precesses to the –y-axis, again zero voltage is induced. Finally, with the magnetization pointing along the –x-axis, a maximum positive voltage is induced. This sinusoidal output voltage from the coil would continue indefinitely, except that the relaxation processes cause the magnitude of the transverse magnetization to decay as it precesses around $\mathbf{B_0}$. Therefore, this transverse magnetization from **freely** precessing spins, **induces** a voltage in the RF coil

that **decays** due to relaxation processes and hence produces what is known as a **free induction decay (FID)**.

1.3 Magnetic Resonance Spectroscopy (MRS)

The FID contains time domain data representing the superposition of NMR signals received from all metabolites. In order to obtain spectroscopic resonant frequency information for the metabolites, the time domain data $f(t)$ are converted to the frequency domain $F(\omega)$. Because the FID data are discretely sampled, a discrete Fourier transform (FT) is performed. The Fourier transform is a mathematical tool that determines the Fourier coefficients $A_n(\omega)$, for the n frequency harmonics, that is, $\sin(n\omega t)$ and $\cos(n\omega t)$, present in the FID. The Fourier transform is described mathematically as

$$F(\omega) = \frac{1}{N} \sum_{n=0}^{n=N-1} f(t) \exp[-j\omega t], \qquad [1.17]$$

where $t = n\,\Delta t$ are the sampled time points of the FID. The time domain data is recovered from the frequency domain using the inverse Fourier transform,

$$f(t) = \sum_{n=0}^{n=N-1} F(\omega) \exp[j\omega t], \qquad [1.18]$$

where $\omega = n\,\Delta\omega$ are the discrete points of the frequency spectrum. The resolution of the spectrum is related to the sampling interval as,

$$\Delta\omega = \frac{1}{N\,\Delta t}, \qquad [1.19]$$

where the sampling interval is determined by the highest frequency present in the sampled data (by the Nyquist theorem).

If there are 2^N points in a data set, then the FT requires N^2 complex multiplications. In practice, $f(t)$ and the exponential term can be decomposed such that the successive

doubling Fast Fourier Transform (FFT) method can be employed (6). The FFT only requires $N\log_2 N$ operations. For an FID consisting of 8192 points (4096 real and 4096 imaginary), the FFT will perform the time-to-frequency domain transformation 600 times faster than the regular FT.

The NMR spectrum consists of many peaks or resonances superimposed on a baseline of noise. Although a spectrum consists of signals from a particular nucleus, say ^1H, hundreds of resonances exist over a range of frequencies. The height of any particular resonant peak is determined by its relative concentration and the degree of relaxation present (T_2, T_2^*, T_1). A particular metabolite's frequency position is determined by its chemical environment. A nucleus is surrounded by an electron cloud that acts to shield the nucleus from the applied magnetic field B_0 (7). This shielding gives rise to an effective local magnetic field given by $B = B_0(1-\sigma)$, where σ is referred to as the shielding constant. The frequency of the resonance then changes from ν_0 to $\nu = (\gamma/2\pi)\, B_0(1-\sigma)$. The chemical shift reference, ν_0, is usually chosen to be the frequency of a known resonance. Chemical shift is often expressed in parts-per-million (ppm), $\delta = 10^6(\nu-\nu_0)/\nu_0$, which is independent of B_0 field strength. As the B_0 field is increased, the distances between the peaks in the spectrum will increase (in frequency but not in ppm), resulting in an apparent improvement in resolution. Unfortunately, a higher B_0 field is often accompanied by increased B_0 inhomogeneity and hence larger linewidths, leading to a decrease in resolution. Fortunately, the higher B_0 field also brings increased SNR by virtue of increased magnetization (M_0) according to the Boltzmann distribution.

A resonance peak can also be split to form a doublet, triplet, etc., by spin-spin coupling or J-coupling. This refers to the interaction of the magnetic moment of one nucleus of a metabolite with that of a nearby nucleus of the same molecule. This splitting is seen in high resolution spectra, but for *in vivo* spectroscopy, B_0 inhomogeneity usually broadens resonance line shapes so much that this effect is masked.

Interpretation of a spectrum is strongly dependent on SNR and resolution. From Eq. [1.19], it can be seen that with a fixed sampling interval Δt, the resolution of a spectrum can be improved by increasing the total number of points in the FID. Because an FID usually decays to zero long before the last data point, zeroes can be added to the FID (usually an integer multiple of the original number of points), thereby increasing the total number of points without increasing acquisition time and usually resulting in an apparent improvement in spectral resolution. The apparent SNR can also be improved by noise reduction in the time domain. Because the FID will have decayed to noise level long before the last data point and an FID is in general exponential in shape, an exponential weighting function can be applied to the FID to reduce the total noise level in the spectrum.

1.4 Frequency Selective RF Pulses and Slice Selection

1.4.1 Frequency Selective RF Pulses

As described previously, NMR excitation is accomplished using a short RF pulse. The frequency response to an RF pulse is approximated by the Fourier transform of the pulse envelope. The envelope of the RF pulse without specific shaping is square, resulting in a frequency profile that has a sinc shape ($\sin(\omega)/\omega$). Knowing this, it is

possible to achieve a frequency profile that is square by using a sinc-shaped RF pulse. Unfortunately, this is only true for an infinitely long RF pulse. For a finite length RF pulse, the edge of the profile becomes less defined and side lobe(s) appear on each side. This effect can be reduced using a Hanning-filtered sinc-shaped RF pulse or more complicated pulse shape calculations such as the Shinnar-LeRoux algorithm (8). A 3 ms Hanning filtered RF pulse consisting of 5 lobes of the sinc-shape is shown in Fig. 1.7. The corresponding frequency response profile is shown in Fig. 1.8. In this case, the effective bandwidth of the RF pulse is 2000 Hz.

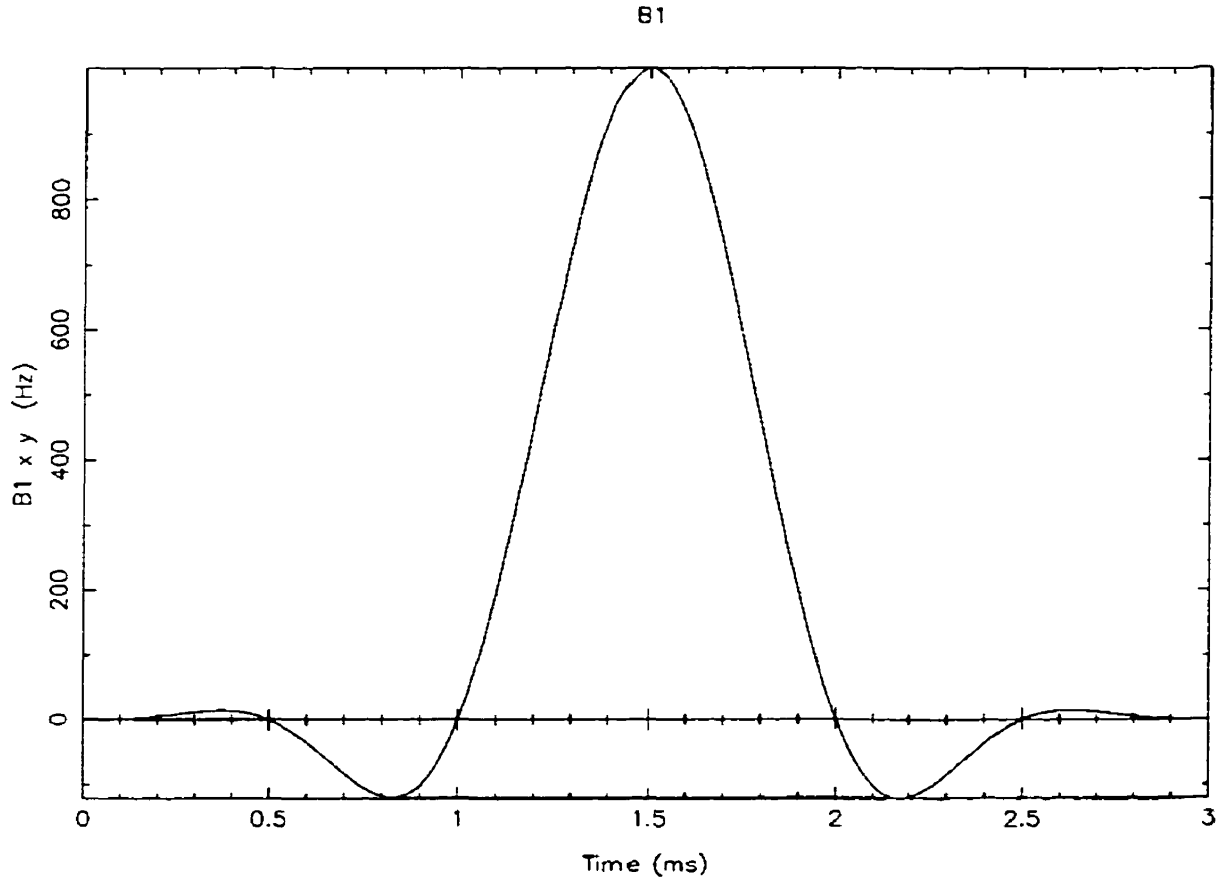

Figure 1.7 Hanning filtered sinc pulse shape, with 5 lobes and 3 ms in length (calculation done using "Bloch", written by Dr. J. C. Sharp, Institute for Biodiagnostics, NRC).

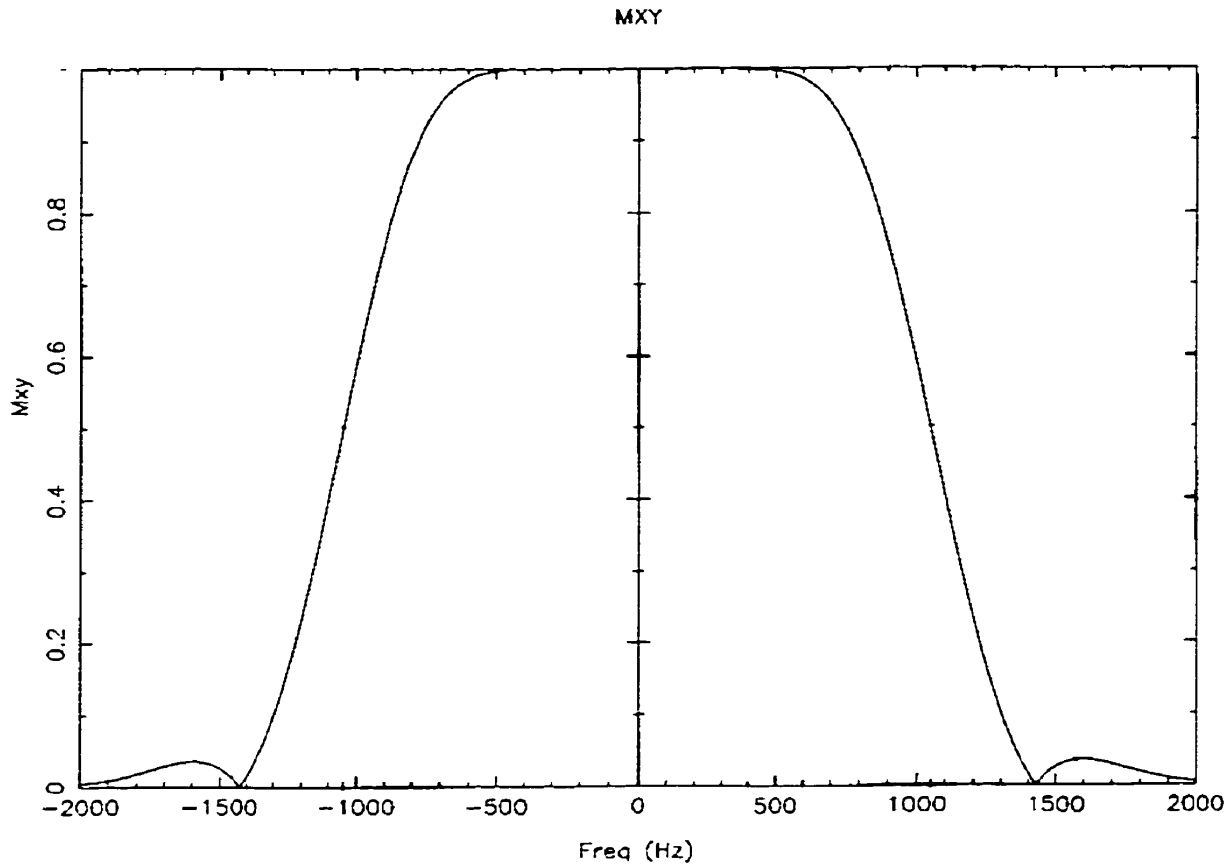

Figure 1.8 Frequency response profile of the Hanning filtered sinc pulse of Fig. 1.7. The effective bandwidth of the RF pulse is 2000 Hz (calculation done using "Bloch", written by Dr. J. C. Sharp, Institute for Biodiagnostics, NRC).

A frequency selective RF pulse of this type is used for selectively suppressing the water resonance in ^{1}H MR spectroscopy.

1.4.2 Spatial Slice Selection

Selection of a plane of signals within a larger sample is accomplished using a frequency selective RF pulse in combination with a linear magnetic field gradient. If the magnetic field inside the magnet varies linearly along the z-direction, the resonance

frequency of isochromat spins will depend on their location within the sample in the z-direction. This follows directly from the Larmor equation,

$$\nu = \frac{\gamma}{2\pi}(B_0 + zG_z), \qquad [1.20]$$

where $G_z = dB_z/dz$ is the magnetic field gradient along the z-direction. Following this by taking the partial derivative of ν with respect to z, the expression for the slice thickness Δz selected by a RF pulse with bandwidth $\Delta\nu$, is given by

$$\Delta z = \left(\frac{2\pi}{\gamma}\right)\frac{\Delta\nu}{G_z}. \qquad [1.21]$$

The relationship between the RF pulse bandwidth, RF pulse frequency offset, gradient strength, slice thickness and slice position is illustrated in Fig. 1.9.

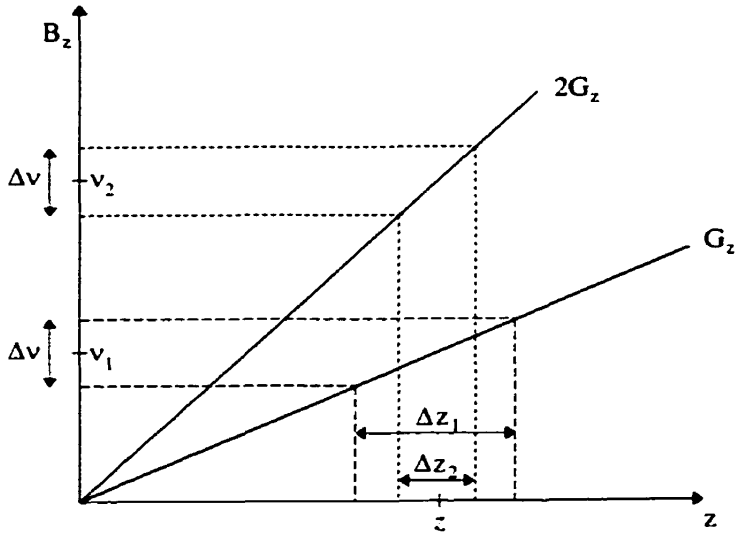

Figure 1.9 Slice selection at a position z using an RF pulse of bandwidth $\Delta\nu$. A slice thickness of Δz_1 is produced for a gradient strength G_z and frequency offset ν_1. To reduce the slice thickness by half, a gradient strength of $2G_z$ and frequency offset ν_2 is required.

Therefore, the slice thickness is controlled by adjusting the gradient strength, and the slice position is determined by the central frequency offset of the frequency selective RF

pulse. Alternatively, the slice thickness can be adjusted by varying the RF bandwidth at constant gradient strength.

1.5 Spatial Localization of MR Spectra

Localization of the NMR signal to a specific region within a sample was first performed with surface coils, in which signal was acquired from the entire sensitive region of the coil (9). The inhomogenous transmit and receive (T/R) surface coil resulted in a very crude method of spatial localization. Surface coil localization was further improved with topical magnetic resonance (10), the use of surface layer suppression (11-15) and single slice selection applied parallel to the surface coil at the depth of interest (16,17). The concept of 3-dimensional volume localization was then developed (18-23). More recently, single shot localization techniques (24) such as PRESS (25) and STEAM (26) or VEST (27) have been used to obtain excellent spatial localization in humans (28.29). These methods use three orthogonal slice selections in combination with spoiler gradient pulses to destroy outer voxel signals, resulting in selection of a homogeneous VOI.

As already described, the gradient strength (G_z) used in a localized spectroscopy experiment is determined from the slice thickness (Δz) and the bandwidth (BW) of the frequency selective RF pulse, that is,

$$G_z(Hz/cm) = \frac{BW(Hz)}{\Delta z(cm)} \quad \Leftrightarrow \quad G_z(mT/m) = \frac{10^5}{\gamma} G_z(Hz/cm) \quad \Leftrightarrow \quad G_z(Gauss/cm) = \frac{10^4}{\gamma} G_z(Hz/cm) \cdot$$

For a typical RF pulse bandwidth of 2000 Hz and a slice thickness of 1 cm, the slice selection gradient strength would be 2000Hz/cm or 4.7 mT/m or 0.47 Gauss/cm.

As the B_0 field is increased, the chemical shift separation of the water and fat resonances increases linearly. That is, in going from 1.5T to 3T, the chemical shift separation goes from $\delta = 211$ Hz to 422 Hz. Consider the respective x-positions of the water and fat slices using the same x-gradient strength, G_z = 4.7 mT/m. The slice shift can be calculated as

$$\Delta z_{Fat-H_2O} = \frac{\delta_{Fat-H_2O}}{(\gamma/2\pi)G_z}. \qquad [1.22]$$

Therefore, at 1.5T, the fat and water slice shift is 1 mm while at 3T it is 2 mm. This must be taken into consideration when placing a voxel within the tissue of interest.

1.5.1 Volume Localization using a Stimulated Echo - STEAM

Volume localization using a stimulated echo, called STEAM or Stimulated Echo Acquisition Mode (26-28), is accomplished by applying three 90° frequency selective RF pulses, each in the presence of an orthogonal gradient. The STEAM sequence is illustrated in Fig. 1.10. The behavior of the magnetization vector was described in Section 1.2.2.5, the only difference here is that each 90° pulse selects a plane of signal. The intersection of the three orthogonal plane is a rectanguloid or voxel. As described in Section 1.2.2.6, a sequence of three RF pulses creates multiple FID's and spin echoes. In this case, each FID comes from one of the planes of signal selected by a 90° pulse. Single spin echoes are created from the intersection of two planes and therefore represents a column of data. To dephase, spoil or crush these unwanted coherences, spoiler or crusher gradients are applied between the slice selections. To refocus the stimulated echo, the gradient area A of the crusher in the first TE/2 period has to be

identical to the crusher in the second TE/2 period. The behavior of the spoiler or crusher gradients and therefore the amount of spoiling of the unwanted coherences is described in detail in CH. 5.

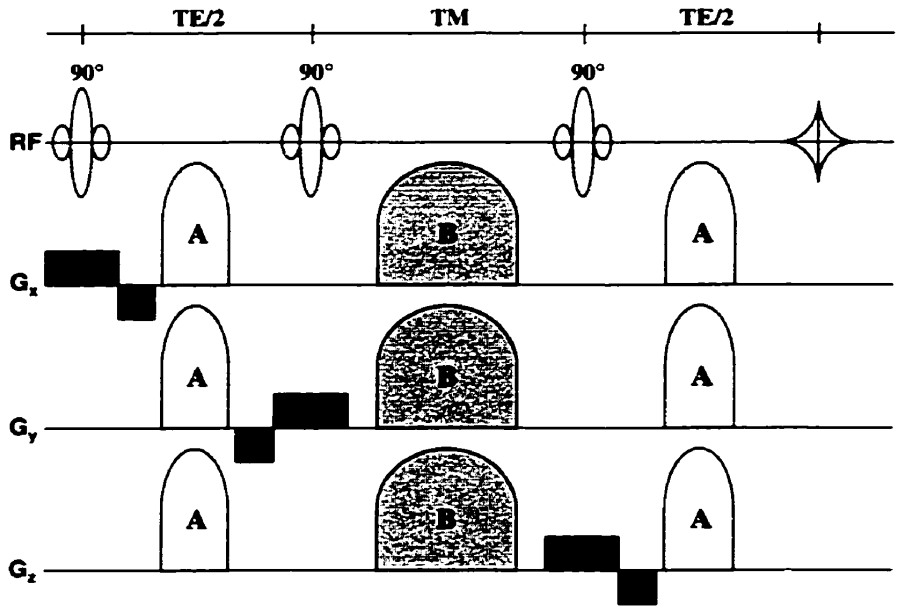

Figure 1.10 The STEAM sequence, consisting of three refocused orthogonal slice selections with immediate refocusing (black), and spoiler or crusher gradients (A and B) to refocus the stimulated echo but spoil or dephase all other coherences.

1.5.2 Volume Localization using a Double Spin Echo - PRESS

Volume localization using a double spin echo, called PRESS or Point RESolved Spectroscopy (25,28), is accomplished by applying a 90° frequency selective RF pulse followed by two 180° frequency selective RF pulses, each in the presence of an orthogonal gradient. The PRESS sequence is illustrated in Fig. 1.11. The behavior of the magnetization vector was described in Section 1.2.2.4, the only difference here is that the 90° and 180° pulses each select a plane of signal. Once again, FID's, single spin echoes

and a stimulated echo are also created. In this case, the FID's created by the last two pulses are small, and require less "spoiling". A comparison of the advantages and disadvantages of PRESS with respect to STEAM is discussed in CH. 5.

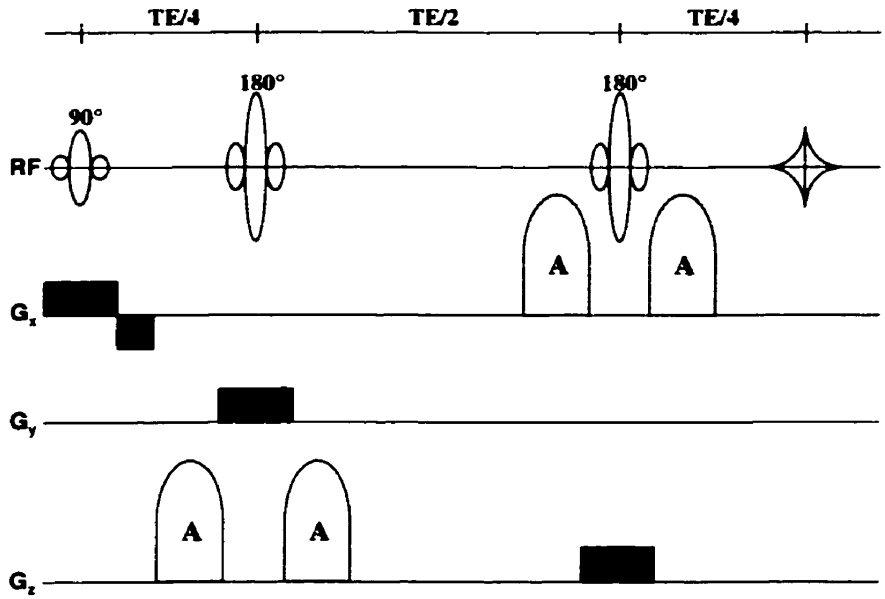

Figure 1.11 The PRESS sequence, consisting of one 90° refocused slice selection, and two 180° self refocussing orthogonal slice selections, with spoiler or crusher gradients to refocus the double spin echo but spoil or dephase all other coherences.

1.6 Magnetic Resonance Imaging (MRI)

The basic imaging sequence requires spatial information in two dimensions over a thin slice selected using the method described in Section 1.4.2. After "slice selection", spatial information over the slice is acquired by "frequency encoding" and "phase encoding". Both of these encoding methods are ways of measuring the phase variation of the magnetization as a function of position. The phase acquired during the application of a linear field gradient G_i of a spin at position r_i is $\phi = 2\pi\nu t$, where $\nu = \frac{\gamma}{2\pi}(B_0 + r_i G_i)$.

Much like the relationship between time and frequency on phase, there is an equivalent description using position and k-space. The change in phase evolution due to the gradient is given by $\phi = \gamma G_i t r_i = k_i r_i$. This describes a Fourier transform pair between k-space and position-space. To use the Fourier transform to interpret spatial encoded k-space data without "aliasing", k_i must be varied in equal increments Δk such that the maximum variation in phase cannot exceed $\pm\pi$, that is $\Delta\phi \leq \pi$. MR images center the field-of-view (FOV) at isocenter, hence the maximum measurable phase increment will be at the edge of the FOV. Therefore, the k-space increment is defined such that

$$\Delta k = \frac{2\pi}{FOV}. \qquad [1.23]$$

1.6.1 Frequency Encoding

One method of *k*-variation is to increment the time, that is, to measure the phase as a function of time. If the spatial encoding direction is chosen to be the x-direction, the phase evolution is given by

$$\Delta\phi = \Delta k_x \, x = \gamma G_x \, \Delta t \, x. \qquad [1.24]$$

This of course is no different than acquiring a complex FID with a sampling rate or spectral width of $1/\Delta t$ and the Fourier transform is a frequency spectrum where x-position is directly proportional to frequency. This method is therefore called "frequency encoding". Usually the spectral width *SW* is fixed, so therefore in order to satisfy the boundary condition when x has its largest value $FOV_x/2$, the "read gradient" can be calculated as

$$G_x = \frac{2\pi}{\gamma}\frac{SW}{FOV_x}. \qquad [1.25]$$

The spectral width is determined from the required resolution in the frequency encoding direction and the acquisition time. That is, if the FOV_x is 25 cm and the required pixel resolution is 1 mm, then N_r = 256 complex data points should be collected. For an acquisition time of 8.0 ms, the data need to be sampled at a rate of 32 kHz. In this case, the read-gradient strength would be 1280 Hz/cm.

1.6.2 Phase Encoding

The only other method of *k*-variation is to increment the gradient, that is, to collect N_p FID's after application of N_p incremented "phase encoding" gradients for a fixed length T_p. In this case phase is measured as a function of phase encoding gradient strength. If this spatial encoding direction is chosen to be the y-direction, the phase evolution is given by

$$\Delta\phi = \Delta k_y\, y = \gamma \Delta G_y T_p\, y. \qquad [1.26]$$

With fixed T_p, the boundary condition of Eq. [1.23] determines the phase encode gradient increment. This has to be satisfied when y has its largest value $FOV_y/2$, such that the phase encode gradient increment is given by

$$\Delta G_y = \frac{2\pi}{\gamma}\frac{1}{T_p\, FOV_y}. \qquad [1.27]$$

The maximum-value that the phase encode gradient requires is then determined from the required resolution. That is, if the FOV_y is 25 cm and the required pixel resolution is 1

mm, then N_p = 256 complex data points should be collected. This implies that the maximum gradient value needs to be

$$G_y^{max} = N_p \Delta G_y . \qquad [1.28]$$

Usually, the phase encode gradient is incremented in a bipolar fashion such that the first value is $-\frac{G_y^{max}}{2}$ and the last value is $+\frac{G_y^{max}}{2} - \Delta G_y$. In this example, with T_p = 5 ms, the phase encode increment would be 8 Hz/cm and the minimum/maximum phase encode gradient strength would be −1024 Hz/cm and 1016 Hz/cm respectively.

1.6.3 Basic Imaging Methods: FLASH and Spin Echo Imaging

Using the spatial encoding methods described above, the N_r x N_p FID data matrix obtained from a slice, selected as described in Section 1.4.2, is given by

$$S(k_x, k_y) = K \iint \rho(x, y) \exp[-i2\pi(k_x x + k_y y)] dx\, dy , \qquad [1.29]$$

where S is the FID signal, K is a constant of proportionality, and $\rho(x,y)$ is the density of spins at position x and y within the selected slice. Therefore, performing an inverse two-dimensional FFT on the FID matrix will yield the spin density matrix resulting in the required 2-D image.

There are some limitations to the spatial encoding techniques described above, that would result in misregistration. The frequency encoding technique requires that frequency be only position dependent. Therefore, this technique would introduce errors due to chemical shift differences of the tissue, magnetic susceptibility variations and gradient shape. Because the phase encoding technique is a phase difference method, it is not sensitive to chemical shift errors or magnetic susceptibility variations, and while

sensitive to gradient area, is insensitive to gradient-shape imperfections. The major disadvantage of phase encoding, is that motion or blood flow causes phase errors, creating what is known as "motion artifacts" or "ghosting".

The two most common methods of imaging are the gradient echo and spin echo methods. In the gradient echo method, a gradient refocused slice selection is performed with a frequency selective RF pulse of flip angle α, followed by a phase encode gradient, a dephasing read gradient (so that an echo occurs in the middle of the acquisition window) and finally an FID is acquired during the read gradient. In the case of FLASH (Fast, Low-Angle SHot) imaging (28), a small flip angle is used (for example $\alpha = 20°$) so that a short repetition time (TR) is achieved. This sequence is illustrated in Fig. 1.12a.

Spin echo imaging can be accomplished with a gradient refocused slice selection and a non-selective 180° RF pulse. This is shown in Fig. 1.12b.

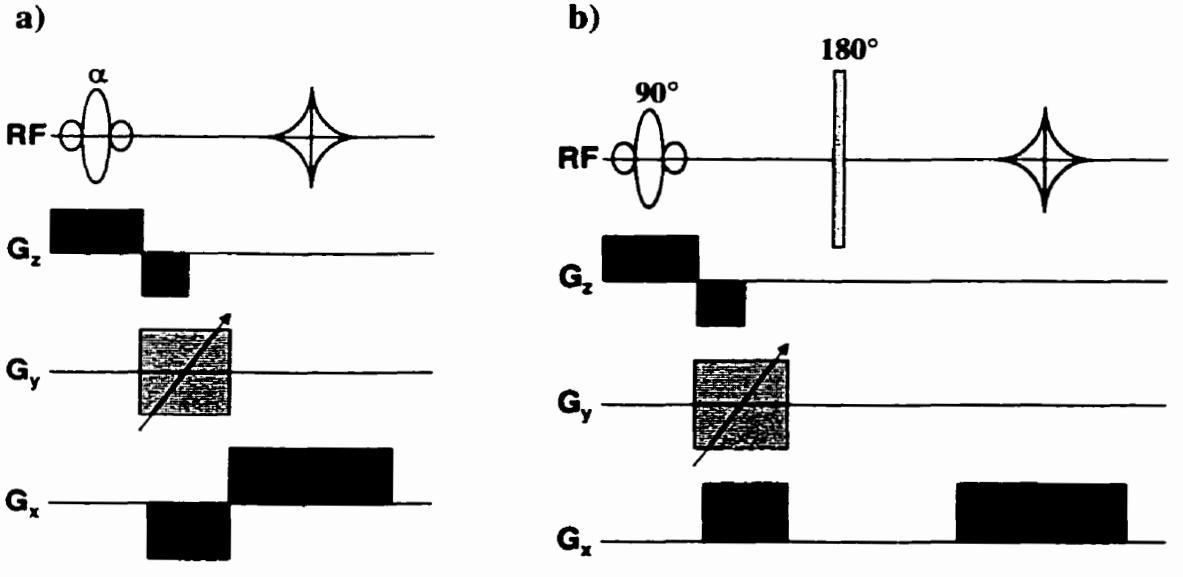

Figure 1.12 The (a) FLASH and (b) spin echo 2-D imaging sequences. In this case the read, phase and slice orientations are in the x, y and z directions respectively.

1.7 The Apparatus

1.7.1 The Magnet, Shim Coils and Gradient Coils

Superconducting imaging systems consist of the magnet, the cryostat, the field gradient and shim coils with corresponding electronics, the RF coil and transmitter/receiver system, and the console/computer with software to control the operation of all components. Figure 1.13 illustrates the hardware components of the imaging system.

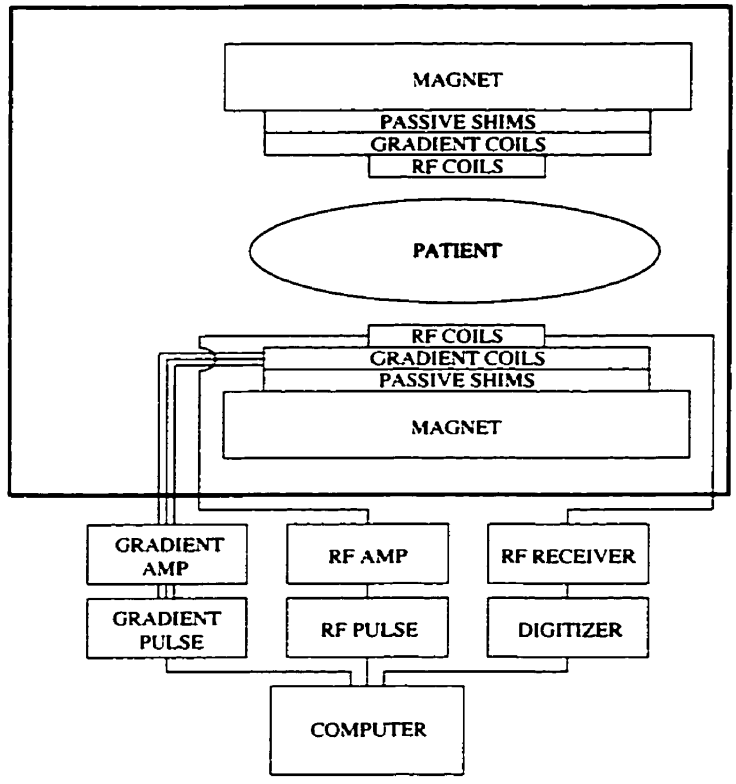

Figure 1.13 The components of an MRI system.

As was explained earlier, the amount of polarization and hence the amount of signal-to-noise available for spectroscopy and/or imaging experiments is directly proportional to

the magnet strength. In spectroscopy, SNR is of ultimate importance, and therefore the largest field strength available is used. Therefore, all magnets used for both *ex vivo* and *in vivo* MR spectroscopy are superconducting, achieving field strengths up to 17.5 Tesla for *ex vivo* spectroscopy studies and up to 8 Tesla for *in vivo* spectroscopy studies. Superconducting magnets are made from alloys such as niobium-titanium or niobium-tin, superconducting at 4.2 K, and therefore require liquid helium for operation.

The inhomogeneity of the magnetic field when it is first installed can be 100 ppm over the volume of a head, but this can be improved using passive shimming of the magnetic field and shim coils characterized by specific spherical harmonics that cancel the remaining constant field inhomogeneities (see Chapter 5).

Linear magnetic field gradients are required for spatial encoding and slice selection in imaging, and voxel selection and coherence elimination for *in vivo* spectroscopy. Typical gradient strengths in imaging systems are 20 mT/m, capable of a slice thickness of 2 mm. The rate at which the gradient can be ramped is called the slew rate, which results in a particular rise time. Rise times for general imaging and spectroscopy are 800 μs to 1 msec, while for fast imaging techniques such as echo planar imaging (EPI) rise times of 150-300 ms are required. Gradient design focuses on achieving a desired distribution of current density and direction by winding wire into a particular pattern, while minimizing the total inductance and maximizing the energy stored in the gradient field. This method maximizes the current that can flow in the coils and hence the gradient slew rate, resulting in decreased rise times.

If a gradient waveform modulator puts a rectangular pulse into the gradient amplifier, the actual gradient produced would have rounded rise and fall characteristics

(Fig. 1.14). To compensate for this, "premphasis" is performed on the gradients, whereby the gradient value is overshot on the rising edge and undershot on the falling edge. Both the amplitude of these overshoots and the their time constants of decay can be adjusted.

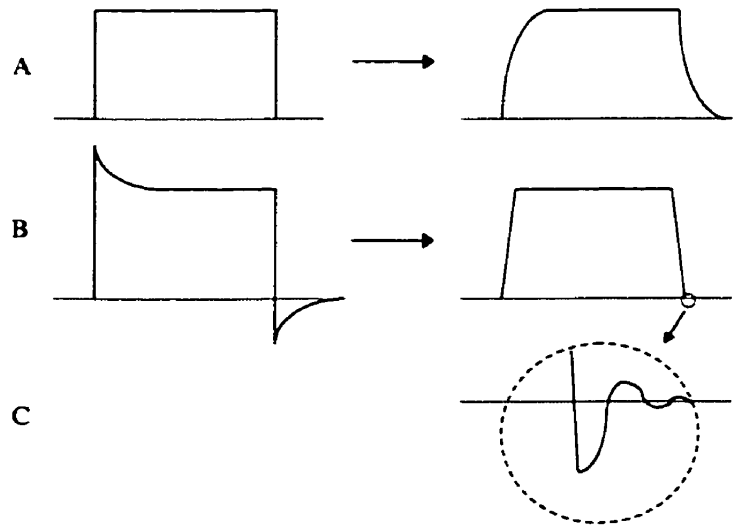

Figure 1.14 Author illustration of the output waveform of the gradient pulse modulator (left) and actual gradient pulse shape produced (right) (a) without and (b) with premphasis, and (c) imperfections of the gradient amplifier producing a small ringing effect.

Switching the linear magnetic field gradients also causes flux changes in the surrounding metal of the cryostat and magnet, which induce 'eddy' currents that can persist for many milliseconds. These 'eddy' currents produce time dependent changes in every harmonic of the field, each with its own time constant. Changes in the main magnetic field are corrected for using a B_0 compensation coil, while changes in higher order harmonics are compensated by fine tuning the preemphasis, which will depend on the sequence used.

Additional eddy current correction can be applied post-data acquisition, which will be further explained in Chapter 5.

1.7.2 RF Coils

As described previously, NMR excitation and detection is done with a coil or probe capable of delivering and detecting RF magnetic field perpendicular to the B_0 field. This transverse B_1 field can be produced by many types of coils, but is dependent on the geometry of the magnet and the direction of the B_0 field. For MRI systems, there are coils that produce a uniform B_1 field within the volume of the coil but have lower sensitivity and coils that have high sensitivity but produce inhomogeneous B_1 field. These are termed volume coils and surface coils, respectively. The most commonly used volume coil for superconducting tunnel magnets is the birdcage coil (31), while for C-shaped vertically polarized magnets the solenoid coil is most common. Surface coils (9) are used for higher SNR applications such as spectroscopy, and will be discussed in detail in Ch. 3.

If unit alternating current is put into an RF coil, an RF magnetic field of magnitude $\hat{B}_1$ will be produced at a point r within the volume of a volume coil or near the surface of a surface coil. The principle of reciprocity (32) states that if a small rotating magnet is placed at the same point r, then a voltage will be induced in the coil, proportional to $\hat{B}_1$. This enables one to calculate the signal received from a coil, and therefore can be used in SNR calculations (see Chapter 3). The voltage induced in a coil is given by

$$S = \omega_0 \hat{B}_1 M_0 \Delta V , \qquad [1.30]$$

where ΔV is the volume element from which signal is taken. From the principle of reciprocity, one can see how the same transverse RF B_1 coil is used for both excitation and detection.

In order to maximize power transfer from the transmitter coil to the sample during excitation, as well as maximize detection SNR, an RF coil that is a tuned high-Q LC resonator is employed. The resonance frequency of a LC resonator is given by

$$\nu_0 = \frac{1}{2\pi\sqrt{LC}}, \qquad [1.31]$$

where L and C are the total inductance and capacitance of the resonator.

1.7.2.1 Impedance Matching to the Transmitter/Receiver

The coil has to be tuned to the resonance frequency of the particular nucleus being studied which will be dependent on coil loading. Coil loading refers to the amount of magnetic and electric field interactions with the sample, or inductive and dielectric losses, respectively. Dielectric losses in the sample tend to increase the effective capacitance of the coil and thereby decrease the resonance frequency of the coil. Inductive losses tend to decrease the effective inductance of the coil and hence increase the frequency of the coil.

In order to excite the NMR signal with optimum efficiency, the RF coil has to be impedance matched to the transmitter electronics and the cable connected to the coil. In general, the coil is connected to a cable with a characteristic impedance of 50 Ω. There are two methods of matching: capacitive and inductive.

The inductive matching method will be discussed in detail as this is the method used for the RF coils developed in this thesis. Consider the situation where a coil such as a

surface coil (or loop of wire), called the secondary coil, tuned to the Larmor frequency of the NMR signal, is brought near another tuned loop, called the primary coil. When they are brought close to each other, there will be a certain degree of interaction between the coils, known as coupling, that is described by the coupling constant $k = \frac{M}{\sqrt{L_s L_p}}$.

This coupling is due to the mutual inductance, M, between primary and secondary coils with self inductances L_p and L_s respectively. The coupling can also be described as a shared impedance between coils. A detailed analysis reveals that the secondary coil couples an impedance, $\frac{(\omega M)^2}{Z_s}$, into the primary such that the effective primary impedance is given by (33)

$$Z'_p = Z_p + \frac{(\omega M)^2}{Z_s}, \qquad [1.32]$$

and the current induced in the secondary coil is given by

$$I_s = -j\frac{\omega M I_p}{Z_s}, \qquad [1.33]$$

where I_p ($I_p = \frac{V_p}{Z_p + \frac{(\omega M)^2}{Z_s}}$) is the current input into the primary coil, required to produce the appropriate response in the secondary coil.

As both the primary and the secondary coils are at resonance, $Z_s = R_s$ and $Z_p = R_p$. For a high-Q secondary coil ($Q_s = \frac{\omega L_s}{R_s}$), the secondary impedance is small and subsequently $Z'_p >> Z_p$ and $I_s >> I_p$. Further, consider the secondary coil matched to the

impedance of the primary coil and the attached 50 Ω cable. During a matched condition, the effective impedance of the primary is equal to the effective impedance of the secondary, known as critical coupling ($k = \frac{M}{\sqrt{Q_s Q_p}}$). In this case, $\frac{(\omega M)^2}{Z_s} = R_p$ and

$$I_s = -j\frac{\omega M I_p}{R_s} = -j\sqrt{\frac{R_p}{R_s}} I_p. \qquad [1.34]$$

For example, if R_s = 0.2 Ω and R_p = 50 Ω + 0.2 Ω, then the induced secondary current, I_s ~ -j 15 I_p. This implies that the current in the primary coil is not only much smaller than the current in the resonator, but it is 90° out of phase. By combining the two orthogonal B_1 fields ($B_{1eff} = \sqrt{B_{1s}^2 + B_{1p}^2}$) it can be seen that the magnitude of the effective B_1 field has changed by only 0.2%. Now consider a high-Q coil (Q_U = 250) loaded by a large conductive sample, such that the loaded-Q (Q_L) drops to 50. The effective resistance of the secondary coil now rises from 0.2 Ω to 1.0 Ω ($= \left(\frac{Q_U}{Q_L}\right) 0.2\,\Omega$). Even in this case, the secondary current is still 7.9 times larger than the primary current resulting in only a 0.8% effect on the effective B_1. If higher resistance conductor is used, with a resistance of 0.7 Ω, there would be a 3.4% change in the effective B_1 field. Therefore, for inductively coupled coils, it may be more necessary to keep the secondary conductor resistance (R_S) lower by using larger diameter copper tubing rather than copper foil. Of course, this effect is further reduced when the matching loop is placed further from the sample, which is generally the case, and hence a lower B_{1p} within the sample. There is also a phase change associated with the small field produced by the matching loop, but in

a transmit/receive coil arrangement this phase change is mirrored between transmission and reception and no signal loss results.

1.7.2.2 Reduced Dielectric Coupling to the Sample using Distributed Capacitance

An RF coil is simply a series resonant inductor-capacitor circuit. In most cases the inductance is fixed (depending on the size and orientation of the conductor segments). Capacitors are used to tune the coil to the desired resonance frequency. In additional to the inductive losses described above, there are dielectric losses from the conservative electric field associated with the capacitors that extends into the sample. There is a voltage drop across each capacitor on the coil from which this electric field originates, that is smaller for larger capacitance values. For a given resonator, the total capacitance is dependent on the frequency, and is therefore fixed. By distributing the capacitance along the conductor, this capacitance at individual sites can be increased to a value proportional to the number of capacitors used. For example, if a single loop surface coil requires a capacitance of 20 pF, and the coil is segmented into four sections, than each gap would now require 80 pF capacitors. To further reduce dielectric coupling to the sample, copper foil shields are placed between the coil and the sample underneath the capacitors.

1.7.3 The Transmitter, the Receiver and the Console

The transmitter is responsible for the RF pulse shape, duration, power, and timing, which is then coupled to the sample using the RF coil. The RF pulse is produced by mixing (multiplying) a user-defined oscillation, created from a frequency synthesizer, with a user-defined pulse shape created from a waveform generator. Modern transmitters

now typically use digital pulse shape generators. Finally, the RF pulse is amplified with a RF amplifier (32).

One method of reducing the slice shift artifact discussed previously is to increase the RF bandwidth, thereby also increasing the gradient strength required. The reduced chemical shift artifact comes at the expense of SNR as more noise is collected from a larger bandwidth. A large bandwidth RF pulse is also shorter and therefore requires more RF power to produce the same flip angle. Limits on the digital amplitude resolution of the digital transmitter can cause the side lobes of frequency selective sinc pulses to become jagged. Additional limitations on the time resolution of the transmitter can also cause the RF pulse to be coarse in time.

The RF signal received from the RF coil is first amplified with a low-noise amplifier or preamplifier, which prevents the weak received signal from being dominated by noise as it travels down a transmission line (the second stage of the receiver system) to the remote location of the remaining receiver circuitry. The remote receiver circuitry consists of additional amplifiers, a demodulator, and an ADC to digitize the analog signal for analysis. Demodulation of the RF band signal (usually with respect to a reference frequency set to the transmitter frequency) into a low frequency band is required for digitization by the ADC.

The MRI console contains the operating software responsible for the timing and amplitudes of all gradient and RF pulses used during excitation of magnetzation as well as switching the receiver on and off. It also controls offset frequencies of the RF pulses, shim coil currents, as well as B_0-compensation and premphasis currents. The console also contains the Fourier transform software required for spectral interpretation of 1-D

spectroscopy data and 2-D image creation from the frequency and phase encoded data. In addition, the console performs some limited forms of image and spectroscopic analysis.

1.8 References

1. C. P. Slichter, Principles of magnetic resonance. Springer-Verlag, Berlin, Germany, 2nd ed. (1978).
2. F. Bloch, W. W. Hansen, M. Packard, Nuclear induction. *Phys. Rev.* **69**, 127 (1946).
3. T. C. Farrar, E. D. Becker, Pulse and Fourier transform NMR. Academic Press, Inc., Toronto (1971).
4. T. J. Lawry, G. S. Karczmar, M. W. Weiner, G. B. Matson, Computer simulation of MRS localization techniques: an analysis of ISIS. *Magn. Reson. Med.* **9**, 299-314 (1989).
5. E. L. Hahn, Spin Echoes. *Phys. Rev.* **80**, 580-594 (1950).
6. R. C. Gonzalez, R. E. Woods, Digital image processing. Addisson-Wesley Publishing Company, Reading, Massachusetts (1992).
7. R. K. Harris, Nuclear magnetic resonance spectroscopy, a physiochemical view. Pitman, UK, (1983).
8. J. Pauly, P. LeRoux, D. Nishimura, A. Macovski, Parameter relations for the Shinnar-Le Roux selective excitation pulse design algorithm. *IEEE Trans. Med. Imaging* **10**, 53 (1991).
9. J. J. H. Ackerman, T. H. Grove, G. G. Wong, D. G. Gadian, G. K. Radda, Mapping of metabolites in whole animals by ^{31}P NMR using surface coils. *Nature* **283**, 167-170 (1980).
10. R. E. Gordon, P. E. Hanley, D. Shaw, D. G. Gadian, G. K. Radda, P. Styles, P. J. Bore, L. Chan, Localization of metabolites in animals using ^{31}P topical magnetic resonance. *Nature* **287**, 736-738 (1980).
11. T. A. Cross, C. Pahl, R. Oberhansli, W. P. Aue, U. Keller, J. Seelig, Ketogenesis in the living rat followed by ^{13}C NMR spectroscopy. *Biochemistry* **23**, 6398-6402 (1984).

12. J. L. Evelhoch, M. G. Crowley, J. J. H. Ackerman, Signal-to-noise optimization and observed volume localization with circular surface coils. *J. Magn. Reson.* **56**, 110-124 (1984).

13. A. Haase, W. Hänicke, J. Frahm, The influence of experimental parameters in surface-coil NMR. *J. Magn. Reson.* **56**, 401-412 (1984).

14. M. R. Bendall, R. E. Gordon, Depth and refocusing pulses designed for multipulse NMR with surface coils. *J. Magn. Reson.* **53**, 365-385 (1983).

15. R. Sauter, S. Müller, H. Weber, Localization in *in vivo* ^{31}P NMR spectroscopy by combining surface coils and slice-celective saturation. *J. Magn. Reson.* **75**, 167-173 (1987).

16. P. A. Bottomley, T. B. Foster, R. D. Darrow, Depth-resolved surface coil spectroscopy (DRESS) for *in vivo* ^{1}H, ^{31}P, and ^{13}C NMR. *J. Magn. Reson.* **59**, 338-342 (1984).

17. S. Müller, W. P. Aue, J. Seelig, NMR imaging and volume-selective spectroscopy with a single surface coil. *J. Magn. Reson.* **63**, 530-543 (1985).

18. H. Post, D. Ratzel, P. Brunner, West German Patent, No. P3209263.6, 13 March 1982.

19. W. P. Aue, S. Müller, T. A. Cross, J. Seelig, Volume-selective excitation. A novel approach to topical NMR. *J. Magn. Reson.* **56**, 350-354 (1984).

20. R. J. Ordidge, A. Connelly, J. A. Lohman, Image-selected *in vivo* spectroscopy (ISIS). A new technique fpr spatially selective NMR spectroscopy. *J. Magn. Reson.* **66**, 283-294 (1986).

21. P. R. Luyten, A. J. H. Marien, B. Sijtsma, J. A. Den Hollander, Solvent-suppressed spatially resolved spectroscopy. An approach to high-resolution NMR on a whole-body MR system. *J. Magn. Reson.* **67**, 148-155 (1986).

22. D. M. Doddrell, W. M. Brooks, J. M. Bulsing, J. Field, M. G. Irving, H. Baddeley, Spatial and chemical-shift-encoded excitation. SPACE, a new technique for volume-selective NMR spectroscopy. *J. Magn. Reson.* **68**, 367-372 (1986).

23. A. Haase, Localization of unaffected spins in NMR imaging and spectroscopy (LOCUS spectroscopy). *Magn. Reson. Med.* **3**, 963-969 (1986).

24. R. Kimmich, D. Hoepfel, Volume-selective multipulse spin-echo spectroscopy. *J. Magn. Reson.* **72**, 379-384 (1987).

25. P. A. Bottomley, Selective volume method for performing localized NMR spectroscopy. U.S. Patent 4 480 228 (1984).

26. J. Frahm, K.-D. Merboldt, W. Hänicke, Localized proton spectroscopy using stimulated echoes. *J. Magn. Reson.* **72**, 502-508 (1987).

27. J. Granot, Selected Volume excitation using stimulated echoes (VEST). Applications to spatially localized spectroscopy and imaging. *J. Magn. Reson.* **70**, 488-492 (1986).

28. C. T. W. Moonen, M. von Kienlin, P. C. M. van Zijl, J. Cohen, J. Gillen, P. Daly, G. Wolf, Comparisons of single-shot localization methods (STEAM and PRESS) for *in vivo* proton NMR spectroscopy. *NMR Biomed.* **2**, 201-208 (1989).

29. P. C. M. van Zijl, C. T. W. Moonen, J. R. Alger, J. S. Cohen, S. A. Chesnick, High field localized proton spectroscopy in small volumes: greatly improved localization and shimming using shielded strong gradients. *Magn. Reson. Med.* **10**, 256-265 (1989).

30. A. Haase, J. Frahm, D. Matthaei, w. Hanicke, K.-D. Merboldt, FLASH imaging. Rapid NMR imaging using low flip-angle pulses. *J. Magn. Reson.* **67**, 258-266 (1986).

31. C. E. Hayes, W. A. Edelstein, J. J. Schenck, O. M. Mueller, M. Eash, An efficient, highly homogeneous radiofrequency coil for whole-body NMR imaging at 1.5T. *J. Magn. Reson.* **63**, 622-628 (1985).

32. D. I. Hoult, R. E. Richards, The signal-to-noise ratio of the nuclear magnetic resonance experiment, *J. Magn. Reson.* **24**, 71-85 (1976).

33. F. E. Terman, Electronic and radio engineering. McGraw-Hill Book Company, Inc. 5th ed. New York (1955).

34. J. Jin, Electromagnetic analysis and design in magnetic resonance imaging. CRC Press, Boca Raton, Florida (1999).

Chapter 2

BACKGROUND, OBJECTIVES AND HYPOTHESIS

2.1 The Thyroid Gland

2.1.1 Anatomy

The thyroid gland, called *thyreos-ma*, or "shield" by the Greeks because of its shape was thought to shield the larynx. This butterfly shaped gland wraps anteriorly around the trachea at the seventh cervical vertebrae just inferior to the larynx. It consists of two lobes joined together at the center of the trachea by the isthmus which sits just below the cricoid cartilage. The thyroid is covered anteriorly by the sternothyroid muscles and more superficially by the sternohyoid and sternocleidomastoid muscles. The adult thyroid weighs about 20 g and each lobe is approximately 2x2x4 cm (1), elongated in the cephalocaudal dimension, with the distance from the center of the gland to the surface of the neck ranging from 1.3 to 2.3 cm. The thyroid gland anatomy is shown for the axial or transverse plane in Fig 2.1.

2.1.2 Histology and Physiology

The fundamental component of the thyroid gland is the thyroid follicle (Fig. 2.2), a single layer of epithelial (follicle) cells covering the surface of a spherical lumen, filled with a viscous fluid called colloid (1). The basal membrane surrounds the outside surface of the follicle while the apical membrane separates the inner colloid from the follicle cells. Microvilli protrude from the apical surface of the follicle cells into the central lumen. Thyroid follicles have an average diameter of 200-300 μm and are grouped in indistinct

lobules. The follicle cells can be either squamous, cuboidal, or columnar. When the follicle is hyperactive, these epithelial cells become columnar, and when it is hypoactive, they are squamous or cuboidal. Follicular activity is accompanied by a decrease in the quantity of colloid and overall size.

The physiological function of the follicle is to produce two thyroid hormones, thyroxine (T_4) and triiodothyronine (T_3), which are secreted directly into the bloodstream. These hormones are essential for energy metabolism, normal growth and development as well as regulation of many metabolic processes. A feedback system between the hypothalmus, pituitary and thyroid gland regulates thyroid hormone production and secretion. When the normal concentration of thyroid hormones in the blood falls, the pituitary gland secretes more thyroid-stimulating hormone (TSH). A rise in thyroid hormone concentration in the blood causes inhibition of the release of TSH.

The thyroid gland also contains parafollicular cells (C-cells) found either as isolated clusters between thyroid follicles or as part of the epithelium, but the apical surfaces of these cells are never in contact with the colloid. Parafollicular cells are larger than follicular cells and are easily recognized with histological staining techniques. Their physiological purpose is to produce and secrete another hormone, calcitonin. This hormone works together with parathyroid hormone (PTH) to regulate the calcium level of the blood. Calcitonin acts to inhibit the removal of calcium from the bones when calcium levels become much higher than normal, whereas PTH stimulates calcium release from bone when blood-calcium levels are low.

Because the three hormone products of the thyroid are secreted directly into the bloodstream, the gland has extensive vascularity.

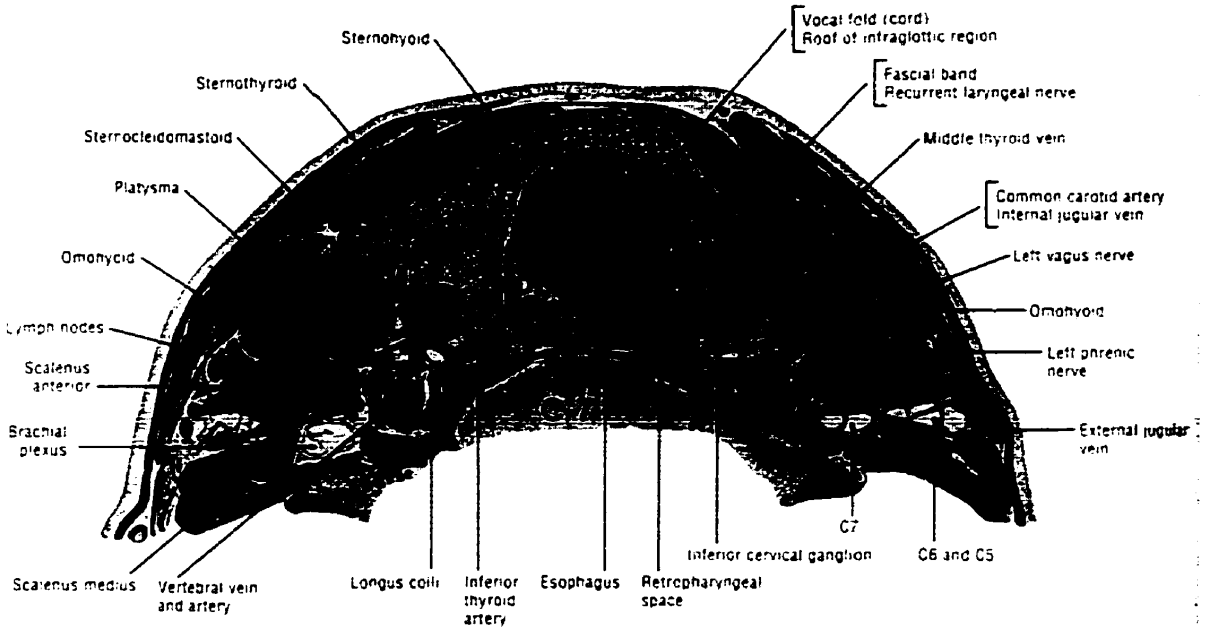

Figure 2.1 The thyroid gland anatomy [adapted from Grant's Atlas of Anatomy, pg. 576 (2)].

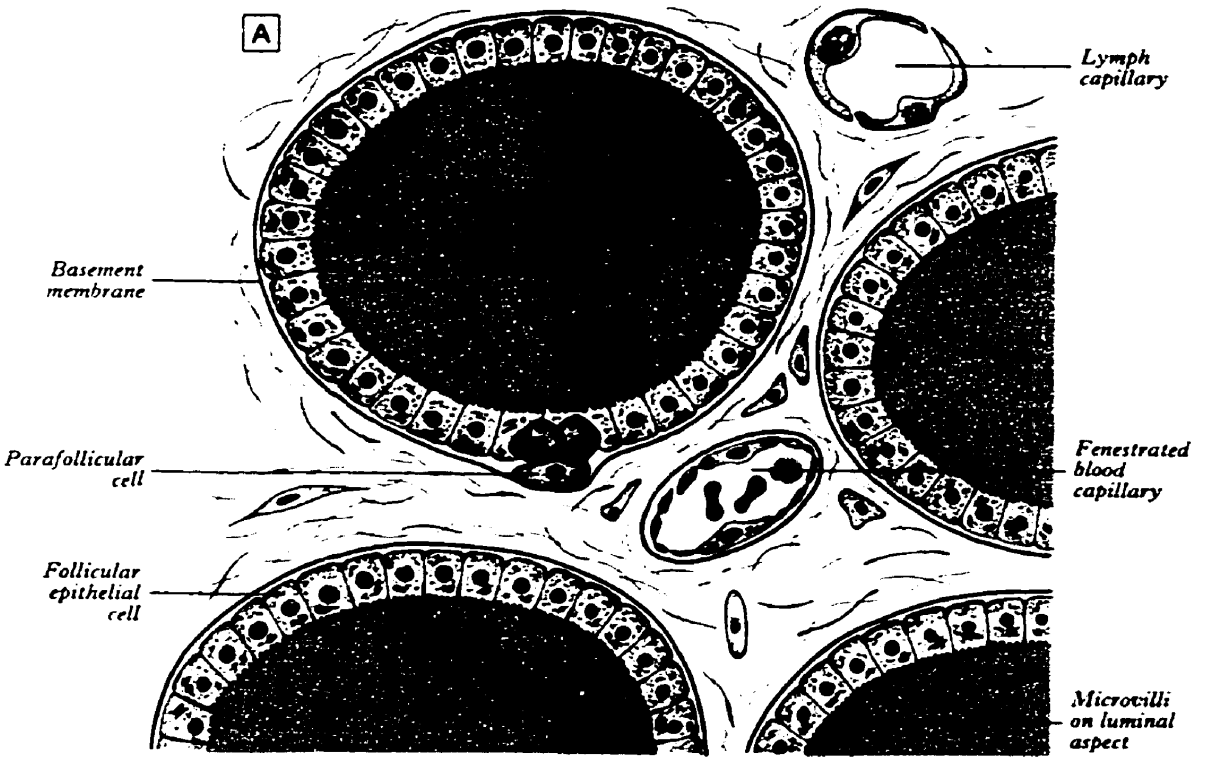

Figure 2.2 Follicular cells of the thyroid gland [adapted from Gray's Anatomy, Endocrine System, pg. 1893 (3)].

2.1.3 Histophysiology and Biochemistry

Iodide ions present in the capillary bed on the basal surface of the follicle cells are trapped and transported through the cell to the apical membrane (1). Within the follicle cells, the tyrosine-rich protein, thyroglobulin, is synthesized and stored in the colloid. Tyrosine residues in the thyroglobulin molecule are iodinated in the colloid when it is in contact with the apical membrane. Iodination creates two precursors to the thyroid hormones; monoiodotyrosine (MIT or T_1) and di-iodotyrosine (DIT or T_2) from the addition of one and two iodide molecules, respectively. The hormone thyroxine (tetraiodothyronine or T_4) is formed from the coupling of two adjacent T_2 molecules, and the hormone triiodothyronine (T_3) is formed from the coupling of a T_1 and a T_2 molecule. Final breakdown of the thyroglobulin molecule occurs within the follicle cells where thyroxine and triiodothyronine are cleaved and then secreted into the bloodstream.

2.2 Non-neoplastic Abnormalities of the Thyroid

2.2.1 Hyperthyroidism

Thyrotoxicosis or hyperthyroidism is a common condition resulting from excess thyroid hormone (increased T_3 and/or T_4). The main disorders associated with this are Grave's disease and toxic nodular goiter. Grave's disease is the most common cause of hyperthyroidism in young individuals whereas toxic nodular goiter is more prevalent in the elderly. Diffuse symmetrical enlargement of the thyroid gland is characteristic of Grave's disease while asymmetric enlargement occurs in toxic nodular goiter. Transient hyperthyroidism is frequently associated with thyroiditis as well as exposure to iodide for contrast studies and iodine containing drugs.

Symptoms include: nervousness, palpitations (sensation of rapid heart beat), fatigability, muscular weakness, weight loss with good appetite, diarrhea, heat intolerance, warm skin, excessive perspiration, menstrual changes and tremour. Objective signs include; eye changes (forward protrusion of the eyes), rapid pulse, enlargement of the thyroid gland and warm smooth skin. Hyperthyroidism can be treated with antithyroid drugs, radioactive iodine (^{131}I) or surgery.

2.2.2 Hypothyroidism

Hypothyroidism is a common condition resulting from insufficient thyroid hormone (decreased T_3 and T_4 production). The major causes of hypothyroidism are autoimmune disorders such as Hashimoto's thyroiditis and hypothyroidism as a result of therapy for hyperthyroidism (^{131}I or surgery). Symptoms include: slowing of physical and mental activity (speech and intellectual), fatigue, weight gain (accompanied by anorexia), cold intolerance, lethargy (drowsiness), apathy (lack of feeling or emotion), constipation. Objective signs include lower heart rate, thickened-coarse-dry skin and enlarged tongue. Hypothyroidism during infancy can cause cretinism. Hypothyroidism can be treated with hormone replacement therapy.

2.2.3 Goiter

A goiter or enlargement of the thyroid gland is usually euthyroid but can be associated with hyper- or hypothyroidism. The major causes of goiter are Hashimoto's thyroiditis, Grave's disease and iodine deficiency. With iodine defiency, the thyroid is enlarged by increased TSH levels in an attempt to maintain thyroid hormone production. Non-toxic

goiters can be treated with T_4 suppression of TSH if started before autonomously functioning nodules develop.

2.3 Adenoma and Carcinoma of the Thyroid

Most tumors of the thyroid gland arise from glandular tissue and are therefore adenomas or carcinomas (4). Clinically palpable thyroid nodules are found in 4 to 7% of adults (5,6), half of which are single on physical examination (7). Thyroid cancer, which represents less than 5% of these, requires surgical treatment (6,8). Single nodules, which are about four times more common in women than in men (7), fall into three major categories; cysts, adenomas and carcinomas. A solitary nodule is more suspect of being malignant than multiple nodules (9), although there is evidence that a dominant nodule in a multinodular gland also has a significant risk of being malignant (10).

2.3.1 Adenomas

Almost all adenomas are solitary nodules, and less than 4 cm in diameter (9). Thyroid adenomas are, for the most part, follicular adenomas. Subtypes are the macrofollicular adenoma or simple colloid adenoma which have no malignant potential (7). Other subtypes such as microfollicular adenoma, trabecular adenoma, Hurthle cell adenoma and papillary cystadenoma do have some malignant potential. The morphology of the adenoma is complete fibrous encapsulation, a clear distinction between the architecture inside and outside the capsule, compression of the thyroid parenchyma around the adenoma and a lack of multinodularity in the remaining gland (9).

2.3.2 Carcinomas

In 1998, there were about 17,200 new thyroid cancer cases diagnosed in the US with about 1,200 deaths from the disease (11). The main types of thyroid carcinoma and their sub-types (7,12) are shown in the table below.

Table 2.1 Classification of malignant tumors of the thyroid gland

WELL-DIFFERENTIATED CARCINOMA
Papillary or papillary-follicular adenocarcinoma (70%)
Follicular carcinoma (15%)
UNDIFFERENTIATED (ANAPLASTIC) CARCINOMA (5%)
Small cell carcinoma
Giant cell carcinoma
MEDULLARY CARCINOMA (5%-10%)
OTHERS - Lymphoma (5%)

Papillary Adenocarcinoma is the most common cause of malignant thyroid nodules. Microscopically, papillary carcinoma consists of well-differentiated thyroid epithelium covering papillary fibrovascular stalks (4). These papillae project from the thyroid capsule (nipple-like), while the nuclei have a distinctive ground glass appearance. Many of these carcinomas are neither purely papillary nor purely follicular, but mixtures of varying proportions and hence the term papillary-follicular adenocarcinoma.

Follicular carcinoma is distinguished from papillary carcinoma by the absence of ground-glass nuclei and well-formed papillae (9). The tumors vary from well-differentiated and normal appearing thyroid tissue to nearly solid sheets of epithelial cells with little or no follicle formation (4). Follicular carcinoma is distinguished from follicular adenoma only by demonstration of capsular and vascular invasion. Therefore, fine-needle aspiration biopsy (FNAB), the main diagnostic tool for thyroid nodules, cannot differentiate between benign and malignant follicular tumors. A malignant diagnosis cannot be made without removal of

the entire nodule, and even at frozen section, the carcinomatous nature is difficult to recognize (4). These nodules usually give an indeterminate result on FNAB.

Medullary carcinoma is a malignant tumor of the parafollicular or C-cells of the thyroid gland. The dominant site of this neoplasia is at the junction of the superior and middle third of the gland where the C-cells predominantly aggregate. As C-cells are responsible for calcitonin production, calcium deposition is common.

Undifferentiated (Anaplastic) carcinoma is the most agressive form of thyroid carcinoma, and is associated with rapid growth, extensive local invasion and rapid metastasis. The tumor tissue lacks structural differentiation, although remnants of differentiated carcinomas (papillary, follicular, medullary) may be found (13).

2.4 The Problem: Diagnosis of Thyroid Nodules

It has been estimated that solitary thyroid nodules are present in 10% of the population. Of these, the majority (90-95%) are benign, being either simple colloid nodules or benign follicular adenomas (14). FNAB is a simple, cost effective technique for diagnosing thyroid cancer, with an acceptably low false-negative rate (15). Other diagnostic procedures that aid in management of thyroid nodules are; radionuclide scanning, ultrasonography, thyroid function tests, as well as the patient's age and tumor size (6). FNAB has greatly reduced the number of patients undergoing thyroidectomy to exclude malignancy. A limitation of FNAB is that cancer may be missed if either the operator does not place the needle in the lesion or the cytologist misinterprets the cellular findings. Although fine needle aspiration biopsy (FNAB) cytology is accurate in identifying papillary, medullary and anaplastic carcinomas, it is unable to differentiate benign from malignant follicular neoplasms because the cellular

components of both types of tumor have the same cytomorphology (16). The criterion for malignancy has been characterized by capsular and/or vascular invasion at the periphery of the neoplasm. This requires surgical removal of the entire tumor as well as substantial portions of the surrounding normal thyroid tissue. About 20% to 30% of nodules assessed by FNA fall into the suspicious follicular category with only 10% to 20% of these actually proving to be malignant (15). Therefore, large numbers of patients each year undergo unnecessary thyroidectomy solely for diagnostic purposes (17). If surgery could be avoided, so too would trauma to the patient, not to mention the substantial savings in health care.

Even when complete thyroidectomy is performed, it is not always possible to distinguish absolutely between benign and malignant follicular neoplasms. This depends on the particular pathologist, since different pathologists may give different diagnoses (16). As with other tumors elsewhere in the body, the identification of histological criteria of malignancy is often a matter of extensive sampling and therefore subject to error. Variations in reported survival figures for these tumors give testimony to the difficulties in applying such criteria.

Therefore, it is necessary to explore new methods that would improve the accuracy of classification of thyroid nodules.

2.5 Magnetic Resonance Spectroscopy in the Study of the Thyroid Nodules

There have been several works aimed at using ^{1}H NMR relaxation times of water as well as water content in evaluating thyroid lesions (18-22). Comparing their results of relaxation time data and peak ratios from *in vitro* NMR spectra, Johnson et al. (22) suggested that proton NMR spectroscopy may be the method of choice to characterize tissue *in vivo*. This is based on the fact that molecules other than water make important contributions to the MR characteristics of tumors (23).

Ex vivo ^{1}H magnetic resonance spectroscopy has been shown to provide an independent modality for the early detection and diagnosis of malignant tumors (24,25). The basis of the MRS method is the assumption that an altered cellular chemistry precedes tumor development and progression (26).

It has recently been reported that *ex vivo* proton magnetic resonance spectroscopy, performed on specimens taken from patients undergoing partial or total thyroidectomy, can discriminate between normal thyroid tissue and invasive thyroid cancer with a sensitivity and specificity of 100% (16,17). Figure 2.3 shows representative *ex vivo* ^{1}H spectrum from a normal thyroid tissue biopsy. Using the ratio of the peak intensities at resonances of 1.7 ppm and 0.9 ppm, all 10 histologically proven follicular carcinomas and all 19 other cancers (papillary, anaplastic and medullary) had a ratio below 1.1, while all 18 normals had a ratio above 1.1. The 69 histologically benign follicular neoplasms were separated into two groups: A) 44% having a benign spectral pattern (ratio > 1.1), and B) 56 % having a malignant spectral pattern (ratio < 1.1). It was hypothesized that Group-B follicular neoplasms might represent lesions showing pre-cancerous

characteristics not yet visible, although they did admit that this is not consistent with current medical views. Although group-B (56%), classified as "malignant", represents false positives and a specificity of 54%, no false negatives resulted, giving an overall negative predictive value of 100%. Therefore, it was postulated, that in this case, 44% of the patients with benign follicular lesions predicted to have a "benign" spectral pattern, could avoid surgery. This is the basis for an ongoing clinical trial in Australia (17) in which patients that present with a follicular lesion on FNA undergo a repeat FNA for analysis by ^{1}H MRS. Those patients found to have a "malignant" spectral pattern will undergo normal surgical excision, while patients with a "benign" spectral pattern are given the opportunity of conservative management, with a semi-annual clinical review, repeat FNA cytology and MRS. Of course, any indication of progression to a malignant pattern would result in surgery.

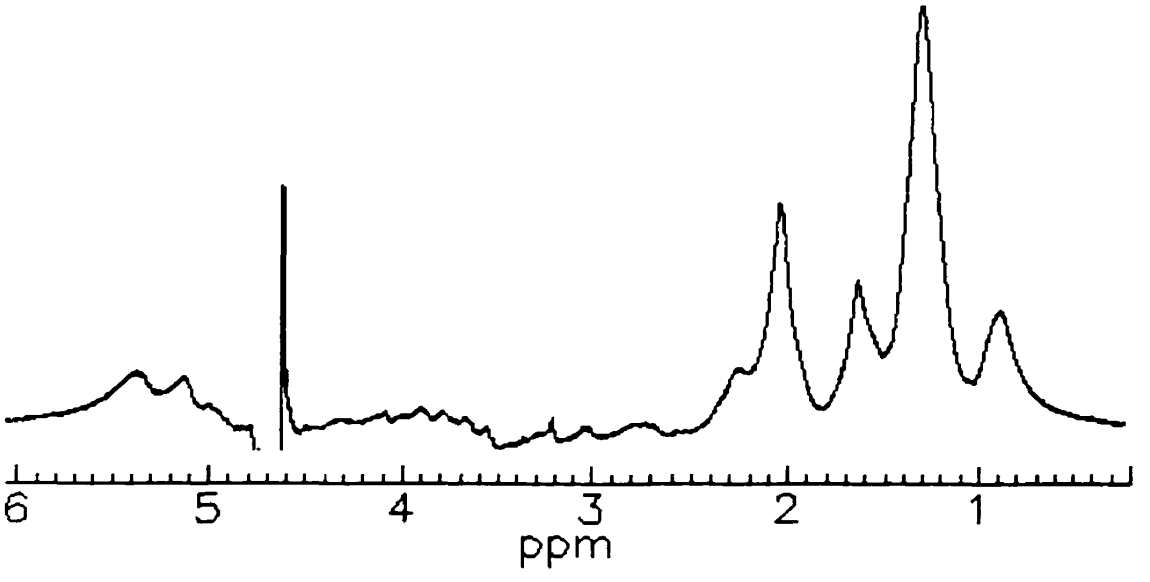

Figure 2.3 *Ex vivo* ^{1}H MR spectrum from a normal thyroid biopsy at 8.5 T (courtesy of Dr. C. Mountford, Institute for Magnetic Resonance Research, University of Sydney, N.S.W., Australia).

The same group has also shown recently, from 1-D and 2-D NMR results (27), that the ratio of the peak intensities at resonances of 2.05 ppm and 0.9 ppm also can be used as a diagnostic classifier of malignancy. They showed that a ratio below 1.12 correctly classified malignancy with a sensitivity of 97%, nearly as good as the original 1.7ppm/0.9ppm classifier, but more importantly, had a specificity (the probability of identifying patients without malignancy) of 72% was achieved compared to 44% using the original classifier.

More recently, *ex vivo* thyroid ^{1}H MR spectra were classified using computerized consensus diagnosis (CCD) which classifies spectra from the consensus result of several different computer classification algorithms (28). Here, mathematical methods are used to analyze the entire spectrum as a fingerprint, resulting in a high level of sensitivity and specificity for thyroid neoplasms. This approach classified the thyroid spectra into normal and malignant with 100% specificity and 100% sensitivity on training data sets, and 100% specificity and 98% sensitivity on test sets when compared to the histological diagnosis. This mathematical approach to analysis may be useful for *in vivo* studies where the less favorable conditions may not allow peaks to be resolved well enough for meaningful peak ratios.

Based on the information obtained from 2D NMR spectroscopy (COSY) and published literature values, the resonance at 1.7 ppm is predominantly a composite of the $-CH_2-$ of lipid and the $-CH_2-$ of lysine (16,28). The 0.9 ppm resonance has contributions from the methyl ($-CH_3$) groups of lipid and amino acid metabolites. Principal differences found in the spectra of malignant tissue compared to those of normal tissue were the decrease in intensity of lipid resonances at 1.3 ppm ($-CH_2-$) and

5.3 ppm (–CH=CH–) and increased methyl resonances at 0.9 ppm due to amino acid metabolites. Other metabolite resonances commonly seen in *ex vivo* ^{1}H MR spectra of thyroid tissue are from N-acetylaspartate (NAA) at 2.0 ppm, creatine at 3.0 ppm and choline at 3.2 ppm.

Another study has been done showing chemical shift microimages of the 0.9 ppm resonance on follicular tumors of the human thyroid *ex vivo* (29). Chemical shift imaging (CSI) showed that follicular carcinomas and many histologically and clinically benign lesions were chemically heterogeneous at the cellular level, yet not morphologically apparent. It was postulated that the areas of higher methyl intensity could be associated with malignant cells or foci of potentially malignant cells, indicating a premalignant state.

2.6 In Vivo MRS of Thyroid Nodules: Purpose and Objectives

To date, the only attempt at obtaining MR spectra from thyroid lesions *in vivo* was one of low quality, used only as a demonstration of the potential use of *in vivo* proton spectroscopy for the diagnosis of head and neck lesions (30).

The goal of the present work is to develop a method of investigating thyroid nodules *in vivo* using magnetic resonance imaging to locate the tumor and ^{1}H magnetic resonance spectroscopy to characterize the neoplasm. Advantages of the *in vivo* technique are that it is non-invasive, does not require any surgical procedure or biopsies, and explores the entire neoplasm, thereby eliminating the sampling problem of conventional histopathology. Furthermore, with the use of advanced multivariate methods of spectral data analysis, a non-subjective classification can be achieved.

In vivo ^{1}H MR spectroscopy of the thyroid gland is more complex than *in vivo* MRS studies of the brain. The small size of the gland means that spectra are taken from small volumes resulting in a low signal-to-noise ratio. Since the thyroid gland is found wrapped around the trachea, there is a large B_0 inhomogeneity from the magnetic susceptibility differences of the tissue-air interface that can cause immense linewidth broadening. Although the thyroid is relatively superficial and therefore allows high sensitivity surface coils to be employed, it also means that there is another tissue-air interface that will further broaden spectral lines. Spectra are also more sensitive to contamination from the surface layer of muscle or fat. The carotid artery and jugular veins lie next to the thyroid, creating motion artifacts in both MR imaging as well as spectroscopy. There are two additional sources of line broadening from respiration. Respiration will cause line broadening from the physical motion of the thyroid gland, but a larger contribution comes from the magnetic susceptibility changes associated with the inspiration and expiration of air to the lungs. A microimaging study on thyroid neoplasms also showed that although follicular lesions are composed of morphologically homogenous follicular cells and colloid, spectroscopic imaging revealed that the tissue was chemically heterogeneous (29). Therefore, in order to measure mean metabolite concentrations quantitatively over a heterogeneous tissue volume such as thyroid tumors, it is important to use a technique that receives signal uniformly over the volume of interest (31).

Given the above challenges, the first objective of this research was to develop a robust method that maximizes the SNR of thyroid spectra with optimum resolution. Techniques were sought that compensate for the various line-broadening mechanisms. The RF coil and pulse sequence had to be chosen to optimize not only the SNR, but also other spectral

characteristics such as localization quality, water suppression and outer voxel contamination. These methods were designed and tested on normal thyroid glands according to technique development protocols submitted to and approved by the Research Ethics Board of the National Research Council of Canada.

The second objective was to collect ^{1}H MR spectra from normal, as well as benign and malignant thyroid nodules according to the patient study protocol submitted to and approved by the Research Ethics Board of the National Research Council of Canada, and to determine the MR spectral characteristics of normal thyroid and thyroid nodules. The ultimate goal was that *in vivo* MRS would be able to discriminate between normal thyroid and thyroid carcinoma.

2.7 In Vivo MRS of Thyroid Nodules: Hypothesis

Previous *ex vivo* MRS results of biopsies from thyroid neoplasms support the hypothesis that MRS would be a useful tool in the diagnosis of thyroid tumors (16,17,28). It is hypothesized that:

(a) A robust *in vivo* ^{1}H MRS method, that will generate high quality spectra from the thyroid gland of humans, can be developed.

(b) Differences will be seen in the ^{1}H MR spectra of normal and benign thyroid nodules compared to those of thyroid carcinoma, making it possible to discriminate between normal human thyroid and malignant thyroid neoplasms.

2.8 References

1. Robbins, J. "Thyroid Gland and its Hormones", Encyclopedia of Human Biology Vol. 7, pp. 483-491, Editor Renato Dulbecco, Academic Press, Inc. San Diego, 1991.
2. Grant's Atlas of Anatomy 9th Ed., Editor Anne M.R. Agur, Williams & Wilkins, Baltimore, pp. 570-605 (1991).
3. Gray's Anatomy 38th Ed., Editor Peter L. Williams, Churchill Livingston, New York, p. 1893 (1995).
4. Cecil Textbook of Medicine, 18th Ed. James B. Wyngaarden, Lloyd H. Smith Jr., J. Claude Bennett, XVII Endocrine and Reproductive Diseases pg. 1294-1297, W.B. Saunders Company (1992).
5. E. L. Mazzaferri, Thyroid cancer in thyroid nodules: finding a needle in a haystack. *Am. J. Med.* **93**, 359-362 (1992).
6. Giuffrida, H. Gharib, Controversies in the management of cold, hot and occult thyroid nodules. *The American Journal of Medicine* **99**, 642-650 (1995).
7. E. L. Mazzaferri, Management of a solitary thyroid nodule. *N. Engl. J. Med.* **328**(8), 553-559 (1993).
8. E. L. Mazzaferri, E. T. de los Santos, S. Rofagha-Keyhani, Solitary thyroid nodule: diagnosis and management. *Med. Clin. North Am.* **72**, 1177-1211 (1988).
9. Robbins Pathologic Basis of Disease 4th Ed., W.B. Saunders Company 1994, Ch. 26 The Endocrine System, p. 1214-1241.
10. A. Belfiore, G. L. La Rosa, G. A. La Porta, D. Giuffrida, G. Milazzo, L. Lupo, C. Regalbuto, R. Vigneri. Cancer risk in patients with cold thyroid nodules: relevance of iodine intake, sex, age, and multinodularity. *Am. J. Med.* **93**, 363-369 (1992).
11. 1998 Cancer Statistics, American Cancer Society Web Site (www.cancer.org), © American Cancer Society.

12. C. Hedinger, E. D. Williams, L. H. Sobin, The WHO histological classification of thyroid tumors: a commentary on the second edition. *Cancer* **63**, 908-911 (1989).

13. L. A. Akslen, Thyroid cancer: some aspects of epidemiology and etiological factors, pathological features and tumor biology (Review). *International J. of Oncology* **4**, 931-942 (1994).

14. V. A. Li Volsi, Follicular lesions of the thyroid. In: Li Volsi VA, ed. Surgical pathology of the thyroid. Chap. 9, Vol. 22. Philadelphia: Saunders; 173-212 (1990).

15. R. A. Prinz, Invited commentary from L. Delbridge, C. L. Lean, P. Russell, G. L. May, S. Roman, S. Dowd, T. S. Reeve, C. E. Mountford, Proton magnetic resonance and human thyroid neoplasia II: potential avoidance of surgery for benign follicular neoplasms. *World J. Surg.* **18**, 512-517 (1994).

16. P. Russell, C. L. Lean, L. Delbridge, G. L. May, S. Dowd, C. E. Mountford, Proton magnetic resonance and human thyroid neoplasia I: discrimination between benign and malignant neoplasms. *Am. J. Med.* **96**, 383-388 (1994).

17. L. Delbridge, C. L. Lean, P. Russell, G. L. May, S. Roman, S. Dowd, T. S. Reeve, C. E. Mountford, Proton magnetic resonance and human thyroid neoplasia II: potential avoidance of surgery for benign follicular neoplasms. *World J. Surg.* **18**, 512-517 (1994).

18. M. Schara, M. Sentjurc, M. Auersperg, et al., Characterization of malignant thyroid gland tissue by magnetic resonance methods. *Br. J. Cancer* **29**, 483-486 (1974).

19. J. de Certaines, J. Y. Henry, G. Lancien, L. Benoist, A. M. Bernard, G. Le Clech, Evaluation of human thyroid tumors by proton nuclear magnetic resonance. *J. Nucl. Med.* **23**, 48-51 (1982).

20. J. Tennvall, A. Biörklund, T. Möller, M. Olsson, B. Persson, M. Åkerman, Studies of NMR-relaxation-times in malignant tumors and normal tissues of the human thyroid gland. *Prog. Nucl. Med.* **8**, 142-148 (1984).

21. J. Tennvall, M. Olsson, T. Möller, M. Åkerman, J. Ranstam, A. Biörklund, H. Mårttensson, B. Persson, Thyroid tissue characterization by proton magnetic resonance relaxation time determination. *Acta Oncologica* **26**, 27-32 (1987).

22. M. Johnson, B. Selinsky, M. Davis, T. L. Lawrence, G. Cleveland, R. Perry, C. G. Thomas, L. Kwock, In vitro NMR evaluation of human thyroid lesions. *Invest. Radiol.* **24**, 666-671 (1989).

23. C. E. Mountford, L. E. Wright, K. T. Holmes, W. B. Mackinnon, P. Gregory, R. M. Fox, High-resolution proton nuclear magnetic resonance analysis of metastatic cancer cells. *Science* **226**, 1415-1418 (1984).

24. A. C. Kuesel, T. Kroft, J. K. Saunders, M. Préfontaine, N. Mikhael, I. C. P. Smith, A simple procedure for obtaining high quality NMR spectra of semiquantitative value from small tissue specimens: cervical biopsies. *Magn. Reson. Med.* **27**, 349-355 (1992).

25. C.E. Mountford, W. B. MacKinnon, E. J. Delikatny, P. Russell, High resolution proton MRS in cancer pathology. In: J. D. de Certaines, W. M. M. J. Bovee, F. Podo, eds. *Textbook of Magnetic Resonance Spectroscopy in Biology and Medicine*. New York: Pergamon Press, 507-526 (1992).

26. I. C. P. Smith, E. J. Princz, J. K. S. Saunders, Magnetic resonance spectroscopy in cancer research. *J. Can. Assoc. Radiol.* **41**, 32-38 (1990).

27. W. B. Mackinnon, L. Delbridge, P. Russell, C. L. Lean, G. L. May, S. Doran, S. Dowd, C. E. Mountford, Two-dimensional proton magnetic resonance spectroscopy for tissue characterization of thyroid neoplasms. *World J. Surg.* **20**, 841-847 (1996).

28. R. L. Somorjai, A. E. Nikulin, N. Pizzi, D. Jackson, G. Scarth, B. Dolenko, H. Gordon, P. Russell, C. L. Lean, L. Delbridge, C. E. Mountford, I. C. P. Smith, Computerized consensus diagnosis: a classification strategy for robust analysis of MR spectra. I. Application to ^{1}H spectra of thyroid neoplasms. *Magn. Reson. Med.* **33**, 257-263 (1995).

29. A. Rutter, B. Künnecke, S. Dowd, P. Russell, L. Delbridge, C. E. Mountford, Proton magnetic resonance and human thyroid neoplasia III. Ex vivo chemical-shift microimaging. *J. Magn. Reson., Series B* **110**, 240-248 (1996).

30. M. F. Mafee, M. Bárány, E. D. Gotsis, G. D. Dobben, J. Puklin, J. M. Chow, B. L. Wenig, Potential use of *in vivo* proton spectroscopy for head and neck lesions. *Radiologic Clinics of North America* **27**, 243-254 (1989).

31. S. B. King, L. N. Ryner, B. Tomanek, J. C. Sharp, I. C. P. Smith, MR spectroscopy using multi-ring surface coils (in press, accepted July 1999 to *Magn. Reson. Med.*).

Chapter 3

MR SPECTROSCOPY USING MULTI-RING SURFACE COILS

3.1 Introduction

The main disadvantage of using standard single-loop surface coils in magnetic resonance spectroscopy (MRS) (1) - a spatially inhomogeneous B_1-field - stems from their primary benefit - higher sensitivity close to the coil, relative to volume coils. When using a surface coil with otherwise excellent spatially-localized MRS techniques (2-4), this inhomogeneous transmit and receive RF field leads to a variety of disadvantages including imperfect spatial localization (4-6), poor water suppression (7), and increased contamination from outside the volume of interest (VOI) (5). In addition, one cannot measure mean metabolite concentrations quantitatively over a tissue volume if the coil response is non-uniform, unless an assumption is made concerning the metabolite spatial distribution. The inhomogeneous receive profile of a surface coil could result in different spectra of the same tissue, depending on the tissue-coil orientation - especially for heterogeneous tissues such as tumors - which would spoil attempts at tissue classification with MRS. Therefore, the use of an RF coil with a spatially uniform B_1-field is preferred for MR imaging and spectroscopy. Volume coils provide a uniform B_1-field, but are sometimes unavailable, or do not provide adequate RF power or SNR for some applications.

One strategy to overcome surface coil B_1 inhomogeneity relies on the use of separate transmit and receive coils. In this approach, the volume transmitter coil is designed for optimum B_1 homogeneity thereby producing a uniform flip angle distribution, while the receiver coil is designed for optimum sensitivity (8,9). However, large volume coils operating at high frequency require high RF power and therefore often produce an increased specific absorption rate (SAR), with B_1 homogeneity within the sample possibly compromised due to RF penetration effects (10-12). In addition, transmit/receive coil decoupling is also needed (13-15). Another solution is to use a concentric surface coil pair (13). In this case a small surface-coil receiver must also be decoupled from a larger surface-coil transmitter (13,16). To improve B_1 homogeneity during transmission, Styles *et al.* (16) allowed induced current to flow in the receive coil, controlled using crossed diodes and a transmission line. This way a homogeneous transmit B_1 field was produced near the surface of the coil but not at a specific depth of interest.

Another problem in using separate transmit/receive coils for spectroscopy is that, in general, the relative $\mathbf{B_1}$ field direction of the transmit and receive coils at a particular point in the sample is different. Therefore, phase changes in the magnetic moment at that position are not mirrored upon reception, resulting in irretrievable loss of signal and a sample-dependent signal phase (9,16,17). This effect may also degrade the efficacy of shimming procedures used in MR (16). The use of large surface coil or volume coil transmitters may also be impractical due to incompatibility with sample size and shape, for example, *in vivo* MRS within the anterior neck.

An alternative to these hardware solutions is the use of pulse sequence techniques, such as composite or adiabatic RF pulses. Recently, adiabatic 90° selective excitation pulses suitable for single shot localization sequences have been developed (18,19). However, such pulses place increased demands on RF power (hence increased SAR) and gradient performance (more likely to cause eddy current effects), in addition to limited minimum echo time (18).

All the above methods only address B_1 inhomogeneity during transmission, leaving an asymmetric voxel profile due to the inhomogeneous reception field (4-6).

In this chapter, new multi-ring transmit/receive surface coils are proposed which produce a B_1-field uniform over a specific VOI, and therefore, with standard volume localization MRS, are capable of localization performance essentially equivalent to that of a volume coil while maintaining the high signal-to-noise ratio (SNR) associated with surface coils (20). The aim of this work is to analyze the performance of the multi-ring surface coil in MRS (MRI using a double- and triple-ring version has been reported (21, J.L. Patrick et al. ISMRM 1986 p. 47)) and compare this to an optimal single loop circular ("standard") surface coil and a standard volume coil. In addition to comparing the B_1-homogeneity of the coils, local SAR, RF power requirements, SNR, water suppression (WS), and outer volume contamination in conjunction with STEAM localization will be analyzed. In general, any number of rings can be used to optimize the B_1 field homogeneity, but this chapter will focus on two- and three-ring designs.

3.1 Theory

3.1.1 Signal and B_1 Field Distribution

For a coil used as both transmitter and receiver, the B_1 field amplitude affects both the flip angle of the NMR excitation and the reception sensitivity. For a STEAM localization sequence (3), the total signal, S, received from the VOI is given by

$$S \propto \int_{VOI} \frac{|\mathbf{B}_1(\mathbf{r})|}{I} \sin\alpha(\mathbf{r}) \sin\beta(\mathbf{r}) \sin\gamma(\mathbf{r})\, dV \ , \qquad [3.1]$$

where α, β and γ are the flip angles experienced by the elemental volume dV at position $\mathbf{r}$, and $\frac{|\mathbf{B}_1(\mathbf{r})|}{I}$ is proportional to the receiver-coil sensitivity (22), where $\mathbf{B}_1(\mathbf{r})$ is the field produced by a current I ($\hat{\mathbf{B}}_1(\mathbf{r})$ for unit current). In our comparisons of different coil configurations we assume all other parameters are kept constant. We shall assume sample and coil sizes much smaller than the wavelength in the sample, and therefore RF penetration (10,11,23,24) and standing wave (11,25) effects on $\mathbf{B}_1(\mathbf{r})$ can be ignored. In this static approximation, the $\mathbf{B}_1(\mathbf{r})$ field produced by a surface coil at any point $\mathbf{r}$ in space, can be calculated from the Biot-Savart law. In the case of N separate rings, each carrying current I_p, the total field is simply a superposition of the fields from all the rings, such that

$$\mathbf{B}_1(\mathbf{r}) = \frac{\mu_0}{4\pi} \sum_{p=1}^{N} \oint_{l_p} \frac{I_p d\mathbf{l}_p \times (\mathbf{r} - \mathbf{r}_p)}{|\mathbf{r} - \mathbf{r}_p|^3}, \qquad [3.2]$$

where μ_0 is the magnetic permeability of free space, $d\mathbf{l}_p$ is the elemental current vector of magnitude I_p, $\mathbf{r}_p$ is the position vector of the element with respect to the origin, and the

line integral is along the conductor l_p. If the coil is lying in the x-z plane, the axial B_1 field strength along the y-axis is given by the familiar expression

$$B_{1y} = \frac{\mu_0}{2} \sum_{p=1}^{N} I_p \frac{a_p^2}{(a_p^2 + (y - y_p)^2)^{3/2}}, \qquad [3.3]$$

where a_p is the ring radius and y_p is the position of the p^{th} ring.

3.1.2 Noise, Power Deposition, SAR and SNR

Neglecting radiation resistance and noise from the receiver electronics, the noise voltage picked up by the receiver is proportional to the square root of the sum of the effective resistance of the sample (R_S) and the resistance of the coil itself (R_C) (22), so that

$$\text{Noise} \propto \sqrt{R_S + R_C}\,. \qquad [3.4]$$

The coil resistance (R_C) represents the total effective resistance under unloaded conditions. Sample resistance (R_S) results in power deposited in the sample. Dielectric loss within the sample (26) can be effectively minimized by using distributed capacitance and proper capacitor shielding. Therefore, only inductive losses associated with RF induced eddy currents, the major source of power deposition within the sample, will be considered (26).

The specific absorption rate (SAR) refers to the amount of RF power absorbed by the sample during a MR experiment. In the quasi-static approximation, the total power deposition (P) or total SAR is calculated from the induced current density which is proportional to the electric field, **E**, in the sample of constant conductivity σ, so that

$$P = \int_{Sample} P(\mathbf{r})dV = \frac{\sigma}{2} \int_{Sample} |\mathbf{E}|^2 dV, \qquad [3.5]$$

where $P(\mathbf{r})$ represents the spatial distribution of deposited power or the local SAR distribution within the sample. The rapid decrease in B_1 field with distance from a surface coil causes a majority of the power to be deposited near the coil and nearest to the conductor, creating local SAR "hot spots". Therefore, an analysis of the SAR characteristics of both types of surface coils was done.

For the N-ring surface coil, the induced electric field within the sample can be calculated from the vector potential $\mathbf{A}$ and Faraday's law as

$$\mathbf{E}(\mathbf{r}) = -\frac{d\mathbf{A}}{dt} = \frac{-\omega\mu_0}{4\pi} \sum_{p=1}^{N} \oint_{l_p} \frac{I_p d\mathbf{l}_p}{|\mathbf{r} - \mathbf{r}_p|}, \qquad [3.6]$$

where the integration is along the conductor of ring l_p, and ω is the frequency.

The effective resistance of the sample is equal to the total power deposited in the sample per unit squared coil current, that is

$$R_S = \frac{\sigma}{2} \frac{\int_{Sample} |\mathbf{E}|^2 dV}{I^2}, \qquad [3.7]$$

where $|\mathbf{E}|$ is the magnitude of the induced electric field produced by coil current, I. With knowledge of the unloaded Q-factor, $Q_U = \frac{\omega L}{R_C}$, and the loaded Q-factor, $Q_L = \frac{\omega L}{(R_S + R_C)}$, where L is the self-inductance of the coil, the resistance of the coil R_C can be calculated as

$$R_C = R_S \frac{Q_L}{Q_U - Q_L}. \qquad [3.8]$$

By combining Eq. [3.1] and Eq. [3.4], the total SNR can now be expressed as

$$\mathrm{SNR} \propto \frac{\int_{VOI} \frac{|\mathbf{B}_1(\mathbf{r})|}{I} \sin\alpha(\mathbf{r}) \sin\beta(\mathbf{r}) \sin\gamma(\mathbf{r})\, dV}{\sqrt{R_S + R_C}} . \qquad [3.9]$$

The intrinsic signal-to-noise ratio, $\mathrm{SNR_I}$, is found by setting $R_C = 0$.

3.1.3 Multi-Ring Surface Coil Theory

The multi-ring surface coil consists of N co-axial circular rings of different diameters (D_p), currents (I_p) and axial-positions (y_p). The geometry is depicted in Fig. 3.1, where an example of a three-ring coil is shown. Using the theory described below (see also ref. (21)), counter-rotating ring currents are possible, allowing the B_1 homogeneity to be optimized over a desired VOI.

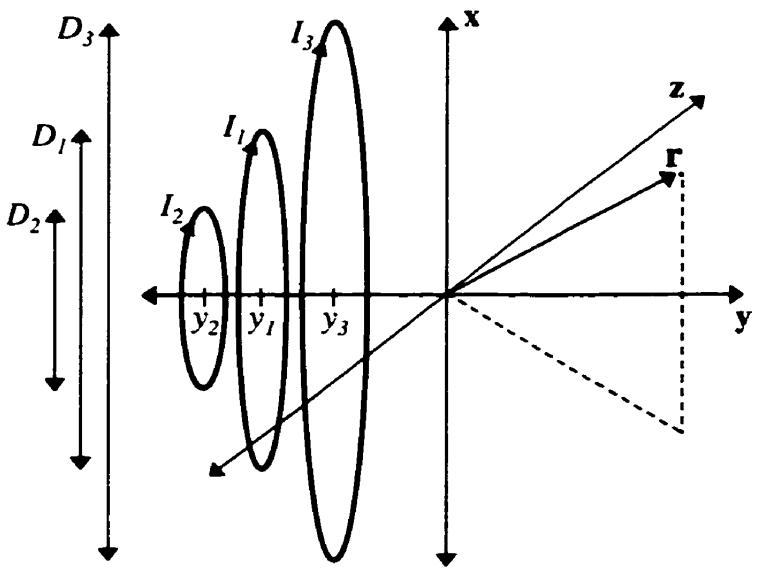

Figure 3.1 Geometrical model of the multi-ring surface coil (N = 3 shown). A current I_p flows in the p^{th} ring of diameter D_p that is positioned at y_p. The $\mathbf{B}_1$ field at any point $\mathbf{r}$ is calculated using the Biot-Savart law.

The mutual inductance, M_{pq}, between two rings l_p and l_q is given by (21,27)

$$M_{pq} = \frac{\mu_0}{4\pi} \oint_{l_p} \oint_{l_q} \frac{d\mathbf{l}_p \cdot d\mathbf{l}_q}{|\mathbf{r}_p - \mathbf{r}_q|}, \qquad [3.10]$$

where $\mathbf{r}_p$ and $\mathbf{r}_q$ are the position vectors of the elements $d\mathbf{l}_p$ and $d\mathbf{l}_q$ respectively. This mutual inductance can be exploited to provide the couplings necessary to distribute power appropriately from the transmitter, producing the required ring currents. For a high-Q coil, the voltage induced in any one ring is due to currents in the other N-1 rings (28). With this assumption, the voltage induced in the p^{th} ring is given from Lenz's law as $V_p = -j\omega_0 \sum_{q=1, q\neq p}^{q=N} M_{pq} I_q$, where I_q is the current in the q^{th} ring. Therefore, the reactance of the p^{th} ring is given by

$$X_p = \frac{V_p}{I_p} = -j\omega_0 \sum_{q=1, q\neq p}^{q=N} M_{pq} \frac{I_q}{I_p}, \qquad [3.11]$$

where $\frac{I_q}{I_p}$ is the current ratio for the q^{th} and p^{th} rings, which is pre-determined by the required B_1 field. A resonant circuit tuned to the Larmor frequency has, by definition, zero reactance. Therefore, to obtain the required ring-reactance (X_p) at the Larmor frequency (ω_0), it is necessary to tune each ring to a certain frequency ω_p different from ω_0.

The reactance of any ring that possesses both an inductance L_p and a capacitance C_p is given by

$$X_p = X_{L_p} + X_{C_p} = j\omega_0 L_p + \frac{1}{j\omega_0 C_p}. \qquad [3.12]$$

The ring inductance can be approximated as $L_p \approx \mu_0 a_p \{\ln(8\frac{a_p}{b_p}) - 2\}$ (29), where a_p is the radius of the p^{th} ring and b_p is the radius of its cylindrical conductor.

The tuning capacitance required for each ring can be determined by equating the reactances in Eq. [3.11] and Eq. [3.12], such that, $\frac{1}{j\omega_0 C_p} = X_p - X_{L_p}$. The resonant frequency of each ring is then given by

$$\omega_p = \frac{1}{\sqrt{L_p C_p}}. \qquad [3.13]$$

After tuning each of the N-rings to the appropriate frequency ω_p, they are brought together to form the multi-ring surface coil. The N-rings couple to create N-resonant modes each at a different frequency. In our multi-ring surface coil designs, it is the highest frequency mode that has the desired Larmor frequency (ω_0) and B_1 response.

3.1.4 Variable Depth Multi-Ring Surface Coil

The multi-ring surface coil can be designed to give excellent B_1 homogeneity at a specific depth from the coil. In most *in vivo* situations, the depth of the tissue of interest will vary from subject to subject. Therefore, to fully utilize the effectiveness of the multi-ring surface coil, there should be a method of adjusting the depth profile to account for these variations.

This can be accomplished in three ways: varying the diameters of the rings, varying the position of the rings, varying the ring current ratios; or a combination of the above. Obviously, varying ring diameter would not be feasible and varying the position of the rings would require a complicated mechanical process. By far the simplest method is to

alter the current ratios by varying ring frequencies, using a variable capacitance on each ring.

3.2 Methods

(i) Coil Design and Construction

The main aim of the multi-ring surface coil design is to achieve better B_1 homogeneity within the VOI, compared to standard surface coils, for improved localization, and with a minimum penalty in SNR. Design begins with optimization of the B_1 homogeneity over a specified volume. This can be accomplished with a variety of multi-ring surface coil parameters; number of rings (N), diameter (D_p), position (y_p) and current (I_p), using Eq. [3.2] and Eq. [3.3]. The localization quality is demonstrated through computer simulations of the voxel profile. The second design objective is to have a minimum loss in SNR performance, so therefore, in addition to B_1 homogeneity and localization quality, SNR is also calculated to determine the optimal design. The above procedures are then iterated until the optimum coil is found.

For predicting the variation in B_1 response for a variable-depth multi-ring surface coil, the ring diameters and positions were held constant, and the current ratios were adjusted to achieve firstly a minimum and secondly a maximum in the depth response corresponding to the predicted variation of depth for the tissue of interest, in this case, the thyroid gland. In the case of a three-ring coil, the current ratios were adjusted such that the frequency of the third ring remained constant. Therefore, in practice, depth variability could be achieved with adjustments of only two capacitors, avoiding the complicated adjustment of the third-ring capacitor.

Rings were constructed from copper tubing and segmented so that the capacitance was distributed evenly to reduce conservative electric field losses within the sample. Remaining dielectric losses were minimized with copper foil shields placed between the ring and the sample, underneath the capacitors. Non-magnetic, high-Q trimmer capacitors (Johanson, USA) were used for tuning the rings. An inductively coupled matching ring, tuned to the Larmor frequency of 127.77 MHz, was used. Inductive rather than capacitive coupling has the advantage that tuning and matching of the coil are independent and no electrical connection to the resonant coil is needed. The standard single-loop surface coil used for coil assessment comparisons was also inductively matched. For comparisons to a volume coil, a circularly-polarized (CP), 16 element, high-pass birdcage head coil (30 cm long, 26 cm diameter) (Morris Instruments Inc., Canada) was used.

(ii) Assessments of Coil Performance

3.2.1 Simulations Model

For all simulations, the STEAM sequence was applied to select a 1 cm^3 voxel at a depth of 2.0 cm below the surface of a phantom. A 0.5 cm gap was assumed between the coil and the phantom surface so that the distance from the center of a circular surface coil to the voxel is d = 2.5 cm. The simulation model is depicted in Fig. 3.2.

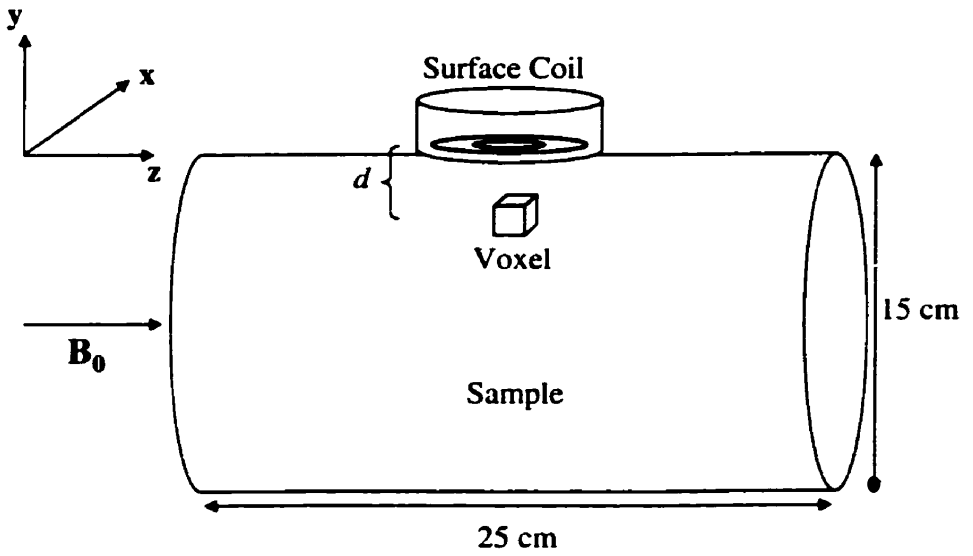

Figure 3.2 Depiction of the sample model and the geometrical arrangement of the surface coil and voxel. The large cylinder of diameter 15 cm and length 25 cm represents the sample. The voxel is shown placed a distance d = 2.5 cm from the center of the surface coil's conductor(s). This includes a separation from the sample surface of 0.5 cm and the depth of the voxel within the sample of 2.0 cm. The $\mathbf{B}_0$ field is in the z-direction and the axis of the surface coil is along the y-axis.

3.2.2 Signal-to-Noise Ratio

The diameter of a standard single loop circular surface coil may be chosen to give maximum SNR at a particular point within a sample (30-34). If sample losses are negligible such that electrical losses in the resonator dominate (primarily due to losses associated with the tuning capacitors and coil resistance), then at a depth d from the center of the coil conductor, maximum SNR occurs for radius $a = \sqrt{2}\,d$ (35). On the other hand, when the noise is dominated by inductive losses due to RF-induced eddy

currents in the sample, maximum SNR is given by the intrinsic signal to noise (SNR_I). In this case maximum SNR_I will be obtained for $a = \frac{d}{\sqrt{5}}$ (30,34).

To determine the optimum surface coil diameter with respect to SNR, the SNR was calculated for standard surface coils of different diameter based on the simulation model (Fig. 3.2) which included sample geometry, coil loading and the localization pulse sequence. The unloaded coil resistance (R_C) of a single loop circular coil is directly proportional to coil diameter and inversely proportional to the diameter of the coil conductor (33). We assume that the construction parameters (coil diameter and conductor diameter) of each surface coil are scaled such that the coil resistance (R_C) is the same (33), which results in R_C being independent of coil size. Therefore, with one experimental measurement of the loaded and unloaded Q-factor for a particular standard surface coil, R_C can be calculated from Eq. [3.8]. The SNR of various diameter surface coils can then be calculated using Eq. [3.9].

In the multi-ring surface coil case, R_C cannot be predicted from a single Q_U/Q_L measurement due to the variability of specific designs (ring diameters, separation, current ratios), so therefore R_C was not calculated. Instead, the intrinsic SNR was calculated using Eq. [3.9] with $R_C = 0$. This gives a reasonable approximation of the true SNR as found by experiment when sample losses dominate ($R_S >> R_C$).

3.2.3 B_1 Field Distribution and SAR

In order to compare B_1 homogeneity for the standard single loop and multi-ring surface coil, 1-D and 2-D B_1 fields were calculated from Eq. [3.3] and Eq. [3.2] respectively.

The total SAR for both types of surface coils was found from the input power used for the spectroscopy experiments (P_i) and scaled by the coil Q-values, since only a fraction of the input power used is deposited into the sample, given by $P_s = P_i\ (1 - \frac{Q_L}{Q_U})$ (36). SAR distributions were calculated from $P(\mathbf{r})$ in Eq. [3.5]. The peak local SAR was found by multiplying the maximum P(**r**), normalized to the calculated total power deposited (P of Eq. [3.5]) within the sample, by the total experimental power deposited (P_s) (37), such that $P(\mathbf{r})_{peak} = P_s\left(\frac{P(\mathbf{r})_{\max}}{P}\right)$.

Simulations of the B_1 field were compared to experiment with bench measurements of the axial B_1 field magnitude under loaded conditions using a network analyzer. The loading apparatus consisted of a large hollow cylinder (20-cm diameter, 16-cm length) with a narrow, centimeter-ruled tube, placed down the center. The whole apparatus was sealed and filled with saline solution to produce the appropriate loading conditions. With the surface coil centered on top of the loader, over the opening of the centimeter ruled tube, a 2.8 mm diameter search probe was placed within the small tube and the output voltage was measured along the central axis in 1 mm increments.

Experimental 2-D B_1 field maps for the surface coils were measured from two gradient echo (GE) MRI images of different flip angles (38), on a 5.6 L cubic phantom filled with 20 mM $CuSO_4$ in 0.3% NaCl solution. A GE sequence (TR/TE = 250/7.8 ms,

FOV = 12 cm × 12 cm, slice thickness = 5 mm) was used with flip angles chosen to be approximately 90° and 45° at a depth of 2.0 cm to emphasize B_1 information at the depth of interest.

3.2.4 Volume Localization (STEAM)

The localization quality of the multi-ring surface coil relative to the standard surface coil was demonstrated by simulating the MRS voxel profile along the axis of the coil for a STEAM localization experiment. STEAM voxel profile simulations were obtained from numerical solutions of the Bloch equations by calculation of incremental spin rotations about the effective field (such as in Lawry *et al.* (5)) during application of a simulated STEAM experiment. A 2-D voxel image in the y-z plane was simulated using frequency selective sinc RF pulses (bandwidth = 2 kHz), with slice selection gradient strengths of 4.7 mT/m (same as experiment). A 16-step phase cycling scheme was employed to remove all but the stimulated echo coherence (39). A one dimensional voxel profile along the y-axis (depth direction) was then obtained by summing over the z-direction of the voxel image.

3.2.5 MR Spectroscopy Experiments

Experimental determination of the SNR (dummy scans (DS) = 4, number of scans (NS) = 16) and water suppression (DS = 4, NS = 128) from localized MR spectroscopy experiments was performed with STEAM (TR/TE = 2000/20 ms) on a 1.0 × 1.0 × 1.0 cm^3 VOI at a depth of 2.0 cm from the surface of a phantom. For voxel imaging and

water suppression, the phantom was filled with distilled water containing 20 mM creatine, 20 mM lactate and 0.3% NaCl.

Voxel images were found using the STEAM (TR/TE = 1000/27 ms) sequence, modified to include read and phase encoding gradients. The same 4.5L cylindrical phantom (25 cm long and 15 cm diameter) was used for all MRS experiments. Experimental voxel profiles were found from 1-D intensity maps taken along the coil axis direction of a voxel image in the y-z plane.

Water-suppressed ^{1}H spectra were taken from the volume of interest using three CHESS sequences (40) before the STEAM sequence, adjusted for maximum suppression factors. The water suppression factor was determined from the residual water peak height.

Experimental SNR measurements were obtained from a small hollow 1.4 × 1.4 × 1.4 cm^3 cube filled with 100% mineral oil and fixed at a depth of 2.0 cm from the surface of the same 4.5L phantom filled only with 0.3% NaCl. A 1.0 cm^3 voxel was chosen within the small cube (to reduce the possibility of outer voxel contamination) and unsuppressed spectra were taken. For SNR measurement on the head coil, the voxel was chosen at the center of the phantom. SNR was evaluated from the height of the mineral oil peak. The amount of contamination due to signal originating from outside the VOI was found from the amount of water signal present in these mineral oil spectra.

3.2.6 Variable Depth Multi-Ring Surface Coil Calibration

The varying depth response of the multi-ring surface coil was initially tested using the loaded bench measurement method of Section 3.2.3. Final calibration of the coil was

done *in vivo* with the phantom described above. First the variable capacitor on the largest ring was set to its minimum value (maximum ring frequency) and the capacitor on a second ring adjusted such that the overall resonant frequency of the coil was at the Larmor frequency. This corresponded to a maximum value (minimum ring frequency) for the second ring. In this situation, the depth response of the coil would be at its minimum value. A one dimensional voxel profile (for a 1-cm^3 voxel) was taken using the voxel imaging sequence described previously. The position of the voxel in the depth direction was varied until the voxel profile was optimized (symmetric and flat). This then corresponded to the depth for which an optimal single voxel experiment could be done. Using this setting as the reference position, the large ring capacitance was increased by about $1/5^{th}$ of its range. The new resonant frequency (lower) of the coil was noted, and the smaller ring capacitance was decreased until the coil was once again at the Larmor frequency. The optimum depth was again determined using the procedure above. This was repeated four more times with the last iteration being the maximum depth for optimum spectroscopy.

3.2.7 Computational and Experimental Environment

Calculations of B_1, SNR, SAR, multi-ring surface coil ring frequency and capacitance were performed in the UNIX C computer language for a cylindrical phantom 15 cm in diameter and 25 cm in length (Fig. 3.2). Voxel profiles calculated from nuclear spin rotations about the effective field were performed in UNIX FORTRAN77 over a 4 × 4 cm^2 FOV plane. Unloaded and loaded Q-factors of the surface coils were measured with a HP8752A network analyzer (Hewlett Packard, USA). MR experiments and coil

calibrations were carried out on a 3T, 1m whole body magnet (Magnex, UK) with a Bruker MSLX console (Bruker, Germany).

3.3 Results and Discussion

3.3.1 Coil Designs

To make a fair comparison between coils, an optimized single loop surface coil was designed. For SNR simulations, R_C was determined from a 5-cm diameter surface coil (measured Q-factors: Q_U = 300 and Q_L = 53). Figure 3.3 shows the variation of SNR with surface coil diameter using the simulation model. The 90° flip position was chosen to be in the center of the 1-cm^3 voxel (d = 2.5 cm from coil conductor) for all surface coils. A maximum in SNR occurs when the coil diameter is chosen to be approximately 4.0 cm. As expected, this diameter lies between the electrical loss dominant case of 7.1 cm ($2\sqrt{2}\,d$), and the intrinsic SNR or sample loss dominant case of ~ 2.25 cm as shown in Fig. 3.3. In addition to SNR, several other factors influence the choice of an optimal surface coil. A surface coil with a larger diameter is often used because of its larger FOV and reduced B_1 inhomogeneity, improved water suppression and decreased susceptibility to outer voxel contamination. Therefore, for a fairer comparison to the multi-ring surface coil, a 5.0 cm diameter standard surface coil (matching ring 3.2 cm in diameter) was chosen, since, as seen from Fig. 3.3, there is less than 6% penalty in SNR compared to a 4.0 cm surface coil optimized for SNR only.

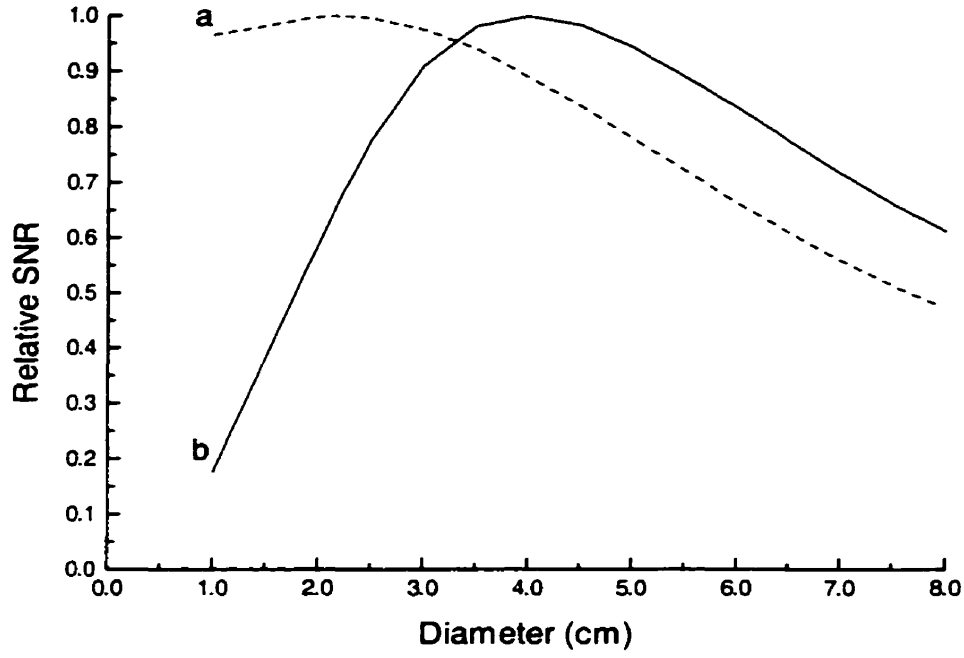

Figure 3.3 A plot of the calculated SNR versus diameter for a standard surface coil for a $1cm^3$ VOI at a depth of 2 cm from the phantom surface (separation of surface coil and phantom is 0.5 cm). (a) Intrinsic SNR and (b) SNR with R_c constant and equal to the coil resistance of a 5 cm diameter surface coil with Q_U = 300 and Q_L = 53. Plots were individually normalized to a maximum of 1.0.

Optimized through simulations, two multi-ring surface coils were designed. The first, was a two-ring coil (Fig. 3.4) designed for homogenous B_1 over the VOI described above. The two co-planar and co-axial rings consisted of a "main" ring 5 cm in diameter with a conductor radius of 2.2 mm and a smaller "B_1-shaping" ring 2.5 cm in diameter with a conductor radius of 1.6 mm with opposite current 1.13 times that of the main ring current. In an attempt to improve SNR, a second coil was designed consisting of three-rings, the first two identical to the two-ring surface coil and a third ring designed to reduce the total power deposited in the sample. The third ring was 15 cm in diameter

with a conductor radius of 3.2 mm and opposite current of 0.09 relative to the "main" ring. The same 3.84 cm diameter matching ring was used for both multi-ring surface coils.

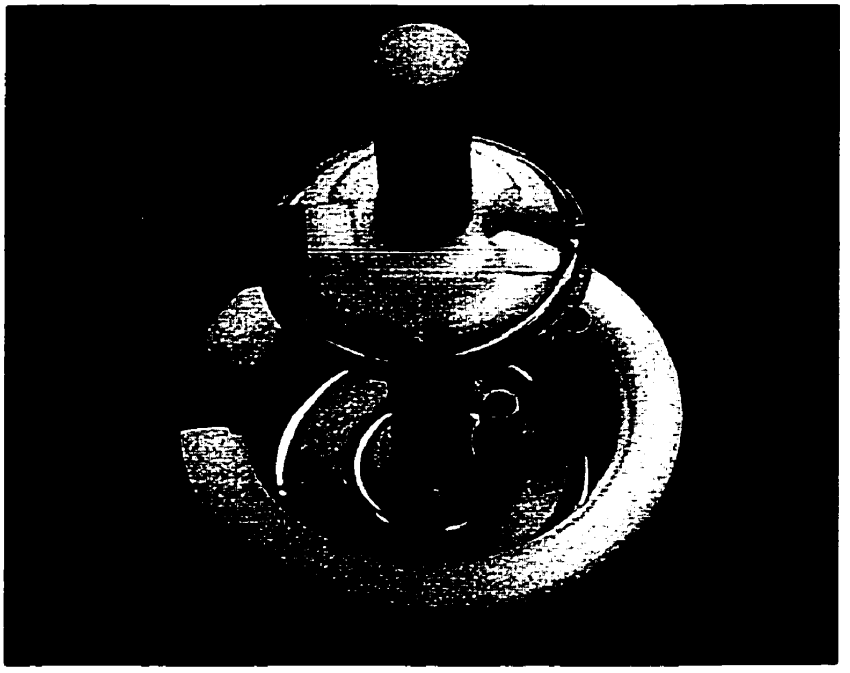

Figure 3.4 A photograph of the two-ring surface coil. The "main" ring has diameter 5 cm, the smaller "B_1-shaping" ring has diameter 2.5 cm and the inductively coupled matching ring has diameter 3.84 cm. The coil is tuned with the variable capacitors and independently matched by adjusting the height of the matching ring.

The design parameters of the multi-ring surface coils are shown in Table 3.1, giving the calculated ring frequencies in isolation. To accommodate changes in individual ring frequencies under loaded conditions, the loaded ring frequencies were adjusted to be the same as those calculated in isolation (Table 3.1) and thereby ensuring proper current ratios. This method resulted in a loaded B_1 response nearly identical to that predicted from calculations (Fig. 3.5). The loaded and unloaded Q-factors for the surface coils are

shown in Table 3.2. The elevated Q_L of the multi-ring surface coil can be attributed to less power being deposited in the sample for unit current.

Table 3.1 Multi-Ring Surface Coil Design Parameters

Coil	Ring, p	D_p (cm)	b_p (mm)	I_p/I_1	ν_p (MHz)*	C_p (pF)
#1	1	5.0	2.2	1	114.1	25.43
	2	2.5	1.6	-1.13	102.3	71.67
#2	1	5.0	2.2	1	111.2	26.79
	2	2.5	1.6	-1.13	105.5	67.39
	3	15.0	3.2	-0.09	90.5	9.29

* Larmor frequency = 127.77 MHz.

Table 3.2 Measured loaded and unloaded *Q*-values for the standard and multi-ring surface coils

	Q_U	Q_L
Standard Surface Coil	300	53
Two-Ring Surface Coil	330	90
Three-Ring Surface Coil	325	118

3.3.2 B_1 Homogeneity

The axial 1-D B_1 field plots (Fig. 3.5) clearly show the improved B_1 homogeneity within the VOI for the two-ring surface coil over a standard 5-cm single loop surface coil. A comparison of the calculated axial B_1 field and the B_1 measured on the bench under loaded conditions is shown. The standard surface coil plot is scaled so that the calculated B_1 field produced at the sample surface is unity. The smaller "B_1-shaping" ring of the two-ring surface coil should have only a small effect on B_1 far from the coil.

Therefore, since both the standard surface coil and the "main" ring of the two-ring surface coil are 5 cm in diameter, the B_1 plots are scaled so that the faraway fields are equal. There is good agreement between the calculations and the loaded measurements (Fig. 3.5). The reduced B_1 magnitude at the voxel location with respect to the standard surface coil is a consequence of the negative current in the "B_1-shaping" ring, and causes a loss in sensitivity of the multi-ring surface coil. For a quantitative measure of the B_1 homogeneity, the flip angle along the coil axis within the 1.0 cm voxel was calculated from the simulated 1-D field. For the standard surface coil, the maximum and minimum flip angles were 121° and 67° respectively (or 90° ± 27°) whereas for the multi-ring coil the maximum and minimum flip angles were 95° and 85° respectively (or 90° ± 5°).

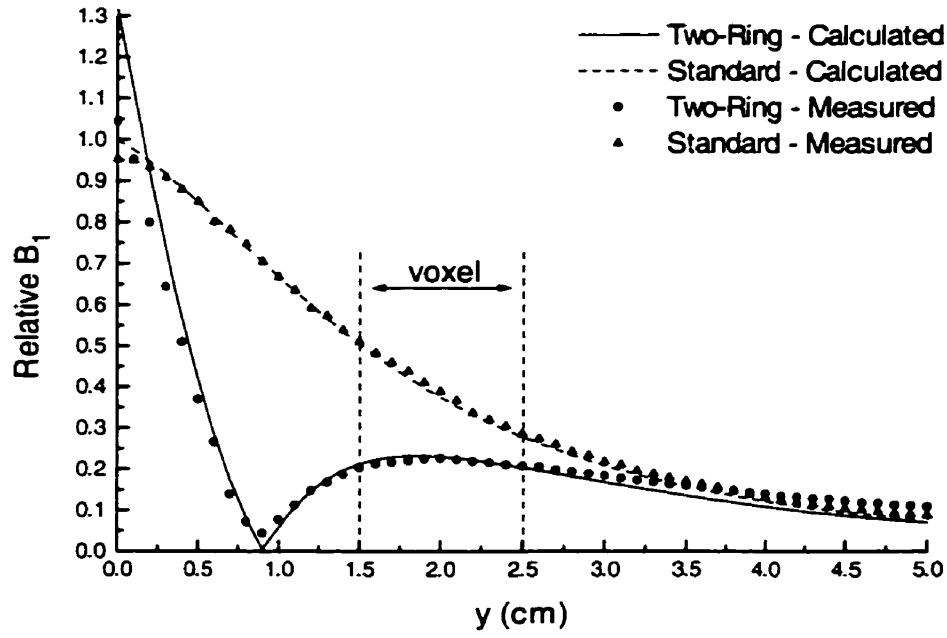

Figure 3.5 Calculated and loaded bench measurement of the B_1 field magnitude along the surface coil axis for the two-ring surface coil and the traditional surface coil. The size and position of the VOI is shown.

Two-dimensional calculated B_1 field distributions in the y-z plane are shown in Fig. 3.6A and Fig. 3.6B. For comparison, an experimental B_1 field map in the y-z plane is shown in Fig. 3.6C. Not only is there a more homogeneous B_1 within the VOI, but also a nulling of field about 1 cm from the sample surface. This effect could result in lowered contamination from signal outside the VOI as well as lowered noise pick-up when compared to standard surface coils.

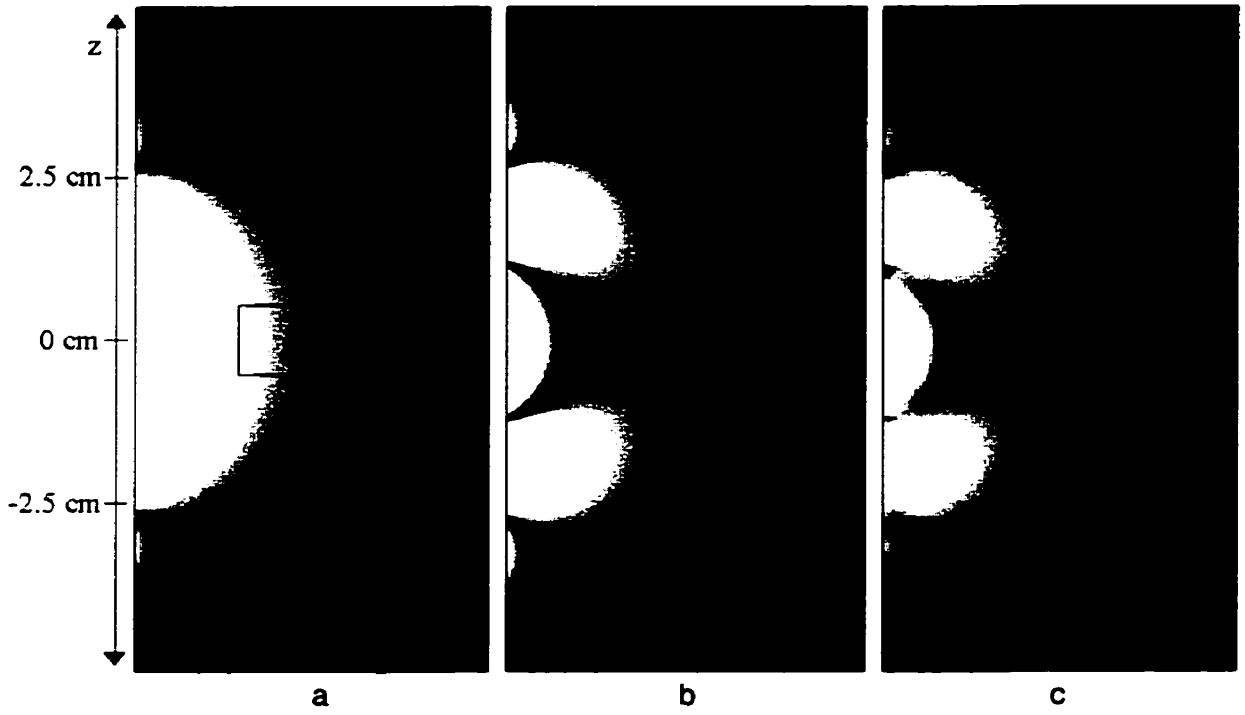

Figure 3.6 Calculated 2-D B_1 field distribution (y-z plane) for (a) the traditional surface coil and (b) the two-ring surface coil. (c) Experimental B_1 field map for the two-ring surface coil. Images are scaled to show the B_1 homogeneity within the VOI indicated.

3.3.3 Volume Localization

The excellent localization quality of the multi-ring coil is demonstrated by images of the selected VOI and by signal profiles through the VOI. Because the multi-ring and standard surface coils are used in transceive mode, the localization quality depends upon

the 90° flip position along the y-direction within the voxel, which is controlled by adjusting the RF power used in the STEAM localization. In addition to the voxel homogeneity, optimization of other spectroscopic factors such as contamination, WS and SNR is also required to determine the ideal input power. Both theoretically and experimentally, it was found that the best overall MRS localization for the standard surface coil was for the 90° flip chosen to be approximately at the center of the voxel. In the case of the two-ring surface coil, the 90° flip is set closer to the coil. That is, for a 1 cm^3 voxel at a position y = 2.0 cm from the sample surface, the 90° flip is set at a position, $y \approx 1.7$ cm. Simulated voxel profiles are shown in Fig. 3.7, for both types of surface coils and a volume coil. Simulations show that the two-ring surface coil produced a symmetric and homogenous response similar to a volume coil whereas the standard surface coil has the characteristic asymmetric axial profile. For comparison, simulated voxel profiles are also shown, where the standard surface coil is used as receive-only, with uniform excitation (volume coil or adiabatic pulses). The asymmetric voxel profile still occurs and again could result in inaccurate quantitation of average metabolite concentration from heterogeneous tissue.

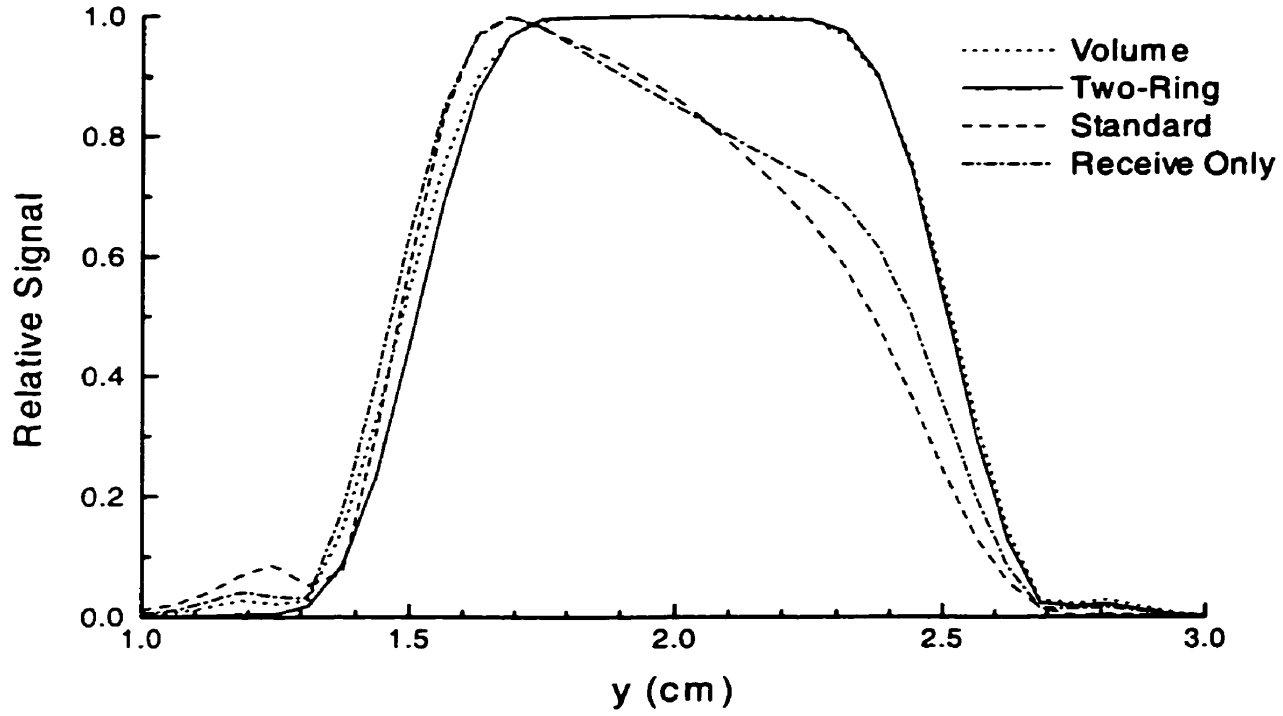

Figure 3.7 Simulated voxel profiles for a volume coil (dotted line), the two-ring surface coil (solid line), the standard surface coil (dashed line), and the standard surface coil used as receive-only (uniform excitation) (dash-dot line). The 90° flip for the two-ring surface coil was at y ≈ 1.7cm from the sample surface.

Experimental STEAM voxel images in the y-z plane obtained with both the two-ring and standard surface coils and a CP head coil are shown in Fig. 3.8. The two-ring surface coil produced a homogenous VOI image similar to that of the head coil, whereas the standard surface coil has the characteristic asymmetric response. Experimental voxel profiles along the y-axis, shown in Fig. 3.9, clearly illustrate the similarity of localization with the two-ring surface coil and the volume coil. The axial profile again demonstrates the improvement over the standard surface coil. There is very good agreement between the simulated and experimental axial voxel profiles, as shown in Figs. 3.7 and 3.9.

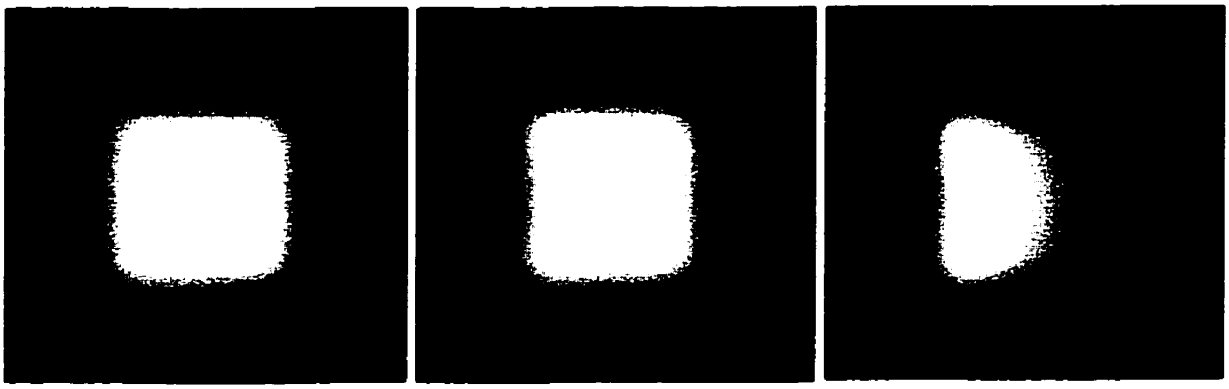

Figure 3.8 Experimental voxel images obtained with STEAM using (a) a circularly polarized head coil, (b) the two-ring surface coil and (c) the standard surface coil. Surface coils are located to the left of the corresponding image. FOV shown is 2 cm.

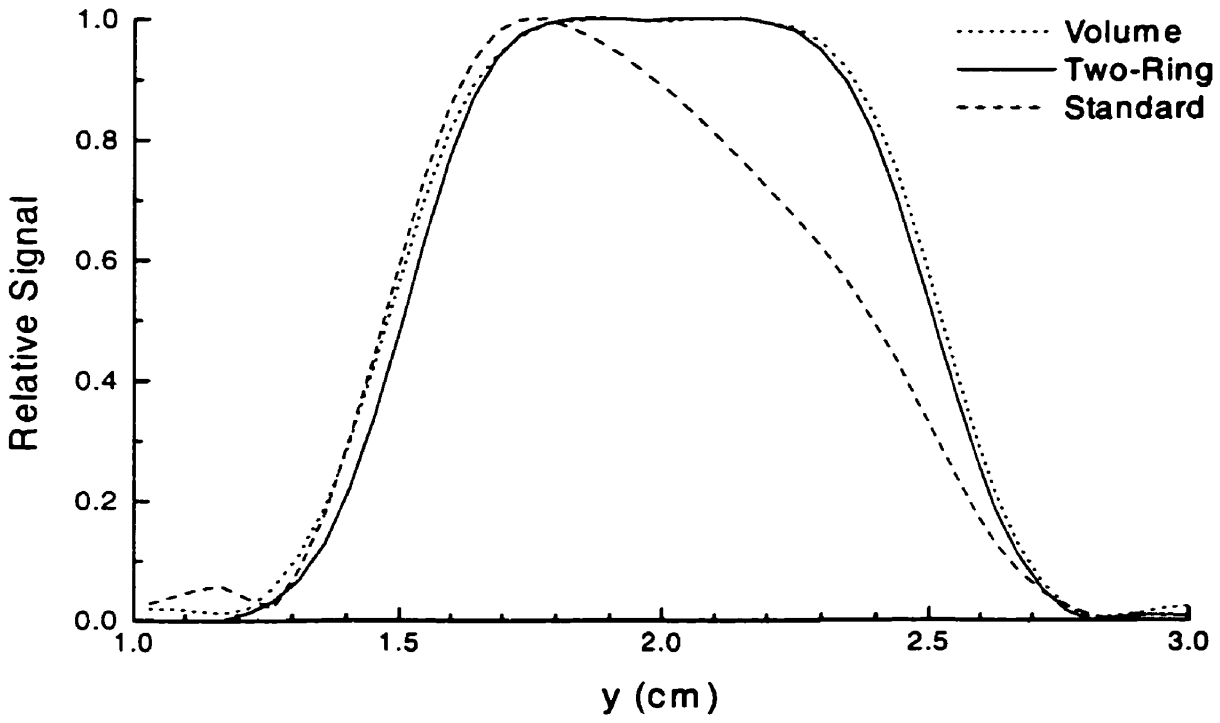

Figure 3.9 Experimental axial voxel profiles obtained with STEAM using a circularly polarized head coil (dotted line), the two-ring surface coil (solid line) and the standard surface coil (dashed line). The voxel is 1.0 cm in size, 2.0 cm from the surface of the sample.

3.3.4 Signal-to-Noise Ratio

Initially, intrinsic SNR values (column 4 of Table 3.3) were calculated to find the optimal multi-ring surface coil design. The first design (two-ring surface coil) provided localization characteristics similar to a volume coil and much improved over the standard surface coil. The experimentally determined SNR (column 6 of Table 3.3) for the two-ring surface coil was found to be 75% of that of the single-ring surface coil, a factor of 2.5 improvement in SNR over a circularly polarized head coil. The experimental SNR is in excellent agreement with the predicted SNR (column 5 of Table 3.3) found from Eq. [3.9] and the Q-values given in Table 3.2. It should be noted that the SNR was determined both theoretically and experimentally for a 90° flip angle position of $y \approx 2.0$ cm for the standard surface coil and $y \approx 1.7$ cm for the multi-ring surface coils. Small variations in SNR (as well as localization quality) were seen both theoretically and experimentally for different 90° flip positions. The increased loaded-Q value of 90 for the two-ring surface coil compared to the standard surface coil ($Q_L = 53$) indicates that there is less power being deposited in the sample and therefore less sample noise received. According to Eq. [3.9], the corresponding decrease in SNR implies that the noise reduction is accompanied by an even larger reduction in sensitivity (or $\hat{B}_1$) within the VOI.

Table 3.3 Localized STEAM Spectroscopy: Contamination, Water Suppression (WS), and Signal-to-Noise Ratio (SNR) relative to a standard 5cm single-ring surface coil

	Contamination	WS	SNR		
			Intrinsic	Predicted*	Experiment
Standard Surface Coil	1	1	1	1	1
Two-Ring Surface Coil	0.7	2.0	0.78	0.73	0.75
Three-Ring Surface Coil	----	----	0.94	0.83	0.85
CP Head Coil	----	4.0	----	----	0.3

*SNR calculated from the intrinsic SNR and R_C experimentally determined from Q_U and Q_L.

Based on simulations, the third ring of the three-ring surface coil (not used for thyroid studies), added for noise reduction, was expected to improve the intrinsic SNR by 17% over the two-ring surface coil. The experimental SNR was 85% of the standard surface coil, an improvement of 13% over the two-ring surface coil with the same localization quality. The loaded Q-value of 118 for the three-ring surface coil was significantly higher than for the two-ring version (Q_L = 90), with an increase in overall SNR. The additional increase in loaded-Q comes from a further reduction in coupling to the sample, particularly at positions of greater depth away from the voxel. In this case, a significant reduction in sample noise was accompanied by only a small loss in sensitivity (or $\hat{B}_1$) within the VOI, resulting in an elevated SNR.

Although we have focused on producing a more homogeneous B_1 field within a specified VOI and have therefore tolerated losses in sensitivity, a multi-ring surface coil could also be designed specifically for sample noise reduction and consequently improved SNR. This might be achieved with a two-ring surface coil consisting of a

"main" ring and a "noise-reduction" ring, similar to the third ring of our three-ring surface coil. SNR_I calculations show that up to 10% improvement in SNR over a standard surface coil could be expected, an effect also observed by another researcher (private communication, Dr. G. R. Duensing 1998).

As with standard surface coils, the SNR advantage of the multi-ring surface coil compared to a volume coil diminishes as the sample volume is made smaller and/or the VOI moved further from the surface, and closer to the center of the volume (31,33).

3.3.5 Specific Absorption Rate and RF Power Requirements

One of the advantages surface coils have over volume coils is lower RF power requirements. Table 3.4 compares the RF power required for spectroscopy and voxel imaging experiments (P_i), for the CP head coil (90° flip at y = 2.0 cm), standard surface coil (90° flip at y = 2.0 cm) and the multi-ring surface coils (90° flip at y = 1.7 cm). The quadrature volume coil required 11.1 dB (or 12.9 times) more power than the standard surface coil while the two-ring coil only required 4.5 dB (or 2.8 times) more. The additional power needed for these multi-ring surface coil designs can be attributed to decreased $\hat{B}_1$ with respect to the standard surface coil.

Calculated local SAR distributions for the standard and two-ring surface coil are shown in Fig. 3.10, where peaks in local SAR correspond to the conductor positions of the 5-cm rings. Results of the local and total SAR simulations are summarized in Table 3.4. As may have been expected from the additional power requirements, both the total and peak local SAR values are higher for the two-ring surface coil than for a standard

surface coil of similar dimensions. Although the total SAR is increased 2-fold, it is still much lower than typical volume coil total SAR limits.

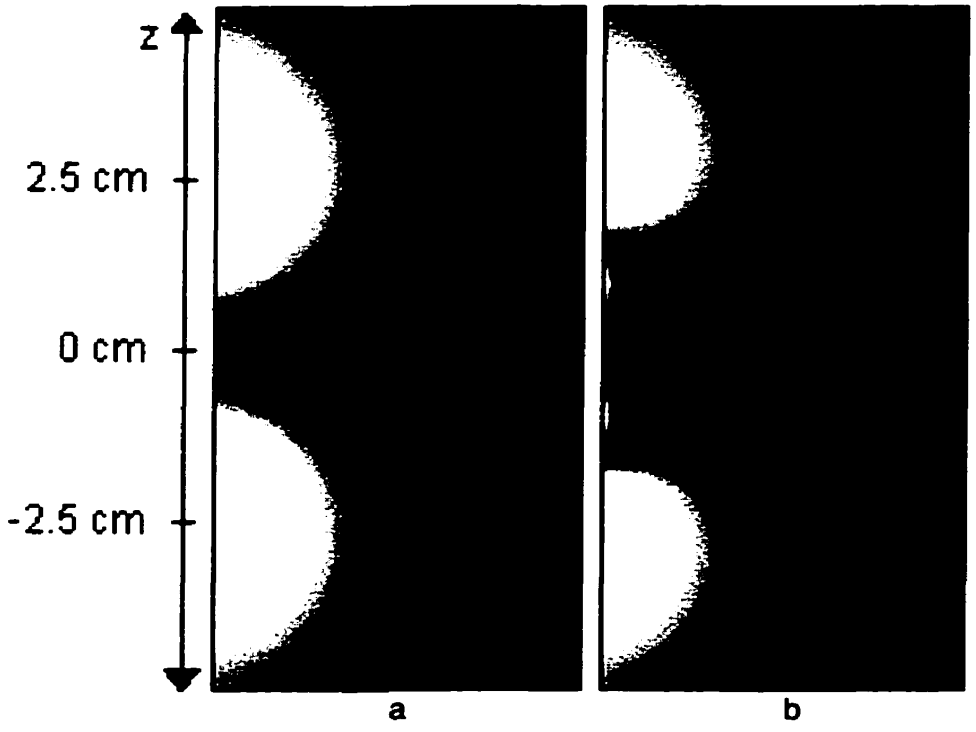

Figure 3.10 The local SAR distribution (y-z plane) as calculated from the spatial power deposition, $P(r)$ of Eq. [6], for (a) the standard surface coil and (b) the two-ring surface coil.

Table 3.4 RF power required as well as local and total SAR relative to a standard 5cm single-ring surface coil

	RF power (P_i)[a]	Total SAR[b]	Peak Local SAR
Standard Surface Coil	0 dB	1	1
Two-Ring Surface Coil	+4.5 dB	2.0	2.5
Three-Ring Surface Coil	+3.9 dB	----	----
CP Head Coil	+11.1 dB	----	----

[a]Input RF power used for spectroscopy experiments, referenced to the power delivered to the standard surface coil.

[b]Total SAR values are found from the input RF power and scaled with the Q-values.

3.3.6 Water Suppression and Outer Voxel Contamination

Without the use of adiabatic pulses, the efficacy of water suppression is dependent on the B_1 homogeneity of the transmit-coil used. The head coil gave the best water suppression, a 4-fold improvement over the standard surface coil, while the two-ring surface coil had a 2-fold enhancement.

Contamination from outside the VOI, usually near the sample surface, is a potential problem when using a surface coil for localized spectroscopy due to the high detection sensitivity close to the coil. Contamination was reduced by 30% with the two-ring surface coil compared to the standard surface coil. This is a consequence of the altered B_1 sensitivity near the coil, specifically the nulling effect seen in the B_1 plots (Fig. 3.6).

Although we have not focussed on nulling the B_1 field near the coil, right at the surface of the sample, a multi-ring surface coil could be designed specifically for this and consequent minimization of outer voxel contamination. This was the focus for the design of a third multi-ring surface coil, where the B_1 field was minimized near the surface of the coil and still optimized for homogenous B_1 field at the depth of interest. Therefore, if required, an additional penalty in SNR was tolerated.

3.3.6.1 A Multi-Ring Surface Coil for Reduced Contamination

The final multi-ring surface coil design optimized first for B_1 homogeneity and B_1-nulling at the surface, and second for SNR, consisted of three co-planar rings with diameters 6.5 cm, 3.0 cm and 2.0 cm and current ratios of 1.00, -1.59 and +1.20 respectively. All three rings were constructed from the same 3.2 mm diameter copper tubing, which resulted in ring frequencies of 119.3 MHz, 91.0 MHz and 73.0 MHz for the three rings respectively. In Fig. 3.11, the network analyzer S11 measurement

(reflection mode measurement) from the coil, loaded by the neck of a subject, shows three resonance modes for the three-ring surface coil. Again, it is the highest frequency mode (at 127.7 MHz) that corresponds to positive current in rings #1 and #3 and negative current in ring #2. Of course, this mode is degenerate with negative currents in rings #1 and #3 and positive current in ring #2.

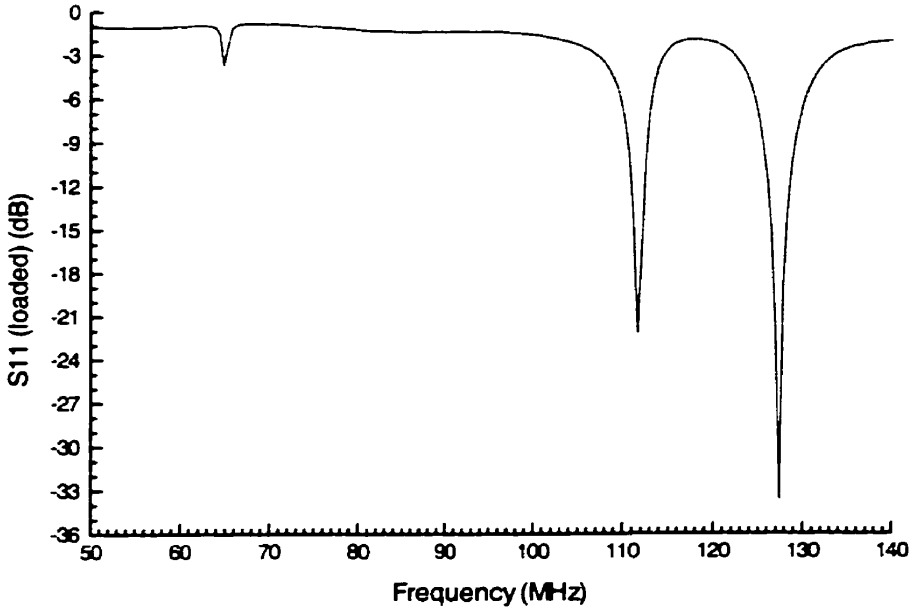

Figure 3.11 Reflection mode (S11) network analyzer measurement for the three-ring surface coil loaded by the neck of a subject.

The SNR obtained with this coil was approximately 65% of the traditional surface coil. The voxel profile and water suppression results obtained with this three ring surface coil were actually a little better than that of the two-ring coil, since it was a larger coil, with a larger region of uniformity. As might be expected, to accommodate the lower SNR, this three-ring coil required 1.5 dB more power than the two-ring surface coil. The contamination measured with this coil was 50% less than with the standard surface coil, a

further improvement over the two-ring version. An axial image of the neck is shown below, where the B_1-nulling region can easily be seen at the surface.

Figure 3.12 Axial image of the neck through middle section of the thyroid with the three-ring surface coil placed on top of the neck, displaced slightly to the subjects right side (left as seen above). Notice the null in sensitivity at the surface near the coil due to the surface B_1 nulling feature. Some ghosting from the carotid artery and jugular vein appear, but does not represent real signal.

In many subjects, there is often a layer of fat at the surface of the neck which presents a very high concentration of MR visible lipid signals. The region of zero B_1 at the surface of the neck virtually eliminates the possibility of lipid from this fat layer contaminating the MR spectrum from the thyroid.

3.3.7 Variable Depth Multi-Ring Surface Coil Calibration

The results of the depth calibration for the two-ring surface coil and the second three-ring are shown in Fig. 3.13 and Fig. 3.14. From the reference position of approximately 1.5 cm, the optimum depth of B_1 homogeneity of the coils can be chosen by varying the capacitor on the largest ring until the coil resonant frequency drops to the appropriate value, as determined from the calibration curves below. The capacitance of the smaller ring is then adjusted until the coil resonant frequency returns to the Larmor frequency.

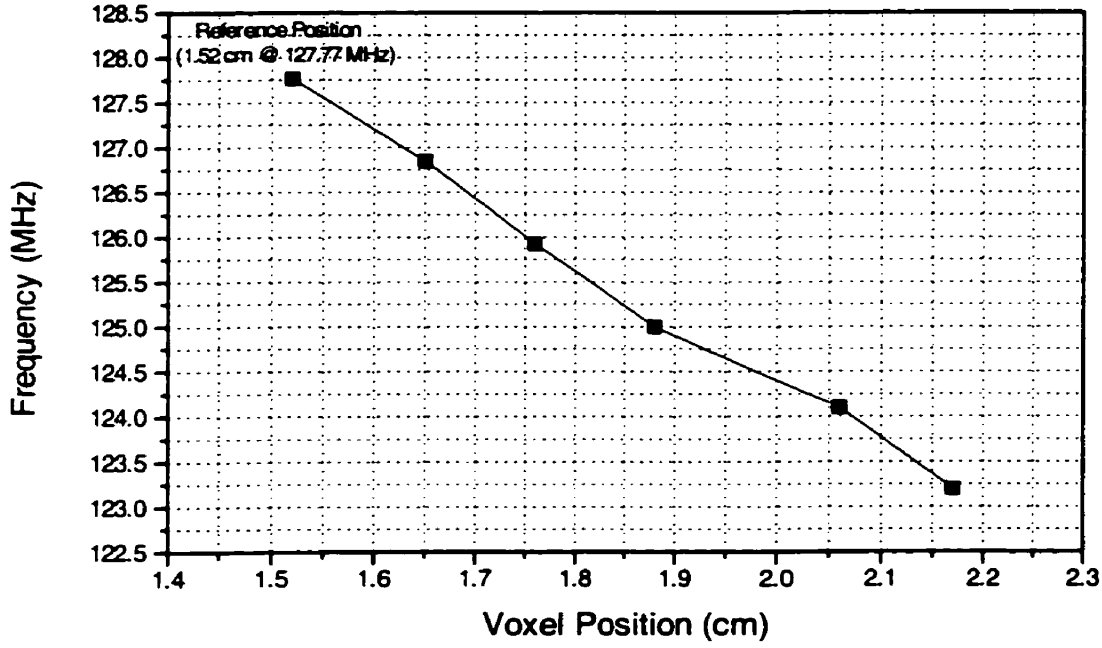

Figure 3.13 Calibration curve for the change in resonant frequency required to the two-ring surface coil (with varying the capacitance of the largest ring) to vary the depth of optimum localized spectroscopy from the surface of the sample.

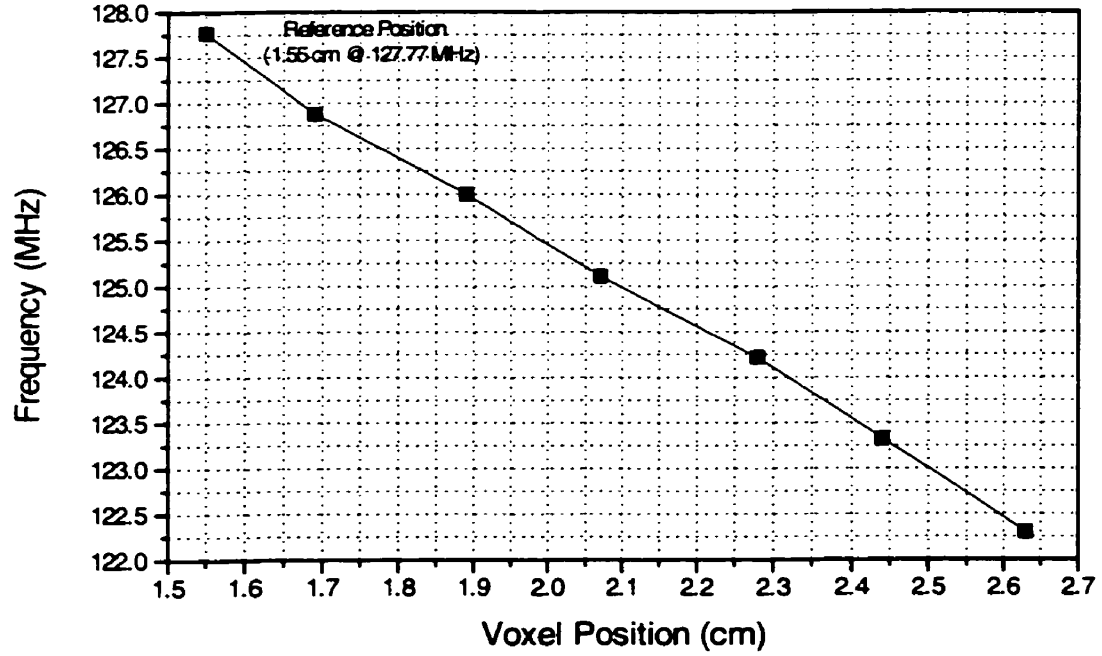

Figure 3.14. Corresponding depth calibration curve for the three-ring surface coil.

The region of optimum B_1 homogeneity can now be varied to accommodate variability in the depth of the thyroid gland and thyroid nodules.

3.4 Conclusions

MR spectroscopy using the multi-ring surface coil results in a quality of spatial localization essentially identical to that obtainable with a volume coil, but requires considerably less RF power and produces much higher SNR. When compared to standard surface coils, the multi-ring coil offers much improved water suppression and localization, with only a small loss in SNR. The B_1 response of the multi-ring coil results in less outer voxel contamination compared to the standard surface coil, but the additional power required gives a higher SAR.

The homogenous B_1 region produced by a multi-ring surface coil can be designed for any depth of interest or made depth-adjustable over a specified range of depths. Construction is relatively simple and robust, since theoretical calculations are in good agreement with practice. Used as both transmitter and receiver, the need for adiabatic RF pulses and electronic coil decoupling methods is eliminated. Thus, uniform flip angles are produced with the added advantage of homogenous reception.

Because of the localized region of high B_1 field homogeneity, the multi-ring design could be regarded as a "local volume coil", ideal for smaller VOI's at limited depths relative to the diameter of a larger sample volume, such as the case with the thyroid gland. This concept is particularly appropriate for MRS studies of defined VOI's, and also for experiments with high RF power requirements. The RF field, stronger than that of a volume coil, means that shorter pulses are possible, leading to better off-resonance

performance and shorter minimum echo times. The properties of these coils may also be particularly beneficial as B_0 field strengths are pushed higher, and bore sizes are increased, and it becomes more difficult to design and use large or whole body volume coils, where the generation and subsequent deposition of large amounts of RF power presents a double liability. Due to its simple design, small size and consequently reduced susceptibilty to RF penetration and standing wave effects on B_1 homogeneity, the multi-ring surface coil may possibly out-perform standard volume coils at high fields.

The combined advantages of high SNR and homogenous localization of the multi-ring coil is an especially attractive feature for quantitative MR spectroscopy of heterogeneous tissues, and therefore may be useful for *in vivo* tumor classification studies.

3.5 References

1. J. J. H. Ackerman, T. H. Grove, G. G. Wong, D. G. Gadian, G. K. Radda, Mapping of metabolites in whole animals by ^{31}P NMR using surface coils. *Nature* **283**, 167-170 (1980).
2. P. A. Bottomley, Selective volume method for performing localized NMR spectroscopy. U.S. Patent 4 480 228 (1984).
3. J. Frahm, K.-D. Merboldt, W. Hänicke, Localized proton spectroscopy using stimulated echoes. *J. Magn. Reson.* **72**, 502-508 (1987).
4. P. C. M. van Zijl, C. T. W. Moonen, J. R. Alger, J. S. Cohen, S. A. Chesnick, High field localized proton spectroscopy in small volumes: greatly improved localization and shimming using shielded strong gradients. *Magn. Reson. Med.* **10**, 256-265 (1989).
5. T. J. Lawry, G. S. Karczmar, M. W. Weiner, G. B. Matson, Computer simulation of MRS localization techniques: an analysis of ISIS. *Magn. Reson. Med.* **9**, 299-314 (1989).
6. S. Crozier, J. Field, I. M. Brereton, L. N. Moxon, G. F. Shannon, D. M. Doddrell, *In vivo* localized ^{1}H NMR spectroscopy at 11.7 Tesla. *J. Magn. Reson.* **94**, 123-132 (1991).
7. C. T. W. Moonen, P. C. M. van Zijl, Highly effective water suppression for *in vivo* proton NMR spectroscopy (DRYSTEAM). *J. Magn. Reson.* **88**, 28-41 (1990).
8. L. Axel, Surface coil proton NMR imaging, in "Proc., SMRM, 2nd Annual Meeting, 1983," p.16.
9. M. G. Crowley, J. L. Evelhoch, J. J. H. Ackerman, The surface-coil NMR receiver in the presence of homogeneous B_1 excitation. *J. Magn. Reson.* **64**, 20-31 (1985).
10. P. A. Bottomley, E. R. Andrew, RF magnetic field penetration, phase shift and power dissipation in biological tissue: implications for NMR imaging. *Phys. Med. Biol.* **23**, 630-643 (1978).

11. G. H. Glover, C. E. Hayes, N. J. Pelc, W. A. Edelstein, O. M. Mueller, H. R. Hart, C. J. Hardy, M. O'Donnell, W. D. Barber, Comparison of iinear and circular polarization for magnetic resonance imaging. *J. Magn. Reson.* **64**, 255-270 (1985).

12. P. Röschmann, Radiofrequency penetration and absorption in the human body: Limitations to high-field whole-body nuclear magnetic resonance imaging. *Med. Phys.* **14**, 922-931 (1987).

13. M. R. Bendall, Portable NMR sample localization method using inhomogeneous RF irradiation coils. *Chem. Phys. Lett.* **99**, 310-315 (1983).

14. A. Haase, A new method for the decoupling of multiple-coil NMR probes. *J. Magn. Reson.* **61**, 130-136 (1985).

15. W. A. Edelstein, C. J. Hardy, O. M. Mueller, Electronic decoupling of surface-coil receivers for NMR imaging and spectroscopy. *J. Magn. Reson.* **67**, 156-161 (1986).

16. P. Styles, M. B. Smith, R. W. Briggs, G. K. Radda, A concentric surface-coil probe for the production of homogeneous B_1 fields. *J. Magn. Reson.* **62**, 397-405 (1985).

17. C-N Chen, D. I. Hoult, "Biomedical Magnetic Resonance Technology," p. 157, Adam Hilger, Bristol, 1989.

18. R. A. de Graaf, K. Nicolay, M. Garwood, Single-shot, B_1-insensitive slice selection with a gradient-modulated adiabatic pulse, BISS-8. Magn. Reson. Med. **35**, 652-657 (1996).

19. R. A. de Graaf, Y. Luo, M. Garwood, K. Nicolay, B_1-insensitive, single-shot localization and water suppression. *J. Magn. Reson. B* **113**, 35-45 (1996).

20. S. B. King, L. N. Ryner, B. Tomanek, I. C. P. Smith, Multi-ring surface coils: a means for enhanced MR spectroscopy *in vivo*, in "Proc., ISMRM, 6th Annual Meeting, 1998," p.2031.

21. B. Tomanek, L. Ryner, D. I. Hoult, P. Kozlowski, J. K. Saunders, Dual surface coil with high-B_1 homogeneity for deep organ MR imaging. *Mag. Reson. Imag.* **15**, 1199-1204 (1997).

22. D. I. Hoult, R. E. Richards, The signal-to-noise ratio of the nuclear magnetic resonance experiment, *J. Magn. Reson.* **24**, 71-85 (1976).

23. J. W. Carlson, Radiofrequency field propagation in conductive NMR samples. *J. Magn. Reson.* **78**, 563-573 (1988).

24. J. R. Keltner, J. W. Carlson, M. S. Roos, T. S. Wong, T. L. Wong, T. F. Budinger, Electromagnetic fields of surface coil *in vivo* NMR at high frequencies. Magn. Reson. Med. **22**, 467-480 (1991).

25. P. S. Tofts, Standing waves in uniform phantoms. *J. Magn. Reson. B* **104**, 143-147 (1994).

26. D. I. Hoult, P. C. Lauterbur, The sensitivity of the zeugmatographic experiment involving human samples. *J. Magn. Reson.* **34**, 425-433 (1979).

27. J. R. Reitz, F. J. Milford, R. W. Christy, in "Foundations of Electromagnetic Theory," 3rd Ed., Addison-Wesley, Massachusetts, p. 242, 1979.

28. D. I. Hoult, R. Deslauriers, A high-sensitivity, high-B_1 homogeneity probe for quantitation of metabolites. Magn. Reson. Med. **16**, 411-417 (1990).

29. L. J. Giacolleto, in "Electronic Designer's Handbook," 2nd ed,. McGraw-Hill, New York, 1977.

30. W. A. Edelstein, T. H. Foster, J. F. Schenck, The relative sensitivity of surface coils to deep lying tissue, in "Proc., SMRM, 4th Annual Meeting, 1985," p.964.

31. C. E. Hayes, L. Axel, Noise performance of surface coils for magnetic resonance imaging at 1.5 T. *Medical Physics* **12**, 604-607 (1985).

32. J. S. Hyde, W. Froncisz, A. Jesmanowicz, J. B. Kneeland, Planar-pair local coils for high-resolution magnetic resonance imaging, particularly of the temporomandibular joint. *Medical Physics* **13**, 1-7 (1986).

33. T. J. Lawry, M. W. Weiner, G. B. Matson, Computer modeling of surface coil sensitivity. Magn. Reson. Med. **16**, 294-302 (1990).

34. J. Wang, A. Reykowski, J. Dickas, Calculation of the signal-to-noise ratio for simple surface coils and arrays of coils. *IEEE Trans. Biomed. Eng.* **42**, 908-917 (1995).

35. C-N Chen, D. I. Hoult, "Biomedical Magnetic Resonance Technology," p. 161, Adam Hilger, Bristol, 1989.

36. P. A. Bottomley, R. W. Redington, W. A. Edelstein, J. F. Schenck, Estimating radiofrequency power deposition in body NMR imaging. Magn. Reson. Med. **2**, 336-349 (1985).

37. P. A. Bottomley, C. J. Hardy, P. B. Roemer, O. M. Mueller, Proton-decoupled, Overhauser-enhanced, spatially localized carbon-13 spectroscopy in humans. Magn. Reson. Med. **12**, 348-363 (1989).

38. E. K. Insko, L. Bolinger, Mapping of the radiofrequency field. *J. Magn. Reson. A* **103**, 82-85 (1993).

39. P. B. Kingsley, Product operators, coherence pathways, and phase cycling. Part III: phase cycling. *Concepts Magn. Reson.* **7**, 167-192 (1995).

40. A. Haase, J. Frahm, W. Hanicke, D. Matthaei, ^{1}H NMR chemical shift selective (CHESS) imaging. *Phys. Med. Biol.* **30**, 341-344 (1985).

Chapter 4

B_0 INHOMOGENEITY CORRECTION

4.1 Introduction

The homogeneity of the B_0 field is extremely important in MR spectroscopy, affecting both spectral resolution and SNR. That is, molecular motion within an inhomogeneous B_0 field causes spectral line broadening which in turn decreases the resolution and the effective SNR of the spectrum. B_0 inhomogeneity arises from two sources: the inherent field distribution of the magnet, which depends on the design of the magnet as well as the ferromagnetic environment in which it is installed (1), and magnetic field susceptibility variations within the sample or subject (2-8).

To correct for the inherent B_0 inhomogeneity, a plot of the B_0 field is made within the magnet and a full spherical harmonic analysis is mathematically generated (9). Unwanted harmonics can then be removed (shimmed out) with superconducting shim coils (cryoshims), as well as appropriate placement of steel pieces (1), called passive shimming, that produce opposing B_0 fields of the same harmonics. These techniques can be used to meet typical magnet manufacturer's field homogeneity specifications of about 10 ppm (measured as peak to peak field variation) over a specified diameter sphere.

To further improve the homogeneity as well as correct for sample induced B_0 inhomogeneity, room temperature shim coils of up to 5^{th} order spherical harmonics are available on some large scanners (10).

For imaging studies, shimming using the room temperature shim coils is done globally to achieve the best possible homogeneity over the whole image FOV. One method of global shimming is an automatic iterative adjustment of each shim coil current until the energy of the FID signal is maximized (11). In addition to the extensive time required, this method shims on an FID that includes signals from parts of the sample that are not of interest (non-localized) since they cannot be separated from the desired signals, and also suffers from a lack of orthogonality between shim fields (12,13). A better method is to calculate the B_0 field experimentally from either frequency or phase space and then determine what shim corrections are needed to make the field homogeneous. Automatic global shimming using either spectroscopic image (14,15) or image phase difference (10,16-20) based field mapping procedures can be very time consuming since it requires a large data set covering the entire FOV as well as matrix inversion during fitting procedures.

For single voxel spectroscopy studies, the shimming has to be done quickly enough to allow time for other set-up procedures and it also needs to produce a field with homogeneity on the order of 0.1 ppm or better (21). For voxel locations remote from the origin of the shim coil set (isocenter), it is impossible to shim manually by adjusting the higher order shims due to a lack of orthogonality of the higher order shim coil spherical harmonics (12). Therefore, manual shimming is done using only the linear (X,Y,Z) shims. The automatic iterative adjustment method (11) is very time consuming when shimming to higher orders and can also fall into local minima rather than the global minimum. For these manual or automatic iterative methods, single shot localization sequences such as PRESS (22) and STEAM (23) are preferred because the same

spectroscopy gradient sequence can be employed during shimming, and therefore eddy current behavior is identical. Sequences like ISIS (24) require several accumulations to select a VOI and therefore cannot be used for iterative shimming. A single-shot shimming sequence has been reported that uses selective RF noise pulses and an identical gradient sequence to ISIS, thus exhibiting identical eddy current behavior (25). This iterative method has inferior localization quality to ISIS but does offer a suitable shimming sequence.

Automatic global shimming requires data to be acquired from the entire sample sensitive to the RF coil and therefore is slow and has poor resolution, providing an initial starting point at best. Global shimming methods can be used to select or zoom-in on a specific region of interest by using a reduced number of data points from the field map. The problems with this are that the lengthy data accumulation does not change and the reduced number of data points used to fit the field is rather small, leading to inaccurate results and sub-optimal performance.

There are a few automatic shimming methods that are suitable for localized spectroscopy studies. One method (13) is a modified chemical shift technique where 31 localized VOSY (26) spectra are taken that spatially conform to a cylinder. A field map is then generated from the distribution of the water resonance frequencies. This technique solves one problem by reducing the amount of time needed to acquire a shim data set, but depending on the available SNR, additional time may be required for averaging. An additional problem occurs if there are vacant spaces within the sample (13), such as the case of the trachea for shimming on the thyroid gland. A variation on this technique (27) obtains initial linear shims from a homogeneous phantom followed by further manual

adjustment of the linear shims with the sample placed in the magnet, essentially still a manual shimming method.

The automatic shimming method best suited to *in vivo* MRS studies is the localized shimming technique, FASTMAP (21,28), or "Fast, Automatic Shimming Technique by Mapping Along Projections". This is a phase difference technique requiring a few linear projections through the center of the localized VOI rather than taking multiple images. By mapping the field along 6 projections, the field can be characterized in terms of spherical harmonic functions. All first and second order shims can then be calculated to correct for any field inhomogeneity. This method uses a STEAM sequence that can be optimized to be very insensitive to eddy currents, thus making application to thyroid spectroscopy easy and robust. As only a few projections rather than complete images are needed, there is a substantial time saving in both data collection and fitting routines.

In this chapter, the FASTMAP autoshimming method (previously described by Gruetter et al. (21,28)) will be described and implementation showing results of phantom and *in vivo* MRS studies of the thyroid and brain.

4.2 Theory

As mentioned in Ch. 1, shim coils are designed to produce a magnetic field distribution in space corresponding to a particular spherical harmonic centered at the magnet origin (isocenter) (9). Therefore, from a spherical harmonic analysis of the B_0 field inhomogeneities and a previous calibration of the shim-coil currents, the required shims can be determined to correct for the inhomogeneity. However, for volumes not located at isocenter, the spherical harmonic fields are not orthogonal and so changes in

the higher-order shims will produce lower-order terms dependent on the magnitude of the shim change and the position $r_0 = (x_0, y_0, z_0)$ of the volume (12).

4.2.1 Magnetic Field Analysis Along Projections

Any static magnetic field B can be written as a superposition of spherical harmonics (9,28) as

$$B(r,\theta,\phi) = \sum_n [T_n + \sum_m (T^s_{nm} + T^c_{nm})] \qquad [4.1]$$

where

$$\begin{aligned} T_n &= C_n r^n P_n(\cos\theta) = k_n r^n W_n(\theta) \\ T^s_{nm} &= B_{nm} r^n P_{nm}(\sin\theta)\sin m\phi = k^s_{nm} r^n W^s_{nm}(\phi,\theta) \\ T^c_{nm} &= A_{nm} r^n P_{nm}(\sin\theta)\cos m\phi = k^c_{nm} r^n W^c_{nm}(\phi,\theta)\,. \end{aligned} \qquad [4.2]$$

Here, integers n and m are the order and degree, respectively, of the harmonic satisfying the condition $n \geq m \geq 0$; C_n, B_{nm}, A_{nm} are constants; and P_n and P_{nm} are the Legendre and associated Legendre functions, respectively. The k_n, k^s_{nm}, k^c_{nm} are convenient forms of the constant terms associated with the zero-degree, $\sin(m\varphi)$, and $\cos(m\varphi)$ terms; the angular dependent terms are lumped together as W_n, W^s_{nm}, W^c_{nm} completely separate from the radial dependence (r^n) of the spherical harmonics. The constant field term, usually written as Z^0 ($n = m = 0$), has been left out since this term can be set to zero with trivial adjustment of the spectrometer frequency.

For simplicity, the explicit separation of the $\sin(m\varphi)$ and the $\cos(m\varphi)$ terms is replaced with a common variable $i = 1 \cdots M$, where M is the number of spherical harmonics associated with r^n, and may vary for different n. The field can now be written as

$$B(r,\theta,\phi) = \sum_n \{ r^n \sum_i [k_{ni} W_{ni}(\phi,\theta)] \} . \qquad [4.3]$$

A list of these functions up to 2nd, for the shims available on the Bruker MSLX 3T system, is shown in Table 4.1.

Table 4.1 First and second order shims and their associated spherical harmonic functions in spherical and Cartesian coordinates

n	m	Shim name	k_{ni}	Spatial dependence $r^n W_{ni}(\theta,\phi)$	
				Spherical	Cartesian
1	1	X	k_{11}	$r\sin\theta\cos\phi$	x
1	1	Y	k_{12}	$r\sin\theta\sin\phi$	y
1	0	Z	k_{13}	$r\cos\theta$	z
2	0	Z^2	k_{21}	$r^2(3\cos^2\theta - 1)/2$	$z^2 - (x^2+y^2)/2$
2	1	XZ	k_{22}	$r^2\sin\theta\cos\theta\cos\phi$	xz
2	1	YZ	k_{23}	$r^2\sin\theta\cos\theta\sin\phi$	yz
2	2	X^2-Y^2	k_{24}	$r^2\sin^2\theta\cos2\phi$	x^2-y^2
2	2	2XY	k_{25}	$r^2\sin^2\theta\sin2\phi$	2xy

Along a straight line running through the center of the coordinate system, the angles θ and ϕ do not vary and consequently, all W_{ni} are constant. Therefore, the magnetic field along a projection, j, with orientation $[\phi^{(j)}, \theta^{(j)}]$ that runs through the origin, can be written as a polynomial in r with coefficients $p_n^{(j)}$:

$$B(r,\theta^{(j)},\phi^{(j)}) = \sum_n r^n p_n^{(j)} = \sum_n \{ r^n \sum_i [k_{ni} W_{ni}^{(j)}] \} . \qquad [4.4]$$

Experimental determination of the magnetic field along the projection, j, and subsequent polynomial regression analysis, yields experimental coefficients $a_n^{(j)}$, such that

$$B_{expt}(r,\theta^{(j)},\phi^{(j)}) = \sum_n r^n a_n^{(j)} . \qquad [4.5]$$

Assuming that the experimental error associated with $a_n^{(j)}$ is of Gaussian distribution, the k_{ni} are determined from standard least-square methods. It can be shown that the solution for each order, n, is a set of M equations

$$\sum_j \{ \sum_i [W_{ni}^{(j)} k_{ni}] - a_n^{(j)} \} W_{nl}^{(j)} = 0 , \qquad [4.6]$$

where l runs from 1 to M, and M represents the number of nth-order spherical harmonics ($M = 3$ for $n = 1$, and $M = 5$ for $n = 2$, see Table 4.1). Thus, in matrix form:

$$\begin{bmatrix} \sum_j W_{n1}^{(j)2} & \cdots & \sum_j W_{n1}^{(j)} W_{nM}^{(j)} \\ \cdots & \cdots & \cdots \\ \sum_j W_{nM}^{(j)} W_{n1}^{(j)} & \cdots & \sum_j W_{nM}^{(j)2} \end{bmatrix} \begin{bmatrix} k_{n1} \\ \cdots \\ k_{nM} \end{bmatrix} = \begin{bmatrix} \sum_j a_n^{(j)} W_{n1}^{(j)} \\ \cdots \\ \sum_j a_n^{(j)} W_{nM}^{(j)} \end{bmatrix} . \qquad [4.7]$$

A simple solution for k_{ni} can be obtained if projections, j, are chosen that satisfy the criteria

$$\sum_j W_{na}^{(j)} W_{nb}^{(j)} \begin{cases} = 0 & \text{for } a \neq b \\ > 0 & \text{for } a = b \end{cases} . \qquad [4.8]$$

In this case, the quadratic matrix is diagonal, and the solution for k_{ni} is given by

$$k_{ni} = \frac{\sum_j a_n^{(j)} W_{ni}^{(j)}}{\sum_j W_{ni}^{(j)2}} , \qquad [4.9]$$

that does not require matrix inversion. Equation [4.8] implies that the orientations of the projections are chosen such that the matrix $\mathbf{W}_n$ (with elements $(W_n)_{ij}$ given by $W_{ni}^{(j)}$ in Eq. [4.4] for the particular projection chosen) has orthogonal columns (28). An example is shown in Table 4.2, where the elements of a matrix $\mathbf{W}_n$ are given for a set of shim coils and projections needed for first or second order field characterization.

Table 4.2 Relative contribution $W_n^{(j)}$ of shim i with an r^n dependence along projection j

Projection Orientation			Shims							
			$n=$	1				2		
			$i=$ 1	2	3	1	2	3	4	5
j	$\theta^{(j)}$ (°)	$\phi^{(j)}$ (°)	X	Y	Z	Z^2	ZX	ZY	X^2-Y^2	2XY
1(x)	90	0	1	0	0	-1/2	0	0	1	0
2(y)	90	90	0	1	0	-1/2	0	0	-1	0
3(z)	0	---	0	0	1	1	0	0	0	0
1(xy)	90	45	1/√2	1/√2	0	-1/2	0	0	0	1
2(yx)	90	135	-1/√2	1/√2	0	-1/2	0	0	0	-1
3(xz)	45	0	1/√2	0	1/√2	1/4	1/2	0	1/2	0
4(zx)	135	0	1/√2	0	-1/√2	1/4	-1/2	0	1/2	0
5(yz)	45	90	0	1/√2	1/√2	1/4	0	1/2	-1/2	0
6(zy)	135	90	0	1/√2	-1/√2	1/4	0	-1/2	-1/2	0

Notice that if only x-, y- and z-projections are taken, then not all of the 2nd order shims can be determined, but if the six-projections labeled xy, yx, xz, zx, yz and zy are taken then all 1st and 2nd order shims can be determined.

It can easily be shown that with these choices of projections, the columns of the two matrices $\mathbf{W}_1$ and $\mathbf{W}_2$ are orthogonal and therefore satisfy the conditions in Eq. [4.8]. The coefficients k_{ni} of the expansion can then be calculated according to Eq. [4.9] from the $W_{ni}^{(j)}$ given above and the experimentally determined $a_n^{(j)}$. This is shown in Table 4.3, for the six-projections listed above. Therefore, the static magnetic field $B(r,\theta,\phi)$ and consequently any field inhomogeneity is completely characterized up to 2nd order.

Table 4.3 Calculated coefficients k_{ni} for the first- and second-order shim coils

Shim name	Associated function, $r^n W_{ni}(\theta,\phi)$	*Coefficients, k_{ni}
X	$r\sin\theta\cos\phi$	$k_{11} = (a_1^{xy} - a_1^{yx} + a_1^{xz} + a_1^{zx})/\sqrt{8}$
Y	$r\sin\theta\sin\phi$	$k_{12} = (+a_1^{xy} + a_1^{yx} + a_1^{yz} + a_1^{zy})/\sqrt{8}$
Z	$r\cos\theta$	$k_{13} = (a_1^{xz} - a_1^{zx} + a_1^{yz} - a_1^{zy})/\sqrt{8}$
Z^2	$r^2(3\cos^2\theta - 1)/2$	$k_{21} = (-2a_2^{xy} - 2a_2^{yx} + a_2^{xz} + a_2^{zx} + a_2^{yz} + a_2^{zy})/3$
ZX	$r^2\sin\theta\cos\theta\cos\phi$	$k_{22} = a_2^{xz} - a_2^{zx}$
ZY	$r^2\sin\theta\cos\theta\sin\phi$	$k_{23} = a_2^{yz} - a_2^{zy}$
X^2-Y^2	$r^2\sin^2\theta\cos2\phi$	$k_{24} = (a_2^{xz} + a_2^{zx} - a_2^{yz} - a_2^{zy})/2$
2XY	$r^2\sin^2\theta\sin2\phi$	$k_{25} = (a_2^{xy} - a_2^{yx})/2$

* For the projections (j) with orientations described in Table 4.2

4.2.2 The Off-Isocenter VOI Effect

The theoretical analysis described above assumes that the center of the coordinate system was at isocenter, and therefore can only be used for projections taken through isocenter. For VOI's translated from isocenter to a position given by (x_0, y_0, z_0), a change of coordinate system is needed given by

$$x' = x - x_0, \quad y' = y - y_0, \quad z' = z - z_0. \qquad [4.10]$$

For the linear shims (n = 1), the only effect is to cause constant frequency shifts given by $-x_0k_{11}$, $-y_0k_{12}$, and $-z_0k_{13}$, which can be corrected simply by adjusting the spectrometer frequency. However, any change in the quadratic shims (n = 2), will introduce linear terms as well as a frequency shift. This is shown below for the Cartesian shims of Table 4.1, where frequency shifts are underlined once and linear term shifts are underlined twice.

$$
\begin{aligned}
z^2-(x^2+y^2)/2 &= z'^2-(x'^2+y'^2)/2 \;\underline{\underline{-x_0x'-y_0y'+2z_0z'}}\;\underline{+z_0^2-(x_0^2+y_0^2)/2}\,,\\
xz &= x'z' \;\underline{\underline{+z_0x'+x_0z'}}\;\underline{+x_0z_0}\,,\\
yz &= y'z' \;\underline{\underline{+z_0y'+y_0z'}}\;\underline{+y_0z_0}\,,\\
x^2-y^2 &= x'^2-y'^2 \;\underline{\underline{+2x_0x'-2y_0y'}}\;\underline{+x_0^2-y_0^2}\,,\\
2xy &= 2x'y' \;\underline{\underline{+2y_0x'+2x_0y'}}\;\underline{+2x_0y_0}\,.
\end{aligned}
\qquad [4.11]
$$

Although the frequency shifts are again corrected with a change in the spectrometer frequency, the first order coefficients k_{1i} now have to be corrected for the first order changes. The voxel displacement-corrected coefficients are then given by

$$
\begin{aligned}
k'_{11} &= k_{11}-x_0k_{21}+z_0k_{22}+2x_0k_{24}+2y_0k_{25}\,,\\
k'_{12} &= k_{12}-y_0k_{21}+z_0k_{23}-2y_0k_{24}+2x_0k_{25}\,,\\
k'_{13} &= k_{13}+2z_0k_{21}+x_0k_{22}+y_0k_{23}\,.
\end{aligned}
\qquad [4.12]
$$

In this way, second order shims may be adjusted and the corresponding changes in the linear terms are automatically corrected. This eliminates the problem of shim coil non-orthogonality that plagues iterative FID-optimization techniques, as well as not having to acquire another set of data along the three magnet axes to correct for these linear shifts.

4.3 Methods

4.3.1 B_0 Field Determination: Data Acquisition and Processing

4.1.1.1 Data Acquisition

Data need to be obtained for both the magnitude and spatial distribution of the magnetic field. In order to collect spatial information along a projection, only one imaging gradient is required, in this case the read gradient. As explained previously, it is important to acquire the projection data required for the magnetic field calculation with the same localization sequence used for the spectroscopic data collection. Therefore, the

basic STEAM sequence described in Chapter 1 was modified to include a readout gradient (Fig. 4.1), with the refocusing lobes of the slice selection and read gradients incorporated into the TE-crushers, resulting in TE = 30.8 ms, TM = 15 ms and TR = 1000 ms. The sequence in Fig. 4.1 represents a coronal-sagittal oblique-projection with a projection angle of 135°. That is, the projection is in the x-y direction at a 45° angle, with slice selections perpendicular in the y-x and z-directions (Fig. 4.2). The first RF pulse is applied without a field gradient while the second and third pulses are slice selective and therefore select signal along a bar, with length equal to the entire FOV in the direction determined from the percentage of X, Y, or Z gradient applied.

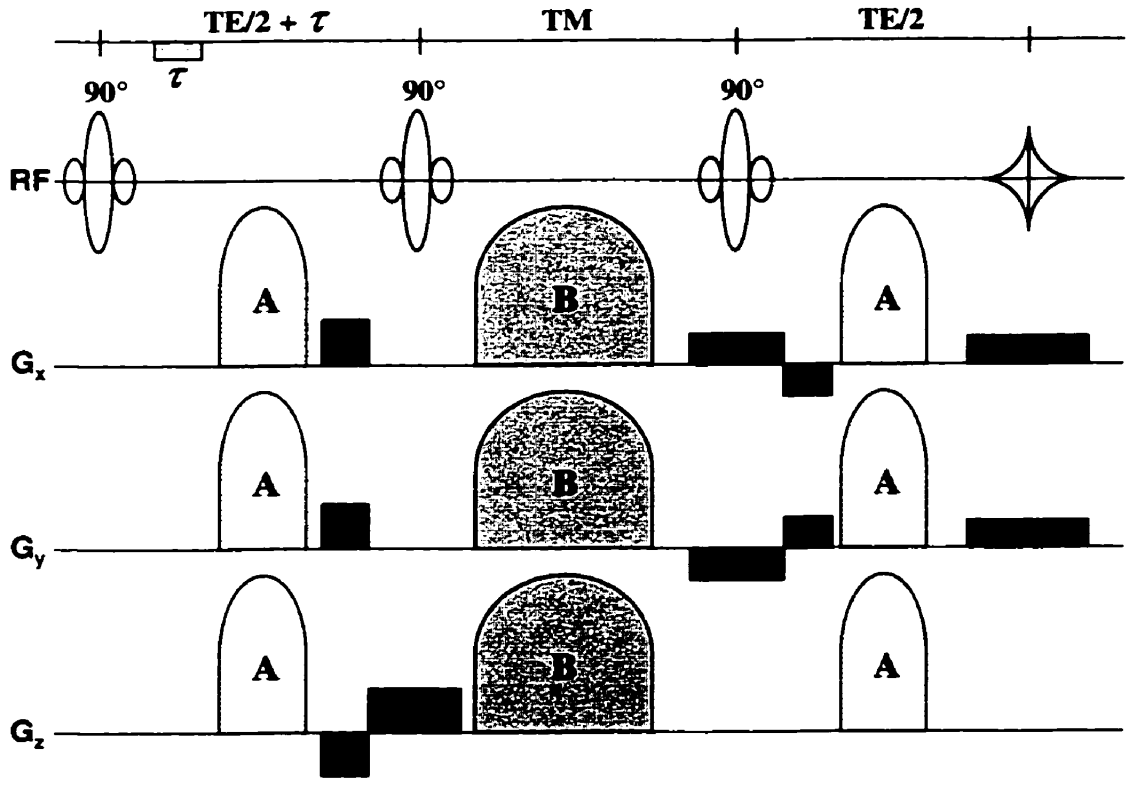

Figure 4.1 The FASTMAP pulse sequence. This is the STEAM sequence described in Chapter 1, with selection of a bar rather than a voxel, with which the phase and therefore B_0-field can be determined.

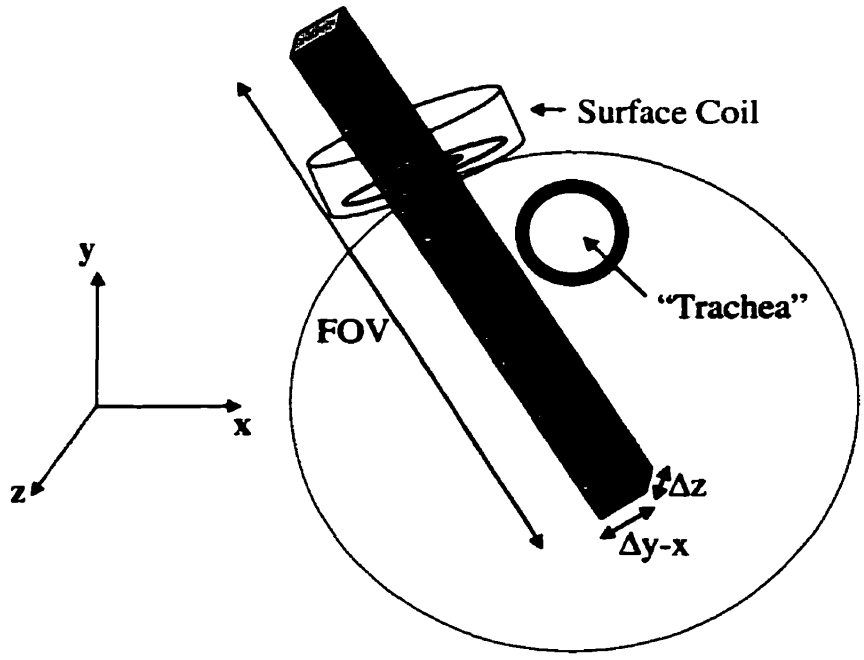

Figure 4.2 Orientation of the x-y FASTMAP projection within the "neck" using the pulse sequence of Fig. 4.1.

The slice thickness or bar width (Δy-x and Δz in Fig. 4.2) was chosen to be between 5 and 10 mm, depending on the size of the VOI. The FOV or acquired bar length for surface coil studies was 12 cm (adjusted by altering the read gradient strength) with a spectral width (SW) of 33 kHz and 256 complex points resulting in a spatial resolution of 0.047 cm/point along the projection. The frequency of the first pulse was set to that of water (referenced as 0 Hz), while the frequency during readout was set such that f = 0 corresponded to the center of the voxel. An oblique readout gradient is comprised of the superposition of two orthogonal linear gradients. For example, the xy projection FID is acquired using the coronal-sagittal-oblique slice orientation with a slice angle of 135°, so that the readout frequency f^R is calculated as

$$f^R = G_x^R x + G_y^R y, \qquad [4.13]$$

where G_x^R and G_y^R are the strengths of the read gradient ($G^R = \frac{SW(Hz)}{FOV(cm)}$) along the x- and y-axes respectively ($= \pm\frac{1}{\sqrt{2}}G^R$ for these 45° and 135°orientations); and x and y are the voxel displacements (in cm) along the x- and y-axes, respectively.

This sequence is first run as described above and an FID is collected. As explained in Chapter 1, after excitation of the sample with a 90° RF pulse, the magnetization will precess in the transverse plane with frequency ω that is proportional to the main magnetic field $B(r,\theta,\phi)$ and acquire a complex phase φ_1 before the next 90° pulse. To obtain the frequency/phase information, a second FID is collected with an extra delay (τ) between the first two 90° RF pulses, thus acquiring phase $\varphi_1 + \Delta\varphi$. The phase difference between acquisitions in the spatial domain is calculated along the projection, which relates to the precession frequency (in ppm) as

$$\Delta\nu^{(j)} = \frac{1}{2\pi\nu_0\tau}\Delta\varphi^{(j)}, \qquad [4.14]$$

where ν_0 is the Hz-to-ppm conversion factor of 127.7 MHz/ppm at 3T; τ = 5 ms is the extra phase encoding delay time. The precession frequency is directly proportional to the magnetic field at that point. Referring again to Fig. 4.1, notice that the first RF pulse is applied in the absence of gradients resulting in a phase evolution during τ that is completely independent of eddy-current effects.

For improved SNR and to allow for phase cycling, two averages of each FID were used.

4.1.1.2 Data Processing

The Bruker FID data first needed to be byte-order swapped for further analysis. The FID's were then bandpass-filtered for noise reduction, after optional zero-filling. The data were converted from the sequential acquisition ADC mode used by Bruker to simultaneous acquisition mode, prior to Fourier transformation. Fourier transformation of the FID converts the data from time domain to spatial information along the particular projection direction.

A variable bar length, L, is chosen for each projection during data processing to allow fitting to be done only within a particular volume, usually slightly larger than the size of the voxel. This variability also allows polynomial fitting through discontinuities, due to signal nulls (such as the trachea or the surface of the sample), to be avoided. It has been reported that L should be chosen such that it satisfies the condition, $L \geq 3 \times \sqrt{A}$, where A is the cross sectional area of the bar (28). Therefore, the bar length needs to be approximately three times the bar width used for the projection. Because normal thyroid glands are generally less than 1.5 cm in diameter, a 5 mm bar width should be used. Thyroid tumors can be up to 4 cm in diameter, so for improved SNR a bar width of 1 cm may be used. Gruetter (21) also determined a noise error propagation relation, where the error in the polynomial coefficients a_1 and a_2 are proportional to $L^{-3/2} * \Delta r^{1/2}$ and $L^{-5/2} * \Delta r^{1/2}$, respectively. Here, Δr is the digital resolution in cm/point, which is found by dividing the FOV by the number of points used in the projection. Therefore, the advantage of using a surface coil rather than a head coil is that smaller FOV's are used, thereby reducing Δr and hence less noise error in the projections.

Using the user-specified bar-length for each projection, the phase difference was then calculated using the reduced data set. It can be shown that the phase difference is given by

$$\Delta\varphi^{(j)} = \varphi_1^{(j)} - \varphi_2^{(j)} = \arctan\left(\frac{z_2^{(j)}}{z_1^{(j)}}\right), \qquad [4.15]$$

where $z_1^{(j)}$ and $z_2^{(j)}$ are the complex, spatially transformed projection data of the first and second (with extra delay τ) acquisitions respectively. Phase discontinuities were corrected using a phase unwrapping routine, which tested for π phase jumps and added or subtracted a multiple of π from the center position.

Using an IDL (Interactive Data Language) -based polynomial fitting routine, with a weighting factor related to the SNR of the projection data, either first- or second-order polynomials of the form

$$a_0^{(j)} + a_1^{(j)} r + a_1^{(j)} r^2 \qquad [4.16]$$

were used to model the functional dependence of $\Delta\nu^{(j)}$ in Eq. [4.14]. The constant term, $a_0^{(j)}$, was ignored since this can be corrected for by simply adjusting the spectrometer frequency.

4.3.2 Shim Control Module Calibration

Calibration of the shim control module (SCM) was done by measuring the k_{ni} at the magnet center for six SCM settings, centered about a zero SCM reference setting. For the linear shims the SCM settings were: -2000, -1000, -500, 500, 1000, 2000, while for the second order shims the settings were; -4000, -2000, -1000, 1000, 2000, 4000. Calibration measurements were made with a spherical phantom 12 cm in diameter which

consisted 5 mM $CuSO_4$ and 0.3% NaCl. Data collection consisted of 256 data points over a 15 cm FOV with τ = 10 ms, a bar width of 12 mm and a calculation bar length of 8 cm. A k_{ni} was determined from the zero SCM setting to represent the background B_0. This value was subtracted from all other calibration k_{ni}. From a plot of ΔSCM_p (in SCM units) versus measured k_q for each shim coil calibration point (in ppm/cm^n) (where p and q are abbreviations for the ni notation), the correlation coefficient ($c_p{}^q$) is determined from the slope of the best-fit line (in SCM units/ppm/cm^n). The correlation coefficients can then be grouped into a correlation matrix given by

$$\mathbf{C} = \begin{bmatrix} c_x^x & c_x^y & c_x^z & c_x^{z^2} & \cdots \\ c_y^x & c_y^y & c_y^z & c_y^{z^2} & \cdots \\ c_z^x & c_z^y & c_z^z & c_z^{z^2} & \cdots \\ c_{z^2}^x & c_{z^2}^y & c_{z^2}^z & c_{z^2}^{z^2} & \cdots \\ \vdots & \vdots & \vdots & \vdots & \end{bmatrix}, \qquad [4.17]$$

where, for example, c_x^x is the slope of the line from a plot of the measured k_x for different X-SCM settings, and $c_{z^2}^x$ is the slope of the line from a plot of the measured k_{z^2} for different X-SCM settings. As noted by Gruetter et al. (28), some of the higher order shim coils are not completely described by their theoretical field functions, but produce small linear terms. These imperfections can be seen in the cross correlation terms ($c_p{}^q$, $p \neq q$) of the correlation matrix ($\boldsymbol{C}$). For example, changing the SCM setting of the Z^2 shim by +1000, could result in an additional small x-gradient, for example, equal to a X-SCM change of +11 units. This would create a linear inhomogeneity characterized by the X shim and therefore, the X shim needs to be corrected by −11 units.

The correlation coefficient determination was done using a separate IDL routine, using polynomial regression.

4.3.3 Shim Current Determination

Before the SCM settings were calculated, the polynomial coefficients (k_{ni}) were corrected for an off isocenter voxel position (if required) according to Eq. [4.12]. The SCM settings required for correction of the B_0 field inhomogeneities were calculated as

$$\mathbf{C}' \cdot \mathbf{G} = \Delta\mathbf{SCM}\,, \qquad [4.18]$$

where $\mathbf{C}'$ is the calibration matrix, $\mathbf{G}$ is the experimentally determined field inhomogeneities or gradients characterized by the polynomial coefficient vector $\mathbf{k}$, and $\Delta\mathbf{SCM}$ is the required change in the SCM setting.

The diagonal components (c_p^p) of the calibration matrix are identical to the expected correlation coefficients of the correlation matrix ($\mathbf{C}$), but the off diagonal components ($c_p'^q$, $p \neq q$) are re-calculated to correct for the imperfect nature of the second order shim coils. Only the off-diagonal calibration coefficients that affect the linear shims are considered, all other off-diagonal calibration coefficients are zeroed. The linear off-diagonal terms of the calibration matrix are required to correct for the linear gradients induced by changing the higher order SCM settings. For example, if a second order inhomogeneity that is represented by the polynomial function of the Z^2 shim coil is present, then a k_{z^2} will be measured. This will be corrected by applying a change in the Z^2-SCM setting given by $\Delta SCM_{z^2} = c_{z^2}^{z^2} k_{z^2}$. If the Z^2 shim coil is imperfect and produces a small X-gradient as well, then this X-gradient can be calculated as a change in the overall x-coefficient given by $\Delta k_x = \dfrac{\Delta SCM_{z^2}}{c_{z^2}^{x}}$. Therefore, to reverse the effect of the

X-gradient induced by changing the Z^2-SCM, an additional change in the X-SCM setting is required and is given by

$$\Delta SCM_x = -c_x^x \Delta k_x = \left(-c_x^x \frac{c_{z^2}^{z^2}}{c_{z^2}^x} \right) k_{z^2} = c_x'^{z^2} k_{z^2}, \qquad [4.19]$$

where $c_x'^{z^2}$ is the off-diagonal calibration coefficient and the negative sign is required to reverse the effect. Therefore, the original off diagonal terms in the correlation matrix **C** are now replaced with correction calibration coefficients calculated in the same manner as the term in the brackets of the above equation. In matrix form, the SCM determination equation then becomes

$$\begin{bmatrix} c_x^x & c_x^y & c_x^z & c_x'^{z^2} & \cdots \\ c_y^x & c_y^y & c_y^z & c_y'^{z^2} & \cdots \\ c_z^x & c_z^y & c_z^z & c_z'^{z^2} & \cdots \\ 0 & 0 & 0 & c_{z^2}^{z^2} & \cdots \\ \vdots & \vdots & \vdots & \vdots & \ddots \end{bmatrix} \begin{bmatrix} k_x \\ k_y \\ k_z \\ k_{z^2} \\ \vdots \end{bmatrix} = \left[\Delta SCM_x \; \Delta SCM_y \; \Delta SCM_z \; \Delta SCM_{z^2} \cdots \right], \quad [4.20]$$

where the matrix on the left is the calibration matrix **C'**.

4.3.4 Experimental

The FASTMAP autoshimming technique was implemented on the Bruker MSLX 3T scanner. The system was equipped with the following room temperature shim coils: X, Y, Z, Z^2, XZ, YZ, X^2-Y^2, 2XY, Z^3, Z^2Y, Z^2X and Z^4, controlled via the shim control module (SCM) unit. A Bruker program was written to control data acquisition and storage. Data were transferred to the local Unix workstation for computations with an automatic transfer program written in IDL. An IDL program was written to read the

FID's (including byte swapping, zero filling, noise reduction, correction for Brukers non-sequential ADC acquisition mode, and Fourier transformation), polynomial fit the data, calculate the shim coefficients, and subsequently determine the new SCM settings (using the calibration data). This program is shown in Appendix I. The new SCM settings were then transferred back to the spectrometer.

Experiments using phantoms were performed on the cylindrical "neck phantom", shown in Fig. 4.2, placed with its long axis in the B_0 field direction and using a 15-cm FOV. For the *in vivo* brain study, a standard head coil was used with a 20-cm FOV. The *in vivo* thyroid studies were done using a multi-ring surface coil and a 12-cm FOV.

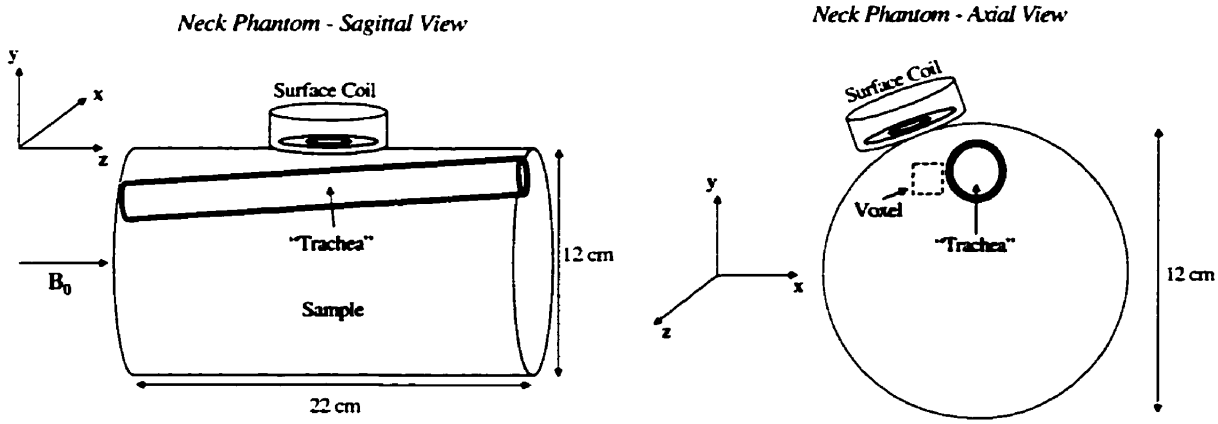

Figure 4.2 The "neck phantom", consisting of a cylindrical jug (12 cm in diameter, 22 cm in length) filled with 0.3% NaCl in distilled H_2O, with a smaller air-filled tube (2.5 cm in diameter) placed at the appropriate angle to mimic the "trachea".

4.4 Results and Discussion

4.4.1 SCM Calibration

The results of the SCM calibrations are shown in Fig.'s 4.3 - 4.7, for all linear shims, the Z^2 shim and a representative cross-correlation (measured X gradient from changing the Z^2 SCM setting). The SCM setting (in SCM units) is plotted against measured polynomial coefficient k_q (in ppm/cm^n) and the slopes of the lines are the coefficients of the previously described correlation matrix, **C** (in SCM units/ppm/cm^n).

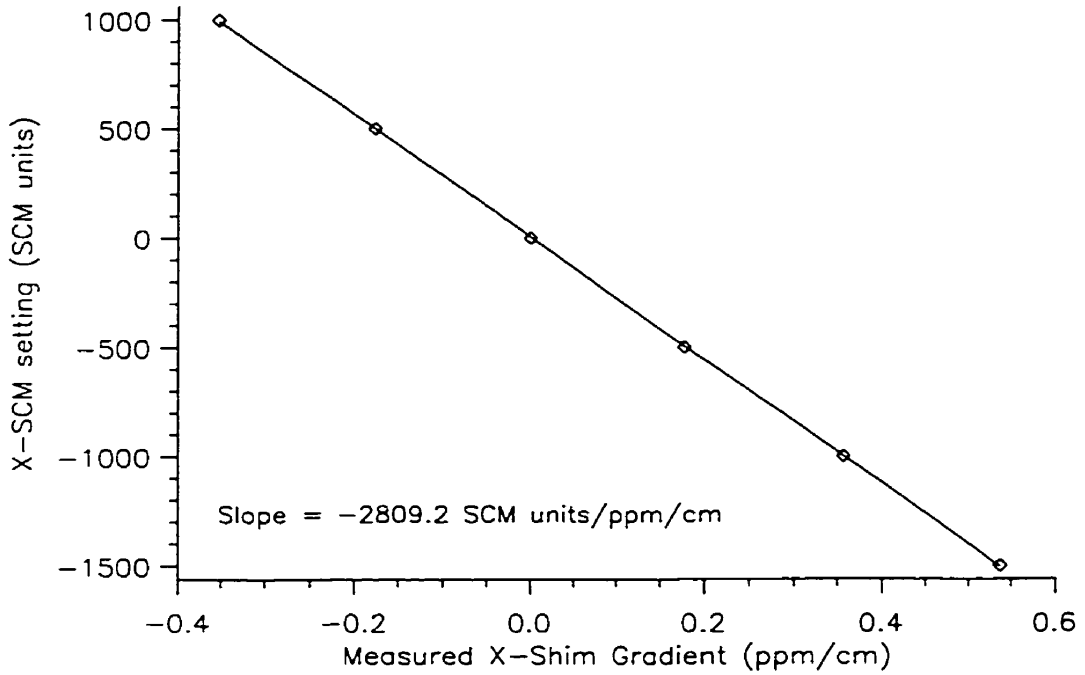

Figure 4.3 Plot of X-SCM setting vs. measured inhomogeneity described by the X-shim polynomial.

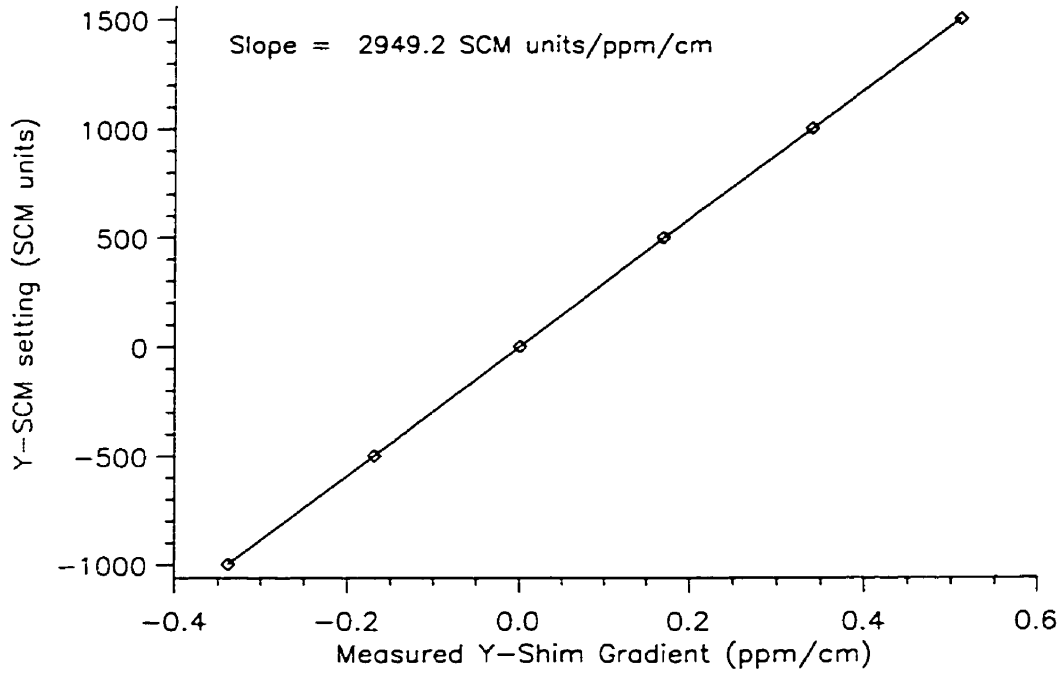

Figure 4.4 Plot of Y-SCM setting vs. measured inhomogeneity described by the Y-shim polynomial.

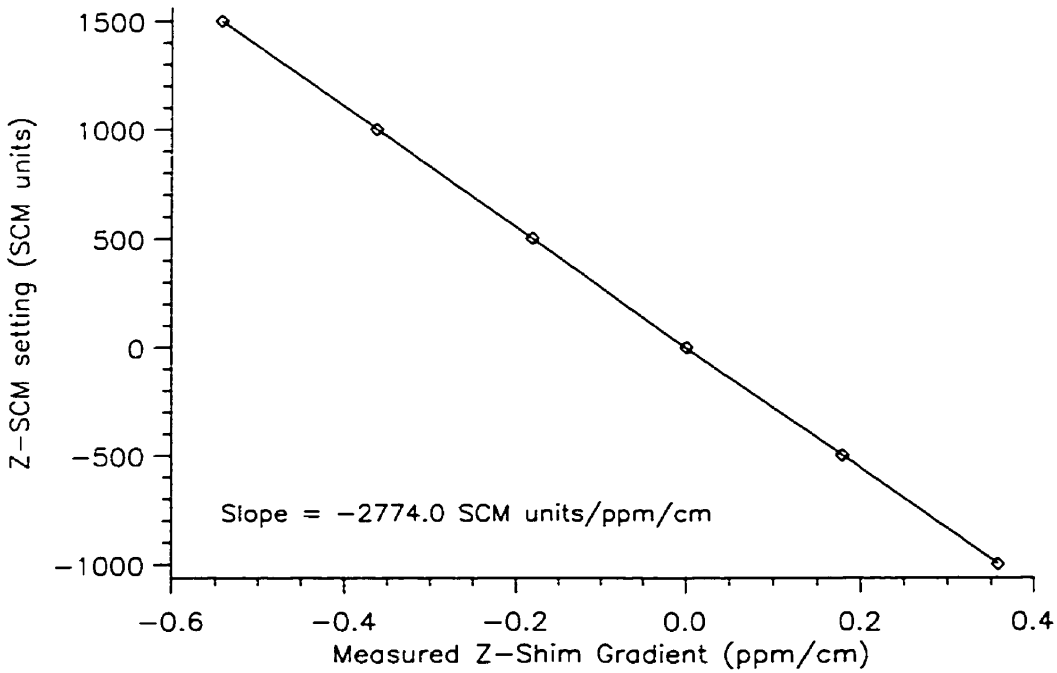

Figure 4.5 Plot of Z-SCM setting vs. measured inhomogeneity described by the Z-shim polynomial.

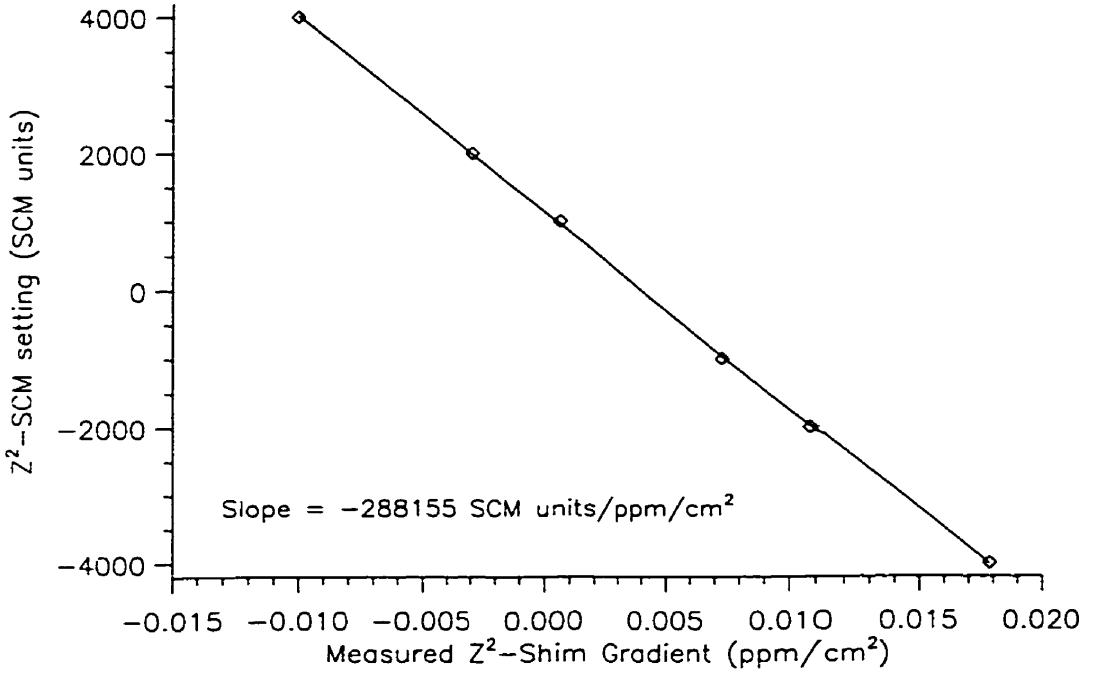

Figure 4.6 Plot of Z^2-SCM setting vs. measured inhomogeneity described by the Z^2-shim polynomial.

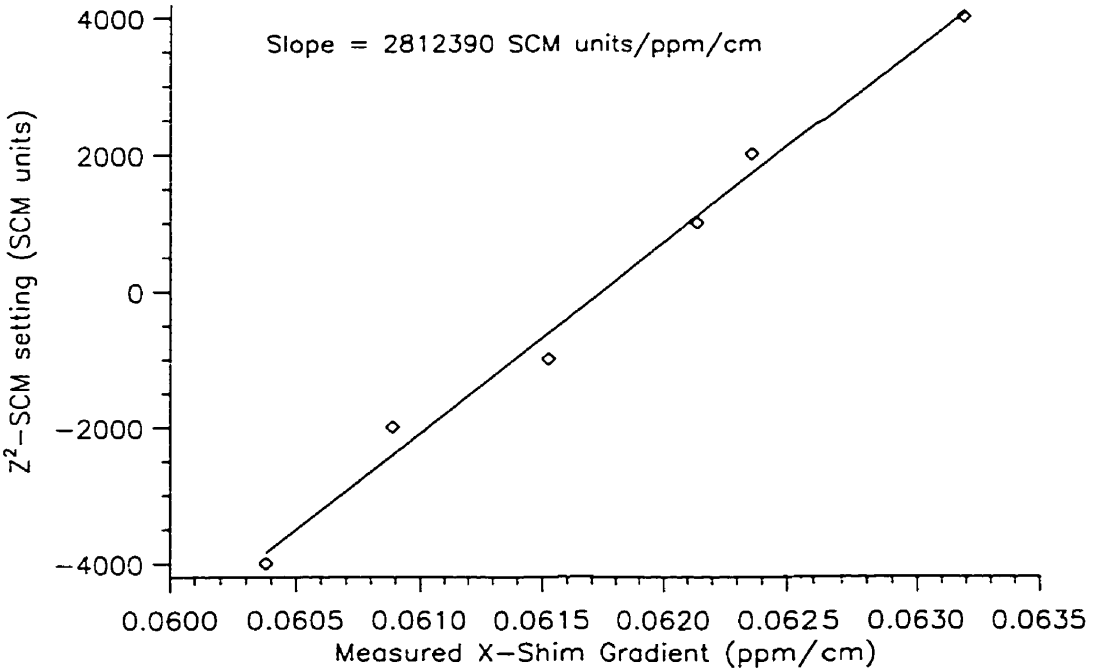

Figure 4.7 Plot of Z^2-SCM setting vs. measured inhomogeneity described by the X-shim polynomial, representing a cross correlation.

The SNR of the projection data is dependent on the linewidth of the water resonance at a particular SCM setting. For large linear SCM settings (± 1500 for linear shims), broadening of the water resonance occurs because of the rather large inhomogeneity introduced. For the linear vs. linear calibration plots, one of the 1500 SCM setting data points is missing because the SNR of the projection data was insufficient. Only one of the ±1500 SCM settings resulted in poor SNR, likely because of the linear inhomogeneity already present. That is, if an X-inhomogeneity of +300 SCM units is already present (due to the sample), and the X-SCM is set to +1500 SCM units, then a total inhomogeneity of +1800 SCM units now exists. Conversely, if the X-SCM is set to –1500, a total X-inhomogeneity of only –1200 SCM units exists.

The calibration matrix (**C'**) of Eq. [20] is calculated using Eq. [19]. For example, the X-shim calibration coefficient c_x^x is identical to the correlation coefficient, but the off-diagonal term

$$c_x'^{z^2} = -c_x^x \frac{c_{z^2}^{z^2}}{c_{z^2}^x} = -2809.2\,SCM\ units/ppm/cm \left(\frac{-288155\,SCM\ units/ppm/cm^2}{-2812390\,SCM\ units/ppm/cm^2} \right)$$
$$= 287.8\,SCM\ units/ppm/cm\ .$$

The resulting calibration matrix (in SCM units/ppm/cm^n), including all linear off-diagonal components, is given by

$$C' = \begin{bmatrix} -2809.2 & 58.8 & -159.6 & -1234.9 & -1857.2 & 192.7 & 7991.2 & 287.8 \\ -9.8 & 2949.2 & 163.7 & 892.1 & 375.8 & 1222.6 & -5400.3 & 129.3 \\ -7.3 & -18.9 & -2774.0 & -271.5 & -240.2 & 1036.2 & -1406.5 & -3205.7 \\ 0 & 0 & 0 & -288155 & 0 & 0 & 0 & 0 \\ 0 & 0 & 0 & 0 & 0 & -119523 & 0 & 0 \\ 0 & 0 & 0 & 0 & -113199 & 0 & 0 & 0 \\ 0 & 0 & 0 & 0 & 0 & 0 & -804985 & 0 \\ 0 & 0 & 0 & 0 & 0 & 0 & 0 & 369684 \end{bmatrix}.$$

From the calibration, it was found that the SCM cable connections to the XZ and YZ shim coils were reversed such that changing the XZ-SCM setting actually created a YZ polynomial field distribution. The solution to this can be seen in the calibration matrix, where the XZ and YZ shim calibrations appear to be switched. In this way, a measured inhomogeneity described by the YZ polynomial is corrected by changing the XZ-SCM setting and vice versa.

4.4.2 Phantom Studies

Because sample regions devoid of signal will present difficulties to the shimming procedure, the FASTMAP technique was tested on the "neck phantom" of Fig. 4.2, which consisted of a "trachea" and a "outer surface". With an appropriately placed voxel, this would mimic the *in vivo* thyroid situation. In addition, in the case of multi-ring surface coil spectroscopy, the characteristic B_1 response will cause signal loss far from the coil. More importantly, there will be a region near the surface of the coil which experiences zero B_1-field, and therefore creates another region devoid of signal. The signal voids are seen in an axial image of the "neck phantom" from the multi-ring surface coil.

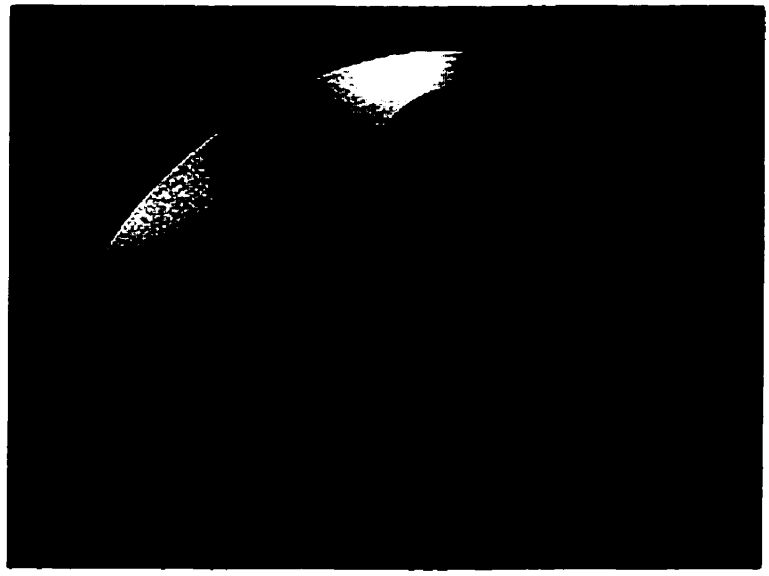

Figure 4.8 An axial image (horizontal-x, vertical-y) taken of the "neck phantom" with a multi-ring surface coil (two-ring surface coil of Ch. 3).

4.1.1.3 1st Order Shimming

The shimming results of using 1st order FASTMAP field determination are shown in Fig. 4.9 using the two-ring surface coil as shown in Fig. 4.8, for τ = 5 ms, a bar-width of 1.0 cm and a bar-length of 3.0 cm at position x = 1.45 cm, y = -0.3 cm, z = 0.0 cm. Most projections have a point where the $B_1 = 0$, a characteristic of the multi-ring coil, and therefore the signal drops to zero. There are portions of the XZ (~ -1.0 cm) and ZX (~ 1.0 cm) projections that have a more rapid fall-off, as could be expected from the B_1 response, because the projection is partially intersecting the "trachea". The calculated B_0 fields for all but the YX-projection have a sharp discontinuity due to the $B_1 = 0$ point of the coil but do not adversely affect the polynomial fit because the fit is weighted according to SNR. A larger inhomogeneity due to the presence of the "trachea" is apparent in the YX projection (1.2 cm to 1.5 cm) and the ZX projection (0.9 cm to 1.5 cm), yet there is no attempt to fit to this inhomogeneity with a 1st order fit.

As expected, the calculated shims required to correct for the inhomogeneity were nearly identical to the manual shims that were used to minimize the spectral linewidth. The SCM shim settings in the two cases are shown below, with the resultant water linewidth (with 1 Hz line broadening) from a 1.0 cm^3 voxel.

Manual Shims: X-SCM = 404, Y-SCM = -500, Z-SCM = -331 $\rightarrow$ $\Delta\nu_{H2O}$ = 3.5 Hz.

Calculated Shims: X-SCM = 443, Y-SCM = -533, Z-SCM = -334 $\rightarrow$ $\Delta\nu_{H2O}$ = 3.5 Hz.

The same spectral linewidth 3.5 Hz was achieved with both methods of 1^{st} order shimming, compared to 21 Hz without any shimming done.

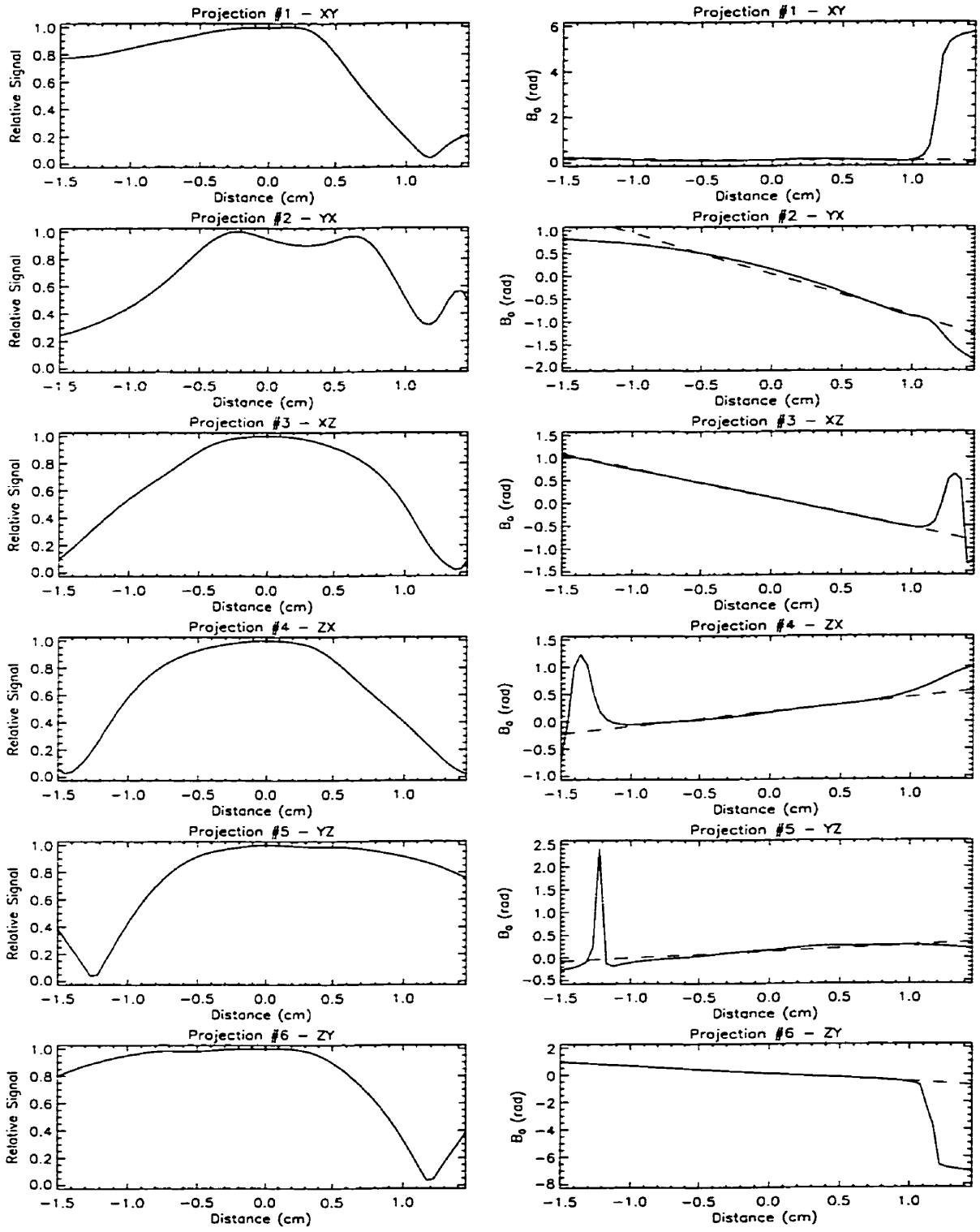

Figure 4.9 Relative spatial domain signal along the six projections (left), and (right) corresponding B_0 maps along those projections (solid) with the 1st order polynomial fit (dashed). The B_0 map is shown in radians, prior to the scaling of Eq. 4.14.

4.1.1.4 1st and 2nd Order Shimming

The shimming results using 1st and 2nd order FASTMAP field determinations are shown in Fig. 4.11, utilizing the three-ring surface coil as shown in Fig. 4.10 for τ = 30 ms and a bar-width of 0.75 cm at position x = 1.45 cm, y = -0.3 cm, z = 0.0 cm. The bar-length was chosen to be 3.0 cm except projection #6, for which a 1.5 cm bar-length was used to avoid higher order B_0 components present for larger bar-lengths.

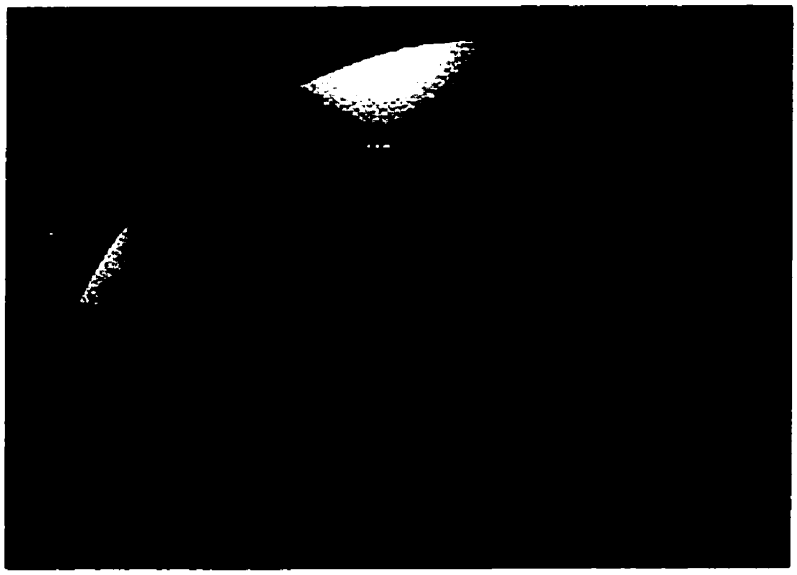

Figure 4.10 An axial image taken of the "neck phantom" with the three-ring surface coil.

The 1st and 2nd order shim calculations were again compared to a manual adjustment of the linear shims. The SCM shim settings are shown below, with the resultant water linewidth from a 1.2 × 1.2 × 1.2 cm^3 voxel.

Manual shims: X-SCM = 250, Y-SCM = -251, Z-SCM = -519,

$\Delta\nu_{H2O}$ = 2.3 Hz.

Calculated shims: X-SCM = 518, Y-SCM = -236, Z-SCM = -449,

Z^2-SCM = -2705, XZ-SCM = -2887, YZ-SCM = 175, 2XY-SCM = 4294, X^2-Y^2-SCM = 7083,

$\Delta\nu_{H2O}$ = 2.0 Hz.

The 1st and 2nd order autoshim calculations achieved a linewidth of 2.0 Hz, an improvement of 13 % compared to the manual shim linewidth of 2.3 Hz.

In performing 1st and 2nd order shim calculations, there will be additional higher order terms as well (for instance 3rd order variation). Therefore, the 1st and 2nd order fitting will try to compensate for those higher order components. It was seen that by polynomial fitting the projection data to up to 3rd order, but then using only 1st and 2nd order shim coils, different SCM settings were determined. This method did not improve the overall shim results, but rather had inferior performance.

The procedure of performing a second autoshim, with the SCM settings of the first run-through as starting values, was useful in that it did improve the linewidth in cases where the voxel was located far from isocenter but did not significantly improve the results for voxels near isocenter.

Generally, when shimming on phantoms, a manual linear shim does an excellent job. Therefore, there would not be too much improvement expected when using more sophisticated techniques such as FASTMAP. Greater improvements over manual shimming may be expected *in vivo*, where typical localized spectra at 3T have water linewidths of 23 Hz, so that a 13% improvement would lead to a reduction in linewidth of 3 Hz.

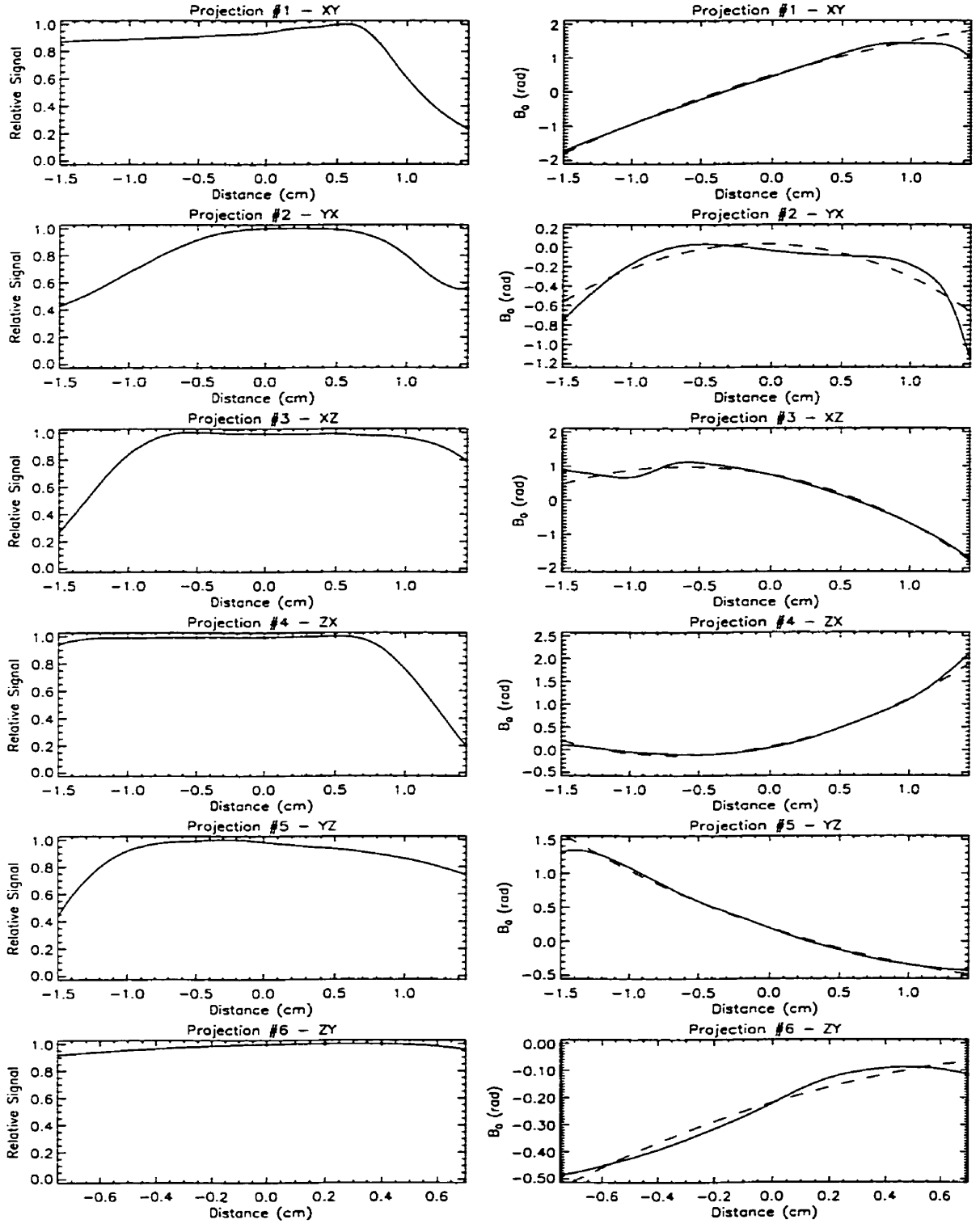

Figure 4.11 Relative spatial domain signal along the six projections (left), and (right) corresponding B_0 maps along those projections (solid) with 1st and 2nd order polynomial fitting (dashed).

4.4.3 Brain Study

The FASTMAP technique was tested *in vivo*, first on the brain to see how well it would perform in the homogeneous sample/B_1 case. The B_0 fitting results showed the expected uniform projections with no discontinuities. The water spectrum obtained with the calculated shim set plus fine tuning the linear shims is compared to results using a predetermined default brain shim set as well as the result when manual shimming was performed from the default shim set for approximately 8 minutes (Fig. 4.12). The water linewidth obtained with the default shims was 16.5 Hz, whereas with a manual shim, it was improved to 8.0 Hz. The FASTMAP autoshimming technique obtained a linewidth of 7.3 Hz, an improvement of approximately 10 %, with marginally improved line shape.

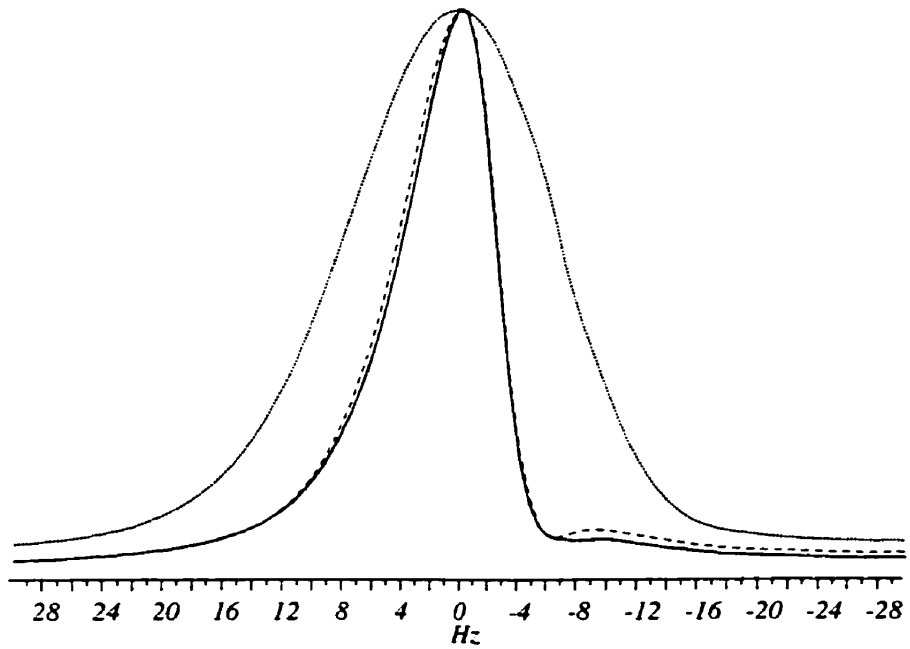

Figure 4.12 *In vivo* water spectra from the brain of a healthy volunteer with (a) a predetermined default brain shim set (dotted), (b) manual shimming from the default shim set (dashed) and (c) FASTMAP determined shim set with fine tuning of linear shims (solid). The voxel size was 2.0 cm^3.

4.4.4 Normal Thyroid Gland Studies

Finally, the FASTMAP technique was tested on the normal thyroid gland *in vivo*, using a multi-ring surface coil, to see how well it would perform in the inhomogeneous sample/B_1 case *in vivo* (Fig. 4.13). Typically, for *in vivo* MR spectroscopy on normal thyroids, the voxel is placed very close the trachea and therefore is subject to large B_0 inhomogeneities and large spectral linewidths.

Figure 4.13 Axial image of the neck through middle section of the thyroid with the three-ring surface coil of Ch. 3 placed on top of the neck, displaced slightly to the subject's right side (left as seen above).

Second order fitting resulted in calculated 2^{nd} order inhomogeneities that were too large to be corrected by the available shims. Therefore, only first order shimming was performed. The shimming results are shown in Fig. 4.14 for τ = 5 ms, a bar-width of 0.5 cm and a bar-length of 1.5 cm at position x = 1.34 cm, y = -1.05 cm, z = 0.5 cm. There are portions of the XY (~ -0.4 cm) and the ZX (~ 0.3 cm) projections that pass through the trachea and therefore a discontinuity is present in the corresponding B_0 fit.

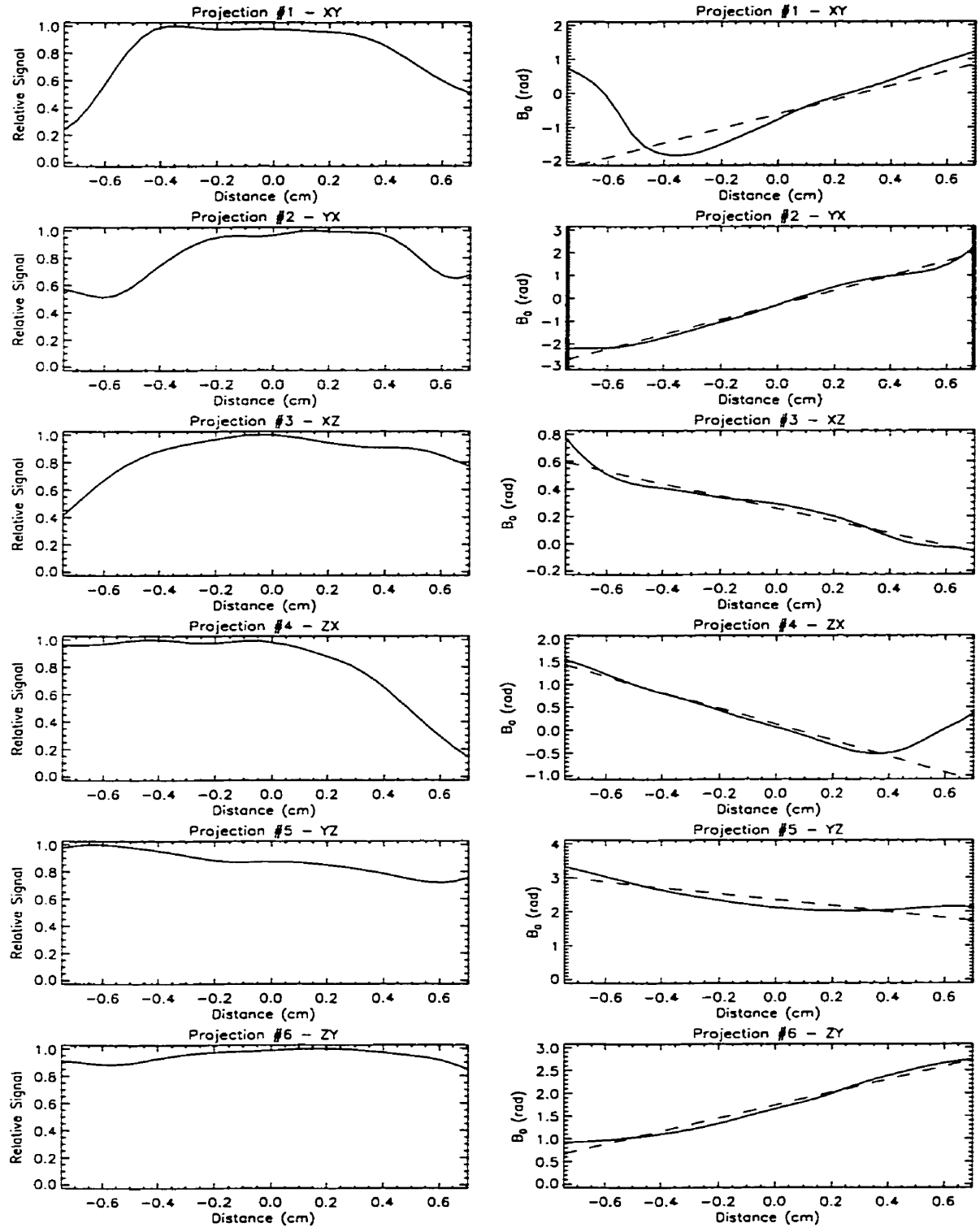

Figure 4.14 Relative spatial domain signal along the six projections (left), and (right) corresponding B_0 maps along those projections (solid) with 1st order polynomial fitting (dashed).

The SCM shim settings for the cases of manual and FASTMAP shimming are shown below, with the resultant water linewidth from the voxel described above.

Manual Shims: X-SCM = 1957, Y-SCM = 1027, Z-SCM = -1030 → $\Delta\nu_{H2O}$ = 40.7 Hz.

Calculated Shims: X-SCM = -741, Y-SCM = 1978, Z-SCM = -540 → $\Delta\nu_{H2O}$ = 25.0 Hz.

The water spectrum obtained with the calculated linear shim set is compared to results when manual linear shimming was performed (Fig. 4.15). The water linewidth obtained by manual shimming for 4 minutes was 40.7 Hz, whereas the FASTMAP autoshimming technique obtained a linewidth of 25.0 Hz, which is typical for optimum water linewidths obtained after lengthy manual shimming (8-10 minutes). This shows that the FASTMAP technique is capable of obtaining optimum shim adjustments in a fraction of the time required for manual shimming. Because the calculation method finds the absolute minimum, the problem of falling into local minima, which plagues iterative manual shimming routines, is avoided.

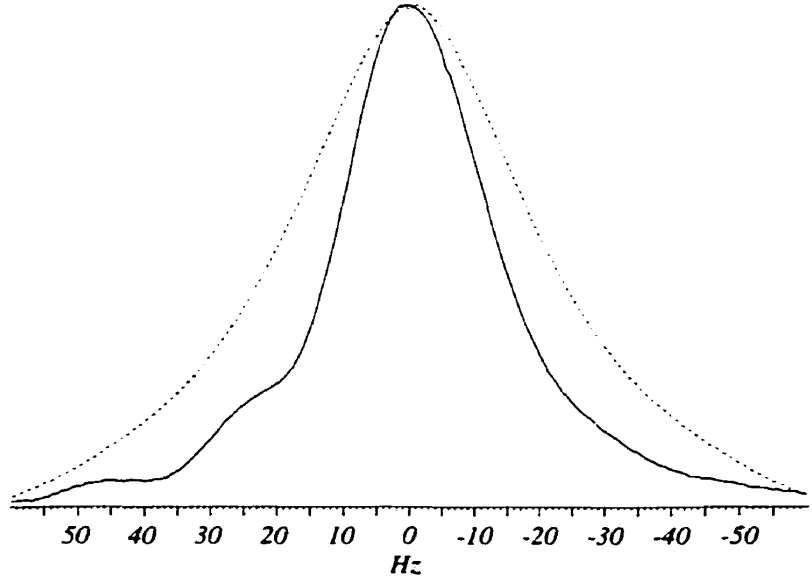

Figure 4.15 *In vivo* water spectra from the thyroid gland of a healthy volunteer with (a) manual linear shimming (dashed) and (b) FASTMAP determined linear shim set (solid).

It should be noted that large susceptibility variations in a sample could give rise to field patterns that may not be expressed as sums of lower order spherical harmonics (13). In this case, the residual inhomogeneities would not be removed using shim adjustments and therefore FASTMAP (or any other auto-shim method for that matter) would probably not be as successful.

4.5 Conclusions

This FASTMAP implementation required specific attention to be paid to the orientation of the projections and determination of the spherical harmonic coefficients (k_{ni}) from the experimental polynomial coefficients (a_{ni}) as differences existed from those used in Gruetter et al. (21), due to variations in the angular definitions of the projections. The signal voids experienced due to the trachea and the B_1-null associated with the multi-ring surface coil as well as the surface of the neck required a different fitting routine than Gruetter et al. (21), which incorporated SNR weighting and variable bar lengths.

When the FASTMAP autoshimming method is applied to the "neck phantom", the use of both 1^{st} and 2^{nd} order shimming gives improved spectral linewidths as compared to manual shimming of the linear shims, an improvement from 2.3 Hz to 2.0 Hz.

The results for the human brain spectroscopy study, where both the sample and B_1 field of the RF coil are homogeneous, showed again that both 1^{st} and 2^{nd} order FASTMAP shimming performs better than traditional iterative manual linear shimming techniques.

The large susceptibility variations within the thyroid region of the neck make it difficult to use 2^{nd} order shim coils for improved homogeneity because the required shim

values are not achievable with the SCM used on the MRI system. Instead, only the 1st order shims can be adjusted. The FASTMAP method performs much better than iterative manual adjustments for the same total shimming time. The reduced shimming time means more time for data acquisition and less time that the subject has to spend in the scanner.

4.6 References

1. D. I. Hoult, D. Lee, Shimming a superconducting nuclear-magnetic-resonance imaging magnet with steel. *Rev. Sci. Instrum.* **56**(1), 131-135 (1985).
2. K. M. Lüdeke, P. Röschmann, R. Tischler, Susceptibility artifacts in NMR imaging. *Magn. Reson. Imaging* **3**, 329-343 (1985).
3. D. T. Edmonds, M. R. Wormald, Theory of resonance in magnetically inhomogeneous specimens and some useful calculations. *J. Magn. Reson.* **77**, 223-232 (1988).
4. R. Bhagwandien, R. van Ee, R. Beersma, C. J. G. Bakker, M. A. Moerland, J. J. W. Lagendijk, Numerical analysis of the magnetic field for arbitrary magnetic susceptibility distributions in 2D. *Magn. Reson. Imaging* **10**, 299-313 (1992).
5. L. F. Fuks, F. S. C. Huang, C. M. Carter, W. A. Edelstein, P. B. Roemer, Susceptibility, lineshape, and shimming in high-resolution NMR. *J. Magn. Reson.* **100**, 229-242 (1992).
6. C. S. Li, T. A. Frisk, M. B. Smith, Computer simulations of susceptibility effects: implications for lineshapes and frequency shifts in localized spectroscopy of the human head, in "Proc., SMRM, 12th Annual Meeting, 1993," p.912.
7. R. Bhagwandien, M. A. Moerland, C. J. G. Bakker, R. Beersma, J. J. W. Lagendijk, Numerical analysis of the magnetic field for arbitrary magnetic susceptibility distributions in 3D. *Magn. Reson. Imaging* **12**, 101-107 (1994).

8. J. C. Sharp, J. K. Saunders, Calculation of the static magnetic field in nonuniform media. *J. Magn. Reson., Series B* **108**, 58-66 (1995).

9. F. Roméo, D. I. Hoult, Magnet field profiling: analysis and correcting coil design. *Magn. Reson. Med.* **1**, 44-65 (1984).

10. H. Wen, F. A. Jaffer, An *in vivo* automated shimming method taking into account shim current constraints. *Magn. Reson. Med.* **34**, 898-904 (1995).

11. W. W. Conover, in "Topics in carbon 13 magnetic resonance spectroscopy" (G. Levy, ed.), Vol. 4, Chap. 2, Wiley, New York, 1984.

12. D. I. Hoult, "Shimming" on spatially localized signals. *J. Magn. Reson.* **73**, 174-177 (1987).

13. I. S. Mackenzie, E. M. Robinson, A. N. Wells, B. Wood, A simple field map for shimming. *Magn. Reson. Med.* **5**, 262-268 (1987).

14. A. A. Maudsley, H. E. Simon, S. K. Hilal, Magnetic field measurement by NMR imaging. *J. Phys. E: Sci. Instrum.* **17**, 216-220 (1984).

15. J. Tropp, K. A. Derby, C. Hawryszko, Automated shimming of B_0 for spectroscopic imaging. *J. Magn. Reson.* **85**, 244-254 (1989).

16. K. Sekihara, S. Matsui, H. Kohno, A new method of measuring static field distribution using modified Fourier NMR imaging. *J. Phys. E.* **18**, 224-227 (1985).

17. M. G. Prammer, J. C. Haselgrove, M. Shinnar, J. S. Leigh, A new approach to automatic shimming. *J. Magn. Reson.* **77**, 40-52 (1988).

18. E. Schneider, G. Glover, Rapid *in vivo* proton shimming. *Magn. Reson. Med.* **18**, 335-347 (1991).

19. P. Webb, A. Macovski, Rapid, fully automatic, arbitrary-volume *in vivo* shimming. *Magn. Reson. Med.* **20**, 113-122 (1991).

20. F. Schick, O. Lutz, Simultaneous determination of the macroscopic and microscopic static magnetic field inhomogeneity (MAGNUS). *J. Magn. Reson., Series B* **102**, 35-46 (1993).

21. R. Gruetter, Automatic, localized *in vivo* adjustment of all first- and second-order shim coils. *Magn. Reson. Med.* **29**, 804-811 (1993).

22. P. A. Bottomley, Selective volume method for performing localized NMR spectroscopy. U.S. Patent 4 480 228 (1984).

23. J. Frahm, K.-D. Merboldt, W. Hänicke, Localized proton spectroscopy using stimulated echoes. *J. Magn. Reson.* **72**, 502-508 (1987).

24. R. J. Ordidge, A. Connelly, J. A. Lohman, Image-selected *in vivo* spectroscopy (ISIS). A new technique for spatially selective NMR spectroscopy. *J. Magn. Reson.* **66**, 283-294 (1986).

25. J. C. Sharp, M. O. Leach, D. J. Collins, A single-shot shimming sequence using low-power RF noise pulses for localized *in vivo* NMR spectroscopy. *Phys. Med. Biol.* **37**, 281-287 (1992).

26. R. Kimmich, D. Hoepfel, Volume-selective multipulse spin-echo spectroscopy. *J. Magn. Reson.* **72**, 379-384 (1987).

27. D. M. Doddrell, G. J. Galloway, I. M. Brereton, W. M. Brooks, Nodal inhomogeneity mapping by localized excitation – the "NIMBLE" shimming technique for high-resolution *in vivo* NMR spectroscopy. *Magn. Reson. Med.* **7**, 352-357 (1988).

28. R. Gruetter, C. Boesch, Fast, noniterative shimming of spatially localized signals. *In vivo* analysis of the magnetic field along axes. *J. Magn. Reson.* **96**, 323-334 (1992).

Chapter 5

PULSE SEQUENCE OPTIMIZATION: REDUCTION OF CONTAMINATION AND MOTION RELATED ARTIFACTS

5.1 Introduction

In vivo MR spectroscopy of the thyroid gland suffers from large B_0 inhomogeneities near the trachea (see Ch. 4) as well as motion artifacts caused by arterial and venous blood flow, physiological motion, respiration artifacts, and bulk motion associated with any *in vivo* experiment.

As discussed in the previous chapter, a single shot localization sequence such as STEAM or PRESS is preferred to a multi-acquisition sequence like ISIS because manual and automatic shimming modalities are easily accommodated. Multi-acquisition sequences are also inherently more sensitive to motion because the add and subtract nature of the technique assumes that the individual slice positions have not moved, which cannot be guaranteed.

Comparing PRESS and STEAM localization, several factors need to be considered: the quality of the localized volume, spin displacement effects, minimum attainable TE, water suppression, homonuclear coupling effects, and the influence of B_1 inhomogeneity (2). The advantages of PRESS are that it offers a factor of two gain in SNR and is less sensitive to motion and spin displacement effects, with no sensitivity to multiple quantum effects. However, STEAM offers advantages in localization quality, minimum TE attainable, and water suppression. During the TM period of the STEAM sequence, T_1

relaxation dominates since magnetization is along the longitudinal axis rather than in the transverse plane as in PRESS. Therefore, in the case of *in vivo* spectroscopy where T_2 values are short compared to T_1, the shorter TE attainable with STEAM would lead to increased SNR with respect to PRESS. Finally, in surface coil spectroscopy the inhomogeneous B_1-field will cause degraded localization for both techniques, but because PRESS has a stronger functional dependence on flip angle, PRESS localization with a surface coil will be worse than with STEAM, and therefore the overall SNR will be further reduced.

The quality of localized spectra obtained using both the STEAM and PRESS sequences is strongly dependent on the strength and placement of the spoiler gradient pulses (1-4) as well as the RF pulse and receiver phase cycling scheme (5-7).

To reduce the artifacts created from motion due to respiration or blood flow, ECG/respiratory gating may be used (8). That is, the pulse sequence is repeated at the same time point in the ECG/respiratory cycle by synchronizing with an electrical signal produced from the appropriate monitoring device. Another method of motion artifact reduction post-corrects the data by calculating the frequency and phase variations between acquired FID's and making the appropriate corrections (9).

When spectroscopic localization procedures such as PRESS or STEAM are used, eddy currents are induced in the metallic bore tube to oppose the effect of the pulsed field gradients. This causes time-dependent B_0 shifts that decay to zero on the order of tens of milliseconds, since the eddy currents are dissipated through resistive effects (10). The resulting spectrum may have major distortions which can significantly obscure spectral

resonances. One method of overcoming this problem is to measure the B_0 variation as a function of time and correct the FID accordingly.

Recently, Ernst et al. showed that the slice selection order is also an important parameter for frontal lobe brain spectroscopy, where contamination from the sinus region has been observed (11). In the case of *in vivo* MR spectroscopy of the thyroid gland, the VOI is placed near the surface of the neck as well as next to the trachea. Therefore, there may be a need for pulse sequence optimization to reduce contamination.

5.2 Theory

5.2.1 B_1 Inhomogeneity Effects: Comparing PRESS and STEAM

The flip angle dependence on the available signal for the three slice selective RF pulses (θ_1, θ_2, θ_3) of PRESS is given by

$$S_{PRESS}(t) \propto \sin\theta_1 \sin^2(\frac{\theta_2}{2})\sin^2(\frac{\theta_3}{2}), \qquad [5.1]$$

whereas the corresponding dependence for STEAM is given by

$$S_{STEAM}(t) \propto \sin\theta_1 \sin\theta_2 \sin\theta_3 . \qquad [5.2]$$

In the case that an RF coil with some degree of B_1 inhomogeneity is used, assume that the flip angle produced at the center of the voxel is the optimum value (90° for STEAM). For a point near the edge of the defined voxel, where the flip angle may differ from the optimum value, the loss in transverse magnetization results in sub-optimal localization and decreased SNR. Since $\theta \propto B_1$, the ratio of the signal loss at positions away from the center of the voxel for the two sequences can be found simply from the calculated B_1 distribution of the particular coil. For the research involved in this thesis,

transmit/receive surface coils were used, such that the flip angle at the inner edge of a 1 cm^3 voxel could be 1.35 times larger than at the center (as for the standard 5-cm diameter single-ring surface coil used in Ch. 3). This would result in approximately 56% loss in available signal for PRESS compared to 39% for STEAM, a difference of 72%. For larger voxel sizes, the effect would be larger.

Comparing PRESS and STEAM, i*n vivo* proton spectroscopy using the latter provides improved water suppression and shorter echo times with superior localization, and is less sensitive to B_1 inhomogeneity. These factors are usually considered to offset the factor-two signal loss encountered when using stimulated echoes (9). Because methods will be developed to compensate for the possible increased sensitivity to motion, the STEAM sequence was used for all spectroscopy experiments.

5.2.2 Motion: Analysis and Correction

During an NMR experiment, physiologic motion or diffusion can cause artifacts in the resulting image or spectrum. Motion can be characterized into three periods/components: 1) motion during the pulse sequence, 2) motion during the acquisition period, and 3) motion during the recovery time between sequence repetitions. The effect of motion during an experiment is to create phase and/or frequency mismatches between acquisitions, thereby increasing linewidths and lowering the SNR of the corresponding summed or averaged FID. A complete description of motion is discussed below while a correction procedure is given in Section 5.2.6.

Period-1 motion can cause different bulk phase changes of the final magnetization for different acquisitions and irretrievable signal loss due to improperly refocused spins,

depending on the amount of motion. The phase change can be corrected by phase correcting the spectra of individual acquisitions before averaging (9) (see Section 5.2.6). One can theoretically analyze the effects of motion during a sequence of RF and bipolar gradient pulses by calculating the total phase change for stationary spins (at position x_0) as well as spins moving with velocity v_0 (and acceleration a_0) and thus determining the corresponding gradient moments. For a group of spins moving in a gradient $G(t)$, if the position as a function of time is given by

$$x(t) = x_0 + v_0\, t + \frac{a_0 t^2}{2} + \ldots, \qquad [5.3]$$

the phase of the resulting signal as a function of time is given by

$$\varphi(t) = x_0 \int G(t')\,dt' + v_0 \int G(t')\,t'\,dt' + \frac{a_0}{2} \int G(t')\,t'^2 dt' + \ldots \qquad [5.4]$$

$$\text{or} \quad \varphi(t) = x_0\, M0 + v_0\, M1 + a_0\, M2 + \ldots, \qquad [5.5]$$

where M0, M1, M2, etc. are the moments of the gradient waveforms with respect to time. If the resulting phase contributed from a particular moment is not zero, signal loss will result when the ensemble average is taken (volume localization).

For both the stimulated echo in STEAM, and the double spin echo in PRESS, the zeroth order moment is always made zero by ensuring that the bipolar gradient areas add to zero for each of the three gradient directions (G_x, G_y, G_z). To minimize the creation of higher order moments, an opposite polarity gradient with equal area can be applied immediately after slice selection. Single shot volume selective pulse sequences such as PRESS and STEAM require spoiler (or "crusher") gradient pulses to remove ("spoil" or "crush") unwanted coherences originating from outside the voxel (see Ch. 1). Unfortunately, these spoiler pulses cause higher order gradient moments. In STEAM, the

spoiler gradient pulses responsible for creating gradient moments are separated by a minimum time of TM, resulting in unavoidable higher order moments which, depending on the amount of motion, will cause possible signal loss. Using gradient moment analysis, it can be seen that if the 180° RF pulses of the PRESS sequence are sandwiched tightly between spoiler gradient pulses of equal length and amplitude, the PRESS sequence will be much less sensitive to motion than the STEAM sequence. Finally, it is worth noting that the use of stronger spoiler gradient pulses (see Section 5.2.3) will cause these higher order gradient moments to be larger, with consequent increased sensitivity to motion.

Period-2 motion during the acquisition of the FID can cause transient effects on the FID as well as bulk phase changes that again may be different for different acquisitions if the motion is not consistent. The transient effects can be partially corrected using traditional eddy current correction algorithms (see Section 5.2.5).

The effect of starting an acquisition sequence at different times within a characteristic cycle of motion (such as respiration) or in random motion, is to again create a total phase difference between acquisitions. This period-3 motion during the recovery time between acquisitions can again be corrected by separately acquiring FID's and individually phase correcting each FID before summation. Alternatively, ECG or respiratory gating can be used to ensure that the data are acquired during the same cycle of motion, thus eliminating the variation between acquisitions.

5.2.3 STEAM: Optimization of Crusher Strength and Position

As discussed in Chapter 1, there are eight different coherences that exist for a STEAM sequence (with three RF pulses) (Fig. 5.1): three FID's, three spin echoes, one double spin echo and one stimulated echo. Spoiler gradient pulses are required to destroy unwanted coherences such as FID signals from the three slabs (excluding the VOI) and spin-echoes from the intersection of two slabs resulting in a column (excluding the VOI). These unwanted signals are removed by destroying their phase coherence. From gradient moment analysis, it is the M0 moment that is responsible for the removal of phase coherence. The larger the integral over time of the gradient (area under gradient in Fig. 5.1), the less phase coherence exists for a particular coherence. When crushers are used on more than one axis, the resulting gradient moments add in quadrature to decrease coherence. An M0 gradient moment analysis for the STEAM sequence shown in Fig. 5.1 is summarized in Table 5.1 with a few examples of possible **A/B** ratios.

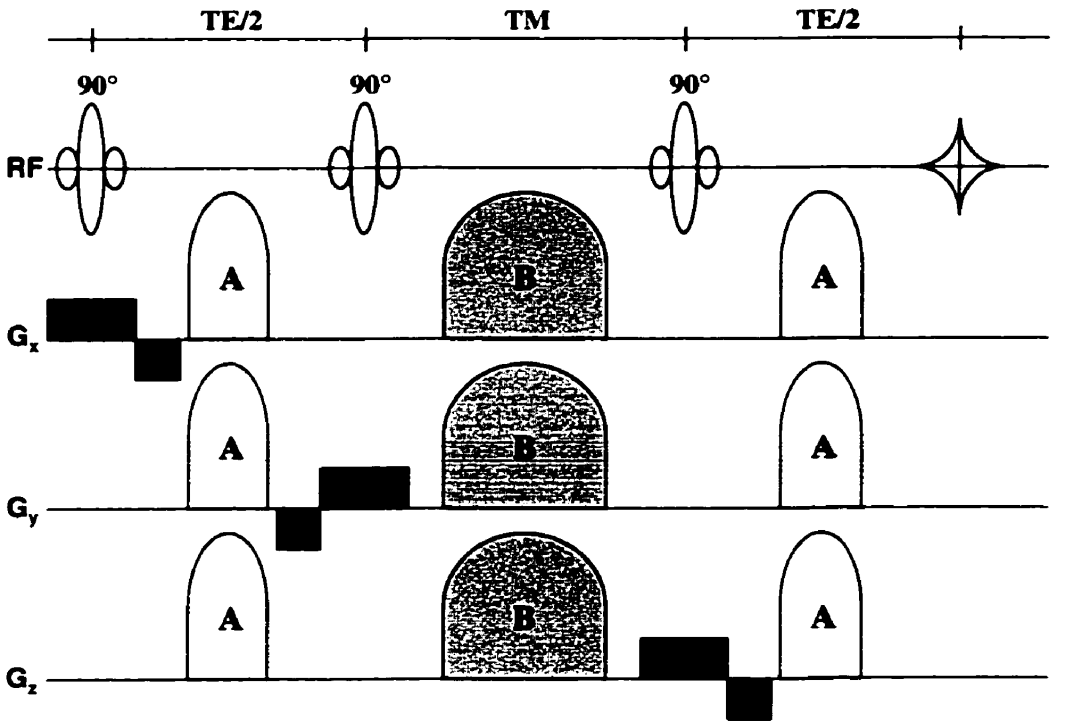

Figure 5.1 STEAM localization pulse sequence. The M0 gradient moment (or gradient area) for each TE-crushers and TM-crushers are labeled **A** and **B** respectively.

Table 5.1 M0 gradient moment analysis for the STEAM sequence of Fig. 5.1

Coherence	Non-Refocused Gradient Area (Coherence Spoiling)	Coherence Spoiling - Examples	
		A = 2B	**B = 3A**
FID1 (90-0-0)	$\sqrt{3}\mathbf{A} + \sqrt{3}\mathbf{B} + \sqrt{3}\mathbf{A} = \sqrt{3}(2\mathbf{A} + \mathbf{B})$	$5\sqrt{3}\mathbf{B} = (5/2)\sqrt{3}\mathbf{A}$	$5\sqrt{3}\mathbf{A}$
FID2 (0-90-0)	$\sqrt{3}(\mathbf{A} + \mathbf{B})$	$3\sqrt{3}\mathbf{B} = (3/2)\sqrt{3}\mathbf{A}$	$4\sqrt{3}\mathbf{A}$
FID3 (0-0-90)	$\sqrt{3}\mathbf{A}$	$2\sqrt{3}\mathbf{B} = \sqrt{3}\mathbf{A}$	$\sqrt{3}\mathbf{A}$
SE1-2 (90-90-0)	$\sqrt{3}\mathbf{A} - \sqrt{3}\mathbf{B} - \sqrt{3}\mathbf{A} = -\sqrt{3}\,\mathbf{B}$	$-\sqrt{3}\mathbf{B} = -(1/2)\sqrt{3}\mathbf{A}$	$-3\sqrt{3}\mathbf{A}$
SE1-3 (90-0-90)	$\sqrt{3}\mathbf{A} + \sqrt{3}\mathbf{B} - \sqrt{3}\mathbf{A} = \sqrt{3}\,\mathbf{B}$	$\sqrt{3}\mathbf{B} = (1/2)\sqrt{3}\mathbf{A}$	$3\sqrt{3}\mathbf{A}$
SE2-3 (0-90-90)	$\sqrt{3}\mathbf{B} - \sqrt{3}\mathbf{A} = -\sqrt{3}(\mathbf{A} - \mathbf{B})$	$-\sqrt{3}\mathbf{B} = -(1/2)\sqrt{3}\mathbf{A}$	$2\sqrt{3}\mathbf{A}$
SEE1-2-3 (90-90-90)	$\sqrt{3}\mathbf{A} - \sqrt{3}\mathbf{B} + \sqrt{3}\mathbf{A} = \sqrt{3}(2\mathbf{A} - \mathbf{B})$	$3\sqrt{3}\mathbf{B} = (3/2)\sqrt{3}\mathbf{A}$	$-\sqrt{3}\mathbf{A}$
STE1-2-3 (90-90-90)	$\sqrt{3}\mathbf{A} - \sqrt{3}\mathbf{A} = \mathbf{0}$	**0**	**0**

Looking at the non-refocused gradient area for SE2, it is clear that **A** cannot equal **B**, otherwise a spin echo from the last two RF pulses is refocused and results in contamination. The second example (**B** = 3**A**) does a better job of destroying unwanted coherences, except for the double spin-echo (SEE 1-2-3). The signal from the double spin-echo (SEE 1-2-3) does come from the voxel and therefore may not represent actual contamination. As the spins only experience T_1-relaxation during the TM period, the TM-crusher can be made much larger than the TE-crusher by increasing its length, hence increasing only TM.

Therefore, if **A** (and also **B**) is made larger, while ensuring that **A** is much different from **B**, the sequence will be most efficient at destroying unwanted coherences. The price paid is increased susceptibility to motion and the production of larger eddy currents, placing more importance on eddy current correction of the spectroscopic data (see Section 5.2.5).

As described above, the STEAM sequence (Fig. 5.1) is more susceptible to motion if the crusher gradient pulses are stronger and separated by longer times. Therefore, for a given crusher strength and TE/TM, it is necessary to minimize motion artifacts. This can be accomplished by placing the TE-crushers as close together as possible. That is, the first TE-crusher is applied just before the second slice selection, leaving any time delay, required to obtain a specific TE between the first slice selection and the start of the TE-crusher. The second TE-crusher is applied immediately after the third slice selection, leaving any required delays until after the crusher. This usually means that the refocusing lobes of the slice selection gradients are incorporated into the TE-crushers. Of

course, minimizing the TM period also reduced motion susceptibility, but this then may increase susceptibility to contamination because the TM gradient area, **B**, will be smaller.

5.2.4 STEAM: Optimizing the Slice Selection Order

As explained previously, in the STEAM sequence (Fig. 5.1), the stimulated echo comes from the intersection of three slabs, excited by each of the 90° slice selective pulses. From the M0 gradient moment analysis shown in Table 5.1, the two coherences most likely to produce contamination are the FID from the third 90° pulse (FID3) and the spin echo from the last two pulses (SE2-3). The FID3 represents signal from a slab obtained by the last slice selection (excluding the VOI), extending two-dimensionally, perpendicular to the slice selection axis. In the pulse sequence of Fig. 5.1, this slab extends into the x-y plane. The SE2-3 represents signal from the intersection of two slabs created by the last two slice selections, resulting in a column that excludes the voxel of interest. This column extends one-dimensionally perpendicular to both of the last two slice selection axes. In the pulse sequence of Fig. 5.1, this column extends in the x-direction.

To experimentally identify the unwanted coherences that cause the strongest contamination, the three flip angles of the STEAM sequence may be varied. The RF pulses should be applied at their nominal 90°, or set to zero. If the non-refocused gradient area of the sequence is sufficient, no signal should be observed. For instance, by applying the RF pulses such that the flip angles are 0° - 90° - 90°, the SE2-3 coherence is selected.

5.2.5 Eddy Current Correction

To correct for eddy current artifacts in spectra, the B_0 variation has to be measured as a function of time. A simple method is to measure the phase of an on-resonance signal following a gradient pulse.

The NMR signal, $S_j(t)$, for spins with chemical shift σ_j located in a time dependent magnetic field $B_0+\Delta B_0(t)$, is given by (10)

$$\begin{aligned} S_j(t) &= \exp\left(i[\gamma(B_0 + \Delta B_0(t))(1-\sigma_j)t] + \frac{t}{T_2} \right) = S_{0j}(t)\exp\left(i\gamma\Delta B_0(t)(1-\sigma_j)t\right) \\ &= S_{0j}(t)\exp\left(i\gamma\Delta B_0(t)t\right)\exp\left(i\gamma\Delta B_0(t)t\sigma_j\right) \end{aligned}, \quad [5.6]$$

where $\Delta B_0(t)$ is caused by a gradient pulse perturbation, such as eddy currents. If the FID signal is dominated by a single isochromat at resonance, then σ_j is small and therefore the time dependent FID following a gradient pulse is given by

$$S_j(t) \cong S_{0j}(t)\exp\left(i\gamma\Delta B_0(t)t\right). \quad [5.7]$$

Furthermore, for an on-resonance FID and a symmetric lineshape (10),

$$\left|S_j(t)\right|_{magnitude} = S_{0j}(t), \quad [5.8]$$

and therefore the time-dependent phase of the FID signal, $\varphi_j(t)$, fully characterizes the eddy current term in Eq. [5.7]. If it is now assumed that all other spins with chemical shift σ_k experience the same time-dependent eddy current effects, such that

$$S_k(t) \cong S_{0k}(t)\exp\left(i\gamma\Delta B_0(t)t\right), \quad [5.9]$$

the FID signal without eddy current artifacts, $S_{0k}(t)$, can be found by multiplying the measured eddy current-affected FID signal by $\exp[-i\varphi_j(t)]$,

$$S_{0k}(t) \cong S_k(t)\exp\left(-i\varphi_j(t)\right). \quad [5.10]$$

The effect of having the original reference FID signal, $S_j(t)$, off resonance, is to introduce a constant frequency offset to the final eddy current-corrected spectrum, and is therefore easily accomodated.

5.2.6 Automatic Frequency and Phase Correction of Individual Spectra

A simple method of shifting a spectrum to a different frequency is to calculate first the magnitude spectrum, then iteratively search for the maximum peak intensity within a specified frequency range, and finally shift the spectrum such that this peak moves to the desired position. This is easily accomplished with any computational engine. The frequency range should be chosen such that there is only one main metabolite peak within the range. This may be performed on the residual water signal after partial water suppression or on a particular well-resolved metabolite peak with adequate signal intensity.

One method of phase correction is to calculate the phase of each FID from the real and imaginary parts at time = 0. This works well when the water signal dominates the individual FID's, but not when the water signal does not dominate, such as water suppressed data. In this case, the phase of the frequency-domain spectrum is calculated from the real and imaginary points at the position of the maximum intensity of water (or other metabolite) in the magnitude spectrum.

Several problems arise when phasing on the residual water signal. First, there has to be enough water left over to obtain the desired lineshape. Second, for *in vivo* spectroscopy in regions of extreme B_0 inhomogeneity, any significant water signal left unsuppressed will overpower information from other metabolites. Therefore, phase

correction on a metabolite peak would be beneficial, leaving one to suppress fully the water resonance.

Automatic phase correction by phase calculation on low SNR metabolite peaks is plagued with difficulty, thereby making manual adjustments a normal practice (14). This arises because the phase calculation fails if a significant amount of noise is present in the spectrum. Another problem with phase correcting individually acquired spectra is that after the spectra have previously been frequency shifted, any differences in individual phase shifts, will cause different individual frequency shifts to be added, again rendering increased linewidths. In general then, it is important to phase correct individual spectra before frequency correction. Of course, the frequency shifting could be repeated after phase correction, but this becomes time consuming.

A method that may overcome both of the problems mentioned above is to phase correct after frequency correction on individual spectra using a maximum peak intensity searching method rather than a phase calculation method. In this new method, the phase of the individual spectrum is adjusted until the maximum intensity of the metabolite peak, in the real spectral domain, is matched to the predetermined frequency shift point. This method works on the assumption that the frequency position of the maximum intensity of the peak modulus corresponds to the frequency position of the maximum intensity of the same metabolite peak in the real spectrum. This peak maximum finding method may be less sensitive to spectral noise than the phase calculation method.

5.3 Experimental

All experiments were performed with a Bruker/Magnex 3T MSLX scanner on normal volunteers. Actively shielded, 20mT/m, gradients were used. Either the 5-cm standard surface coil or the three-ring surface coil described in Ch. 3 were used for these studies. The basic STEAM sequence of Fig. 5.1 was used for data collection, modified such that the refocusing lobes of the slice selection gradients were incorporated into the TE-crushers. TE- and TM-crusher areas were varied by altering both the gradient length and strength. Due to limitations in time permitted for a particular patient study, SE2-3 coherence experiments were done using 4 prescans and 64 averaged acquisitions. STEAM experiments were done using 4 prescans and 128 individual stored acquisitions. Spectra were processed by first doubling the number of points in the spectra by zero filling, and reducing the noise by means of an exponential multiplier equivalent to 2 Hz line broadening.

ECG/respiratory gating was done using the Omni-Trak Vital Signs Monitoring Systems (Model #3100 and 3108-2) from Invivo Research, Inc. (Orlando, USA), with 3M Red Dot Ag/AgCl Monitoring Electrodes (London, Canada), and an ECG Electrode Impedance Meter (Invivo Research, Inc.). For the ECG measurement, the four leads were placed on the subject's back adjacent to the heart but offset slightly to the subject's left, according to the manufacturer instructions. For the respiratory signal measurement, the four leads were placed on the subject's back, adjacent to the left lung, positioned lower and further to the subject's left than for ECG measurement.

Eddy current correction, as well as automatic/manual frequency and phase corrections, were done using an IDL program written by Dr. L. Friesen at the Institute for

Biodiagnostics, National Research Council of Canada (14). The automatic phase correction algorithm described previously was incorporated into the program and tested on normal thyroid spectra. Depending on the SNR, the individual spectra were line broadened until the peak of interest had a SNR such that center frequency determination did not fail due to noise in the spectrum. The frequency and phase shifts were then stored and applied to the original FID's. In addition, the standard deviation of frequency shifts was calculated for correlation with linewidth reduction.

5.4 Results and Discussion

5.4.1 Optimizing the Slice Selection Order

In order to investigate the effect of slice selection order on the amount of contamination in localized ^{1}H MR spectra, experiments were performed on the "neck" phantom described in Ch. 4 (Fig. 4.2). It was found that the amount of contamination with such "ideal" samples was too small to see any significant effects of slice-selection-order optimization. Therefore, localized spectroscopy experiments were done *in vivo* on the thyroid gland of healthy volunteers. From these *in vivo* studies, it was found that the SE2-3 coherence was responsible for the largest contamination effect, therefore, data were collected to measure this coherence as well as the stimulated echo.

In the first example, the TE/TM crusher area ratio (A/B) was 2.0, which was accomplished with a TE-crusher 4.0 ms in length at 50% of maximum strength, and TM-crushers 4.0 ms in length at 25% of maximum strength. The TM used in this case was 15 ms and the TE was 20 ms. All six possible non-oblique orientations were tested. The best and worst case results are shown in Fig. 5.2, for the SE2-3 coherence. The y-x-z and

x-y-z slice selection orders had similar results, but the y-z-x order was clearly the worst. This contamination results in spectra with irregular phase characteristics, which makes phasing to obtain the typical absorption spectrum impossible. The resulting STEAM spectra for the two different slice selection orders are shown in Fig. 5.3. Although there may appear to be a small amount of contamination visible for the y-x-z order, it is not dramatic. The spectrum obtained with the y-z-x slice selection order has a large contamination artifact, with an out of phase signal dipping well below the baseline resulting in a poor quality spectrum.

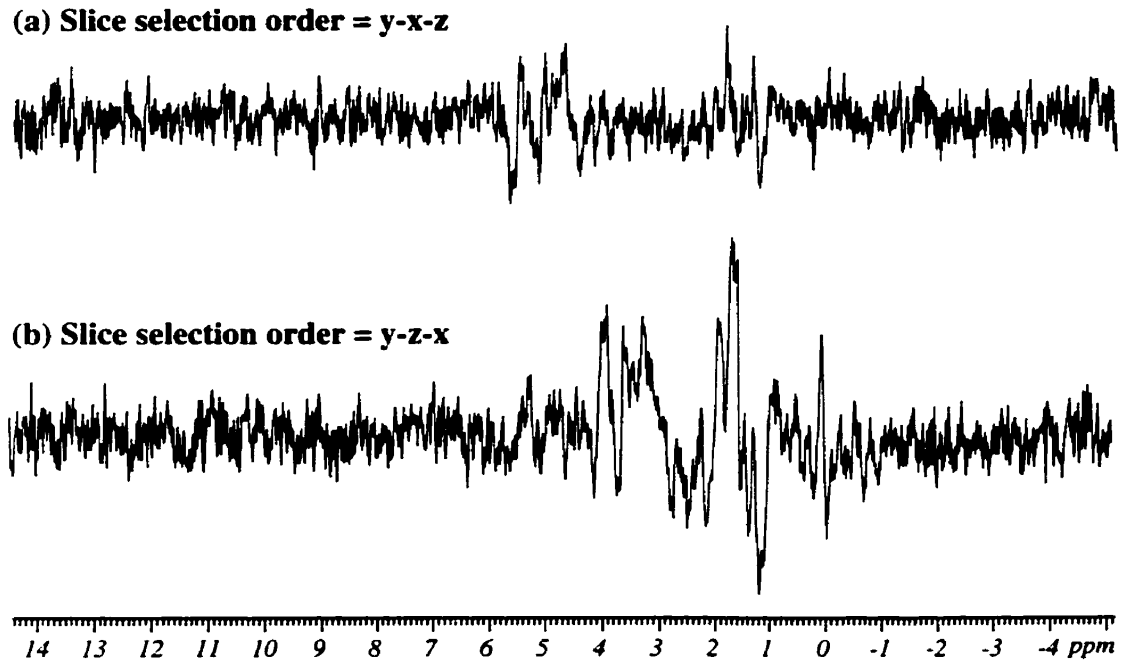

Figure 5.2 Spectra taken from a normal volunteer for observation of the SE2-3 coherence (0°-90°-90°). (a) The best slice selection order y-x-z and (b) the worst slice selection order y-z-x.

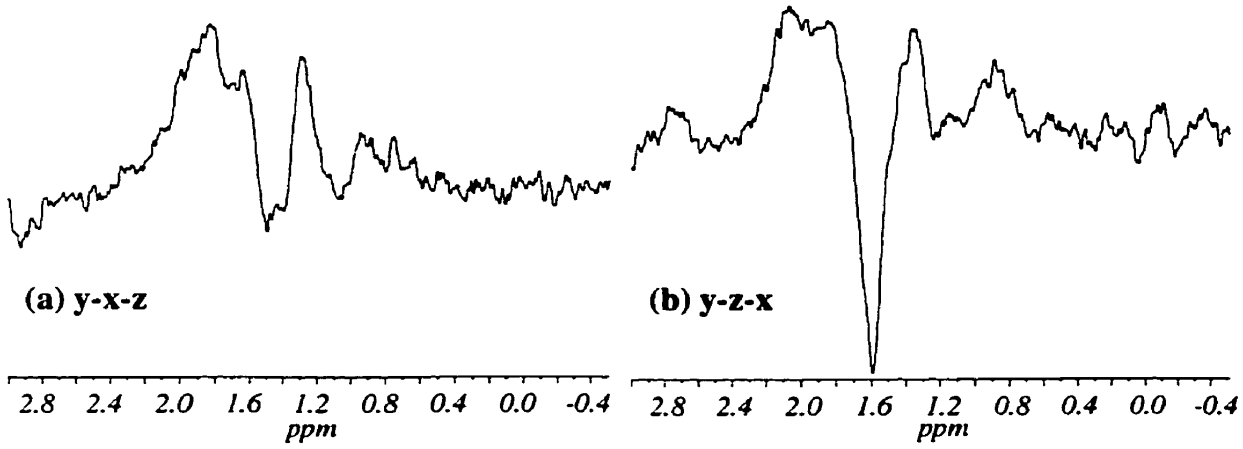

Figure 5.3 Corresponding *in vivo* 1H MR spectra using STEAM (90°-90°-90°) for (a) the best slice selection order y-x-z and (b) the worst slice selection order y-z-x.

In the second example, the TE/TM crusher area ratio (A/B) was 1/3, which was accomplished with a TE-crusher 4.0 ms in length at 50% of maximum strength, and TM-crushers 12.0 ms in length at 50% of maximum strength. The TM used in this case needed to be increased to 18 ms to accommodate the longer TM-crusher and the TE was again 20 ms. The spectra in Fig. 5.4 show the difference in spectral quality when the optimum slice selection order is used. The x-y-z order produced no visible contamination artifact while the z-y-x slice selection order produced the characteristic out of phase signal dipping below the baseline.

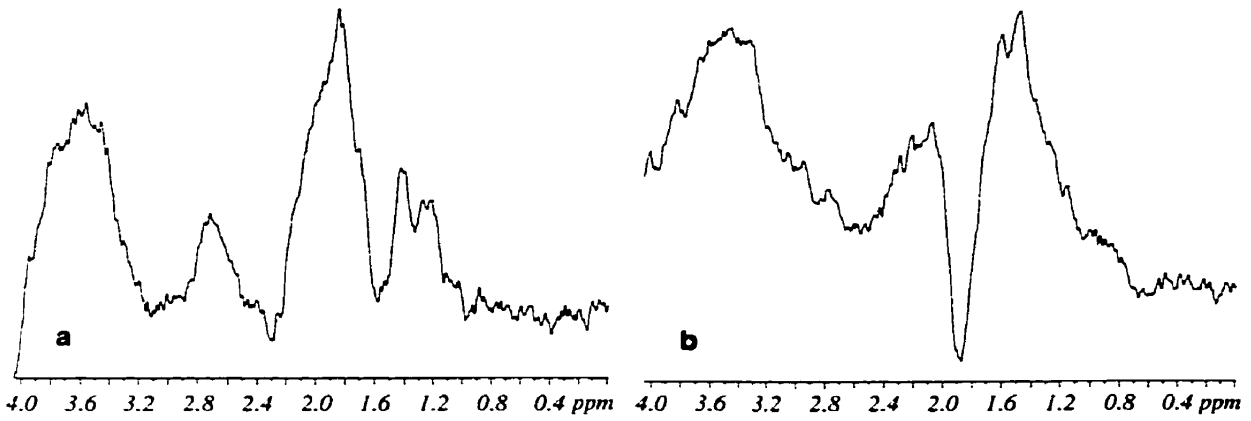

Figure 5.4 *In vivo* thyroid spectra from the same normal subject using slice selection orders (a) x-y-z and (b) z-y-x.

Although the introduction of increased crushing of unwanted coherences using a TE/TM gradient area ratio such that **B=3A** may have reduced the amount of contamination slightly (Fig. 5.4a), there is still a definite requirement to use the x-y-z slice selection order over the z-y-x order. In general, it was found that either the x-y-z or y-x-z slice selection orders produced spectra with little or no contamination artifact, with importance placed on having the last slice selection using the z-gradient.

5.4.2 Eddy Current Correction

The major effect of eddy currents on the spectra was to create antisymetric side lobes around every resonance in the spectrum (12,13). This effect is thought to be caused by an eddy current induced B_0 oscillation, rather than a gradient effect. The intensity of these side lobes is dependent on the amplitude and duration of the applied gradient pulse, and most easily seen for strong signals such as unsuppressed water or lipid dominated spectra. The effect of uncorrected eddy currents is shown in Fig. 5.5 for a lipid-dominated

spectrum. After eddy current correction using the time variation of phase for a water FID as a reference, the antisymmetric side lobes are removed leaving a typical lipid spectrum.

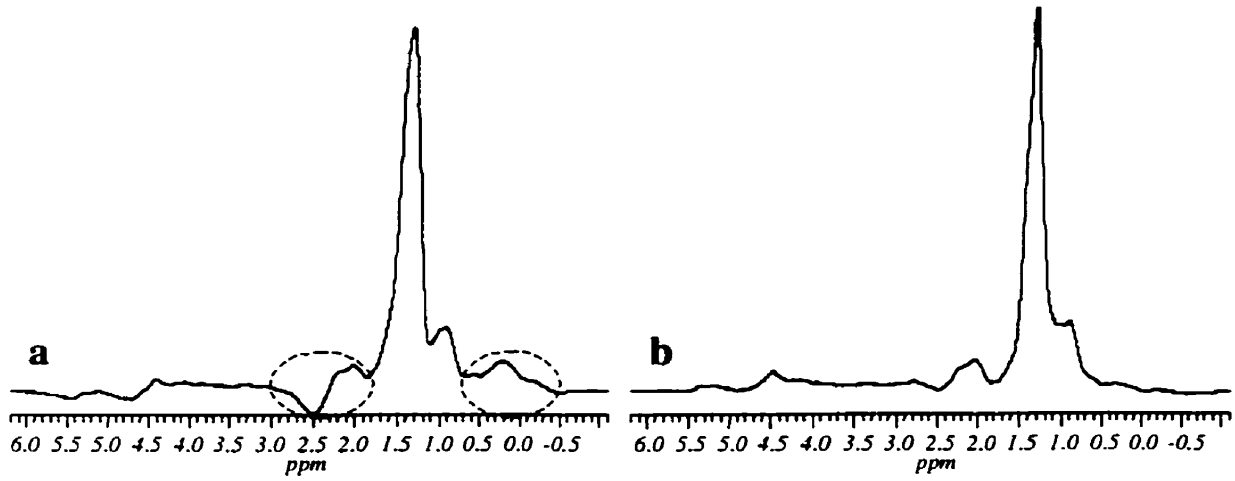

Figure 5.5 Lipid-dominated, water suppressed spectrum from a normal subject (a) without and (b) with eddy current correction. Eddy-current induced anitsymmetric side lobes are indicated in (a). Eddy current correction results in typical lipid spectrum showing major resonances at 0.9 ppm, 1.3 ppm, 2.0 ppm and 5.3 ppm.

5.4.3 Motion Artifact Reduction by ECG/Respiratory Gating

Although physical motion of the subject can potentially be a major source of motion artifact for *in vivo* spectroscopy, it can be prevented with appropriate restraints. Physiological movement of spins, motion produced by venous and arterial blood flow, and respiratory motion are not preventable and therefore play major roles in thyroid spectroscopy *in vivo*.

Motion artifacts can be easily seen by acquiring FID's and reconstructing the spectrum in real time, and then monitoring the frequency and/or phase changes between acquisitions. Although in all volunteers small phase shifts noticed, the frequency shifts

observed were significant and sometimes substantial. In one subject, the observed water peak shifted in frequency by ± 5 Hz from a central position.

With ECG leads placed on the subject's back, an ECG trace was monitored. The ECG signal repeated approximately every 0.8 seconds (heart rate 75 beats/min), with a flat response (isoelectric period) of about 0.6 seconds (Fig. 5.6). The sequence was triggered on the rising edge (at 70% of maximum) and a trigger delay was set such that acquisition started at the beginning of the flat response. In this way, most of the signal was acquired during a period of rest, since typical FID's from the thyroid *in vivo* have decayed to noise level within 0.3 seconds.

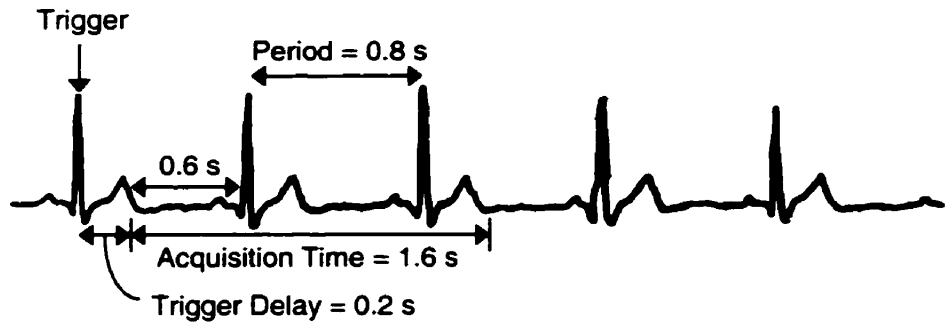

Figure 5.6 Typical ECG trace. Triggered on the peak, acquisition is started after the trigger delay time set such that the first portion of the FID is collected during the rest period.

With ECG triggering, the frequency shifting remained the same, resulting in the same spectral linewidth.

By far the largest contributor of motion artifact comes indirectly from respiratory motion. This is not from physical motion of the thyroid tissue but, rather, frequency and phase changes associated with magnetic field variations caused by the changing magnetic susceptibility at the position of the thyroid gland. The B_0 shift will depend on the

magnitude of susceptibility changes associated with a particular subject as well as the proximity of the tissue of interest to the lungs.

With the ECG leads again placed on the subject's back, a respiratory signal was then monitored. The respiratory signal repeated approximately every 4 seconds (respiratory rate 15 breaths/min), with a relatively flat response (end-expiratory phase) of about 1.6 seconds (Fig. 5.6). The sequence was again triggered on the rising edge and a trigger delay was set such that acquisition occurred during the flat response.

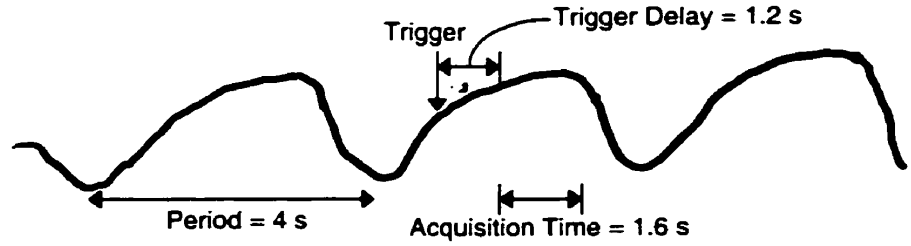

Figure 5.6 Typical respiratory signal trace. Triggered on the rising edge, acquisition is started after the trigger delay time set such that the FID is collected during a flat response.

With respiratory gating, the frequency shifting previously observed was reduced considerably, with just minor frequency variations. A comparison of the summed spectrum for 16 averages (without water suppression) with and without respiratory triggering is shown in Fig. 5.7. In this case, the water linewidth was decreased from 22.3 Hz to 21.1 Hz, an improvement of 1.2 Hz. As the period of the respiratory signal was typically about 4 seconds, the effective repetition time (TR) of the sequence was also 4 s. Occasionally, the system failed to trigger on the next respiratory pulse and an additional 4 s was added to the TR. Thus, for the same number of scans as a non-gated sequence of TR = 2 s, the respiratory gated data took at least two times longer. Consequently, for the same total time, the SNR of the gated experiment was reduced by half.

5.4.4 Motion Artifact Reduction by Frequency and Phase Correction

An alternative to respiratory gating is to collect and store the FID's separately, calculate individually the resultant frequency and phase-shifts, and correct the FID's accordingly. The sum of all corrected FID's would result in a reduced linewidth, by correcting for some of the effects of motion.

In the first example, individual frequency and phase correction was done to the respiratory gated data discussed previously. The corrections were done to the non-triggered data and compared to the result obtained with triggering (Fig. 5.7).

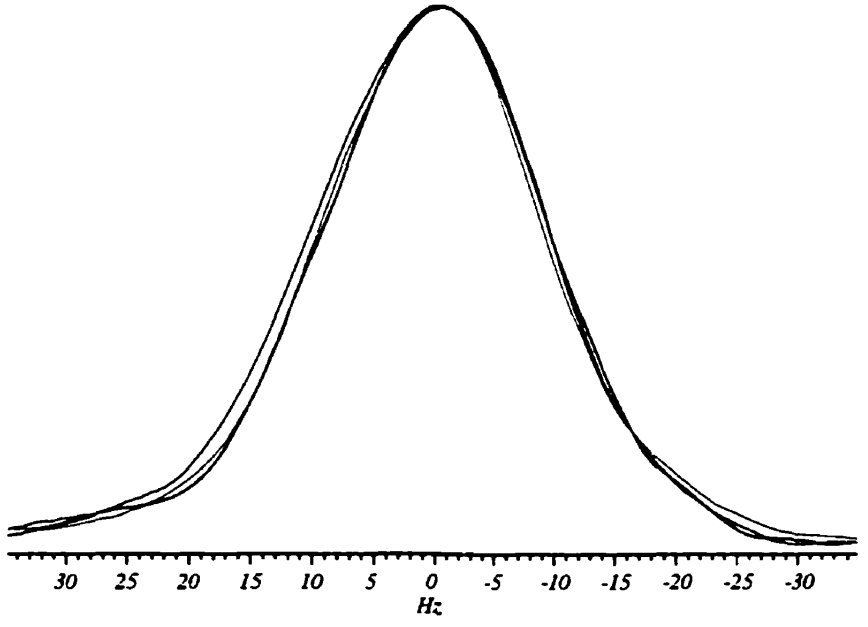

Figure 5.7 Unsuppressed water peak obtained with 16 averages with; no triggering, and no frequency/phase correction (blue), no triggering but frequency/phase corrected (black), and finally the respiratory triggered case (red).

The frequency-corrected linewidth of 21.5 Hz was slightly larger than the respiratory triggered linewidth by 0.4 Hz. This may be the effect of period-1 and period-2 motion described above. That is, in the triggered case, there was little motion during the application of the sequence or acquisition of the FID because acquisition is only done

during the flat respiratory response. In the non-triggered case, the application of the sequence is essentially random with respect to the respiratory signal and, therefore, some of the acquisitions would be collected during a high-motion portion of the respiratory signal, while others would be collected over the flat portion of the respiratory signal.

An average of five normal subjects showed that the standard deviation of frequency shifts averaged 3.1 Hz (range 2.56 Hz to 3.48 Hz), while the decrease in linewidth with individual frequency correction averaged 1.86 Hz (range 1.44 Hz to 2.5 Hz). The amount of linewidth reduction depends on the severity of the respiratory motion artifact and therefore would be expected to vary from patient to patient. An example of the modest improvement in spectral resolution is apparent in the *in vivo* water suppressed spectrum taken from a normal subject (Fig. 5.8). In this case, there was a decrease in overall linewidth of 1.5 Hz.

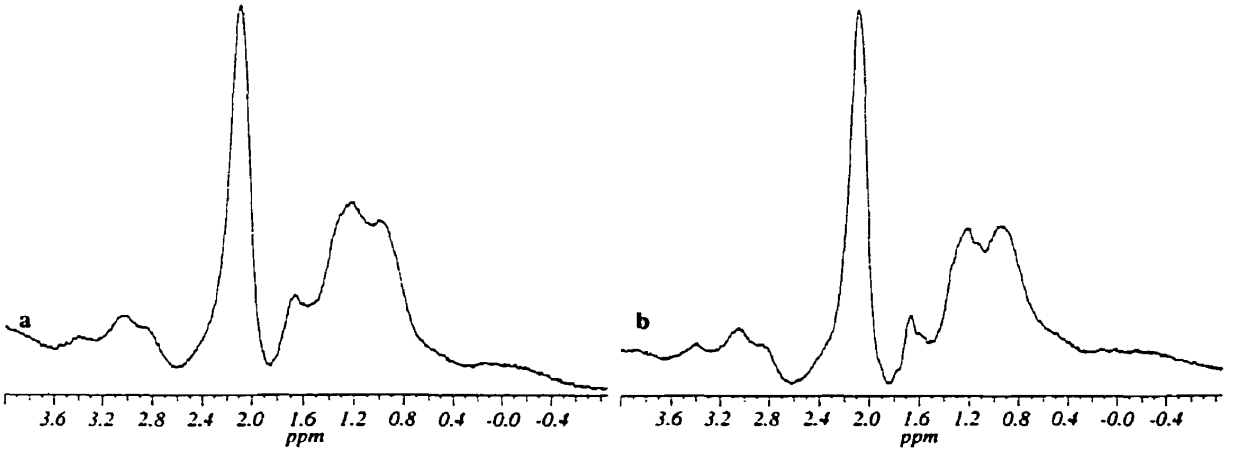

Figure 5.8 Water suppressed spectra from the thyroid of a normal subject (128 averages) (a) without and (b) with frequency and phase correction.

Both the automatic frequency and phase correction algorithms performed very well. Some manual frequency and phase tweaking was made to the automatic calculations for some of the *in vivo* data sets, but was not required for phantom data.

5.5 Conclusions

The STEAM single shot localization sequence was chosen over PRESS on a theoretical basis since STEAM offers improved localization quality, decreased sensitivity to B_1 inhomogeneity and a smaller TE. These factors are usually considered to offset the factor-two signal loss encountered when using stimulated echoes. Although the problem of signal loss from B_1 inhomogeneity is also more severe for PRESS than STEAM, this effect can be substantially reduced with a multi-ring surface coil and should not be a significant factor in choosing the optimal sequence.

Although PRESS is inherently less sensitive than STEAM to period-1 motion during the pulse sequence, both sequences have identical period-2 and period-3 motion characteristics during the acquisition and between acquisitions, respectively. Respiration, not motion due to pulsing blood flow, is the major cause of motion artifact for *in vivo* thyroid spectroscopy. Comparing motion artifact reduction using respiratory gating and individual frequency/phase correction showed that it is period-3 motion that may dominate the linewidth increases associated with motion. Therefore, STEAM's increased sensitivity to period-1 motion is a minor drawback and should not influence the choice of pulse sequence.

It was shown that stronger TE and TM crushers with gradient area ratios greater than two reduce the amount of contamination in spectra *in vivo*, if the TE crushers are placed as close as possible to the second and third 90° pulses. In the case of *in vivo* MR spectroscopy of the thyroid gland, the choice of slice selection order was extremely important for eliminating spectral artifacts from unwanted coherences. The x-y-z or

y-x-z slice selection orders produced very little observable contamination artifact and were therefore chosen as optimal.

Artifacts created by eddy currents were eliminated using an eddy current correction algorithm. Respiration was a cause of line broadening for *in vivo* thyroid spectroscopy. Although the respiratory triggering method produced slightly narrower linewidths than post-correction algorithms, the effective TR of at least 4 s decreased the SNR (in a specified acquisition period) by a factor of at least two. Line broadening caused by respiratory motion was significantly reduced by automatic frequency and phase correction of individual FID's before summing, avoiding the SNR losses of respiratory gating. The new method for automatic phase correction performed very well, resolving some of the problems associated with frequency/phase correction on low SNR metabolites.

In summary, a robust method for acquiring spectra from the thyroid gland has been developed that overcomes many of the problems associated with motion, eddy currents and imperfections in the localization method. A new method of auto-phasing was developed which consisted of iteratively adjusting the phase until the peak of the real spectrum lined up in frequency with the peak in the magnitude spectrum. This worked very well on both phantom and *in vivo* experiments. Although frequency/phase correction, eddy current correction and crusher strength optimization resulted in spectral improvement from the thyroid, the identification of a slice-selection order that produced little or no contamination compared to one producing enormous phase artifacts due to contamination was by far the most important implementation.

5.6 References

1. P. C. M. van Zijl, C. T. W. Moonen, J. R. Alger, J. S. Cohen, S. A. Chesnick, High field localized proton spectroscopy in small volumes: greatly improved localization and shimming using shielded strong gradients. *Magn. Reson. Med.* **10**, 256-265 (1989).
2. C. T. W. Moonen, M. von Kienlin, P. C. M. van Zijl, J. Cohen, J. Gillen, P. Daly, G. Wolf, Comparisons of single-shot localization methods (STEAM and PRESS) for *in vivo* proton NMR spectroscopy. *NMR Biomed.* **2**, 201-208 (1989).
3. D. Ballon, M. Garwood, J. A. Koutcher, An analysis of the intrinsic resonance offset dependence of magnetization generated by stimulated echo pulse sequences for noncoupled spins. *Magn. Reson.Imag.* **9**, 569-575 (1991).
4. W. Zhang, P. Van Hecke, A spin-product-operator analysis of the dephasing requirement in STEAM-localized NMR spectroscopy. *J. Magn. Reson.* **91**, 408-412 (1991).
5. J.-M. Fauth, A. Schweiger, L. Braunschweiler, J. Forrer, R. R. Ernst, Elimination of unwanted echoes and reduction of dead time in three-pulse electron spin-echo spectroscopy. *J. Magn. Reson.* **66**, 74-85 (1986).
6. R. Kimmich, E. Rommel, A. Knüttel, Theoretical treatment of volume-selective NMR spectroscopy (VOSY) applied to coupled spin systems. *J. Magn. Reson.* **81**, 333-338 (1989).
7. P. B. Kingsley, Product operators, coherence pathways, and phase cycling. Part III: phase cycling. *Concepts Magn Reson* **7**, 167-192 (1995).
8. R. M. Dixon, J. Frahm, Localized proton MR spectroscopy of the human kidney *in vivo* by means of short echo time STEAM sequences. *Magn. Reson. Med.* **31**, 482-487 (1994).
9. G. Zhu, D. Gheorghiu, P. S. Allen, Motional degradation of metabolite signal strengths when using STEAM: a correction method. *NMR in Biomed.* **5**, 209-211 (1992).
10. R. J. Ordidge, I. D. Cresshull, The correction of transient B_0 field shifts following the application of pulsed gradients by phase correction in the time domain. *J. Magn. Reson.* **69**, 151-155 (1986).
11. T. Ernst, L. Chang, Elimination of artifacts in short echo time ^1H MR spectroscopy of the frontal lobe. *Magn. Reson. Med.* **36**, 462-468 (1996).

12. Ryner, L. N., P. Stroman, T. Wessel, D. I. Hoult, J. K. Saunders, Effect of Oscillatory Eddy Currents on MR Spectroscopy. in "Proc., ISMRM, 6th Annual Meeting, 1998," p. 1903.

13. K. F. King, A. Linz, J. Zhang, A. Ganin, Correction for Oscillatory B_0 Eddy Currents by Receive Frequency Shifting. in "Proc., ISMRM, 7th Annual Meeting, 1999," p. 744.

14. L. Friesen, Ph. D. Thesis, University of Manitoba, 1999.

Chapter 6

^{1}H MR SPECTROSCOPY OF THYROID NODULES *IN VIVO*

6.1 Introduction

Cytology of biopsies obtained through fine-needle aspiration (FNA), the standard first line diagnostic modality for thyroid nodules, is unable to discriminate benign from malignant follicular thyroid nodules, which are differentiated only by histologic evidence of capsular or vascular invasion (1). Therefore, many thyroidectomies are performed simply to exclude a diagnosis of malignancy. In the benign case, removal of the thyroid gland is usually necessarily only for diagnostic purposes. *Ex vivo* proton MRS on resected tissue as well as on FNA has been reported to accurately discriminate malignant thyroid nodules from normal tissue (1-3). The ability to localize and differentiate normal or benign tissue from their malignant counterpart with MRS *in vivo*, would provide a non-invasive and non-subjective diagnosis and may aid in the clinical management of thyroid nodules.

In vivo ^{1}H MR spectroscopy of the thyroid gland is more complex than *in vivo* MRS studies of the brain. The small size of the gland means that spectra are taken from small volumes resulting in a low signal-to-noise ratio. Fortunately, the thyroid gland lies about 2 cm below the surface of the neck and, therefore, a small surface coil rather than a volume coil can be used to maximize the SNR.

The thyroid glands location next to trachea creates a large B_0 inhomogeneity from the magnetic susceptibility differences of the tissue-air interface, causing immense linewidth

broadening. Therefore the FASTMAP autoshimming method was implemented to improve on the manual shimming method and to achieve optimal linewidths.

Respiration causes line broadening due to frequency and phase shifts from the magnetic susceptibility changes associated with the inspiration and expiration of air to the lungs. A pulse sequence can be optimized to eliminate contamination from outside the voxel by using optimal crusher strength and position as well as optimal slice selection order. Any artifacts created by motion or eddy currents are corrected using post-processing algorithms.

As discussed in Ch. 2, the thyroid gland is chemically heterogeneous (4). Therefore, in order to measure mean metabolite concentrations quantitatively over a heterogeneous tissue volume such as thyroid tumors, it is important to use a technique that receives signal uniformly over the volume of interest. Along with the high SNR associated with surface coils comes a high sensitivity to spectral contamination from the surface layer of muscle or fat. The development of the multi-ring surface coil makes it possible to obtain quantitatively accurate spectra from heterogeneous tissue as well as eliminate contamination from the surface.

Based on the work presented in the previous chapters, the ^{1}H MRS 3T method developed in this thesis to address many of the aforementioned problems is presented. The 3T results are compared to those using standard techniques at 1.5T. Finally, *in vivo* ^{1}H MR spectra from thyroid nodules are compared to spectra obtained from normal subjects, and the potential of *in vivo* ^{1}H MRS for the diagnosis of thyroid cancer is discussed.

6.2 Experimental

MR Equipment:

Experiments were performed with both a 1.5T Siemens/Magnetom SP scanner or a Bruker/Magnex 3T MSLX scanner on normal volunteers while patients with a thyroid nodule were done at 3T. On the 1.5T system, 10 mT/m gradients were used, while actively shielded, 20mT/m gradients were used on the 3T system.

RF Coil:

For 1.5T studies, the available clinical Helmholtz Neck coil and a 5-cm standard T/R surface coil were used for comparison. On the 3T system, a 5-cm standard T/R surface coil, a two-ring T/R surface coil (Ch. 3) and a three-ring T/R surface coil (Ch. 3) were used for comparison. The multi-ring surface coils were required for improved localization and decreased contamination (see Ch. 3).

Imaging:

To locate the thyroid or thyroid nodule, seven 5-mm thick axial FLASH images were taken centered with respect to the surface coil and magnet isocenter. For this, a FOV of 12 cm was used, with a TE = 7.8 ms and a TR = 170 ms. For Helmholtz neck coil studies at 1.5T, a 22 cm FOV was used.

In Vivo Spectroscopy:

The basic STEAM sequence of Fig. 5.1 was used for data collection, modified such that the refocusing lobes of the slice selection gradients were incorporated into the TE-crushers. The TE/TM crusher area ratio (A/B) was 1/3, which was accomplished with a TE-crusher 4.0 ms in length at 50% of maximum strength, and TM-crushers 12.0 ms in

length at 50% of maximum strength. The TM used in this case was 18 ms while the TE was again 20 ms. The optimum x-y-z slice selection order was used, while other orders were collected for comparison (see Ch. 5). The three 90° RF sinc pulses were 3 ms in length for a bandwidth of 2000 Hz. Voxel dimensions were varied by changing the slice-selection gradient strengths. The FID was sampled such that 4096 real and 4096 imaginary data points were collected with a 2500 Hz sweep width, resulting in a acquisition time of 1.6 s (TR = 2 s). A three-CHESS water suppression sequence was applied prior to STEAM experiments where 4 prescans (DS) and 128 individual stored acquisitions (NS) were made. The RF pulse amplitudes were calibrated manually by adjusting the 90° amplitude in STEAM to achieve maximum signal. Using the calibration factor, the amplitude of the water suppression pulses were determined. The amplitude of the third water suppression pulse was increased to achieve an optimum suppression factor. Spectra were processed by doubling the number of points in the spectra by zero filling, and then the noise was reduced by multiplying by an exponential function equivalent to 3 Hz line broadening.

Shimming:

The FASTMAP autoshimming technique, based on the STEAM sequence, was used on the 3T scanner. Data acquisition and storage were controlled with a Bruker AU program. Data were transferred to the local Unix workstation for computations with an automatic transfer program written in IDL. An IDL program was used to read the FID's (including byte swapping, zero filling, noise reduction, correction for Brukers non-sequential ADC acquisition mode, and Fourier transformation), fit the data to polynomials, calculate the shim coefficients, and subsequently determine the new SCM

settings (using the calibration data). This is described fully in Ch. 4. The new SCM settings were then transferred back to the spectrometer. Manual fine-adjustments of the linear shims were made for optimization.

Voxel Imaging:

Voxel images were found using the STEAM (TR/TE = 1000/27 ms) sequence, modified to include read and phase encoding gradients, for a 12 cm FOV, with either 256 phase encodes for a total acquisition time of 4 min. 16 s or 128 phase encodes for a total acquisition time of 2 min. 8 s.

Post-processing and Motion Correction:

Eddy current correction, as well as automatic/manual frequency and phase corrections, were done using an IDL program written by Dr. L. Friesen at the Institute for Biodiagnostics, National Research Council of Canada (5), and modified to include the automatic phase correction algorithm described previously. Depending on the SNR, the individual spectra were line broadened until the peak of interest had a SNR such that center frequency determination did not fail due to noise in the spectrum. In some cases, the SNR was too low for individual frequency and/or phase correction. The frequency and phase shifts were then stored and applied to the original FID's (see Ch. 5).

Study Population:

To obtain statistically significant results, an estimated statistical evaluation was done (Randy Summers, IBD, NRC) to determine the number of data sets required from each of the three groups: normal, benign nodule and malignant nodule. An accurate estimate of the required study population size requires prior knowledge of the *in vivo* diagnostic parameters. As these parameters could not be known prior to the study, based on the

previous *ex vivo* studies, it was estimated that at least 15-20 spectra per group would be needed.

Over a ten-month period, a total of five patients with a thyroid nodule were recruited. All five of these were cases where histological evaluation of fine-needle aspirates was indeterminate, and therefore suspicious of malignancy.

6.3 Results and Discussion

6.3.1 In Vivo ^{1}H MR Spectroscopy of the Thyroid Gland at 1.5T

The benefit of using a volume coil such as the Helmholtz neck coil is that, from an imaging standpoint, the entire neck is visible and the thyroid is easily recognizable relative to other well-known structures. A ^{1}H MR image of a subject presenting with a cystic mass in the left thyroid, collected using the volume neck coil, is shown on the left of Fig. 6.1. The volume neck coil allows full inspection of all anatomical details. Within the nodule there appears to be a difference in the intensity of the MR signal, likely due to the presence of fat or water. Since cysts are fluid-filled, there is a high concentration of water with different T_1 and T_2 compared to the surrounding normal thyroid tissue, giving rise to the different contrast in the image.

A ^{1}H MR image of a normal subject thyroid collected with a 5-cm standard surface coil is shown on the right in Fig. 6.1. Although the surface coil is not sensitive to deep lying tissue, it does adequately visualize the thyroid gland and surrounding trachea, muscle, fat, carotid artery and jugular vein. Ghosting in the image is due to blood flow in the artery and vein which, due to their position relative to the thyroid, do not affect the

ability to recognize the thyroid gland. Alternatively, the phase encoding direction could be chosen in the x-direction, or flow-compensating bipolar gradients could be used.

Figure 6.1 FLASH images at 1.5T, with a Helmholtz neck coil (left) and a 5-cm surface coil (right). Subject on the left had a cystic thyroid nodule in the left lobe of the thyroid gland.

^{1}H MR spectra from voxels placed within the cyst and thyroid, corresponding to the images in Fig. 6.1, are shown in Fig. 6.2. Figure 6.2a represents the best quality spectrum obtained from ten normal subjects studied at 1.5T using a volume coil. The spectrum obtained with the volume coil has very poor SNR due to the low sensitivity of the coil. Combined with the large spectral linewidths expected for *in vivo* thyroid studies, the low SNR results in a poor quality spectrum with little diagnostic capability. Figure 6.2b represents the best quality spectrum obtained from ten normal subjects studied at 1.5T using a standard 5-cm surface coil. Although the SNR of this spectrum is reasonable, the metabolite peaks are situated on the broad shoulder of the residual water resonance due to the poor water suppression associated with a surface coil.

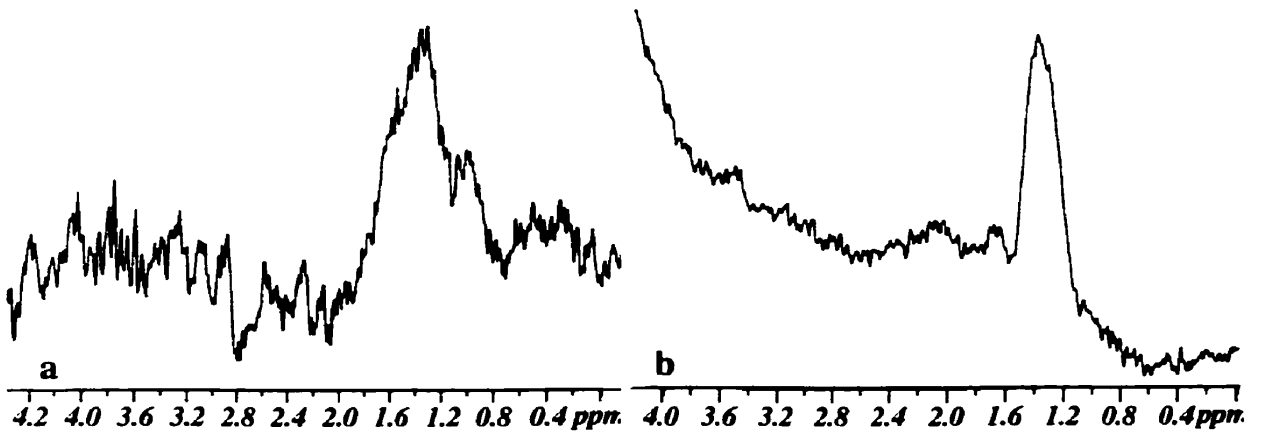

Figure 6.2 *In vivo* ^{1}H MR spectra at 1.5T from (a) a cystic thyroid nodule using a Helmholtz neck coil (see Fig. 6.1, left) and (b) a normal thyroid gland using a 5-cm standard surface coil (see Fig. 6.1, right).

The poor SNR and resolution of the spectra obtained at 1.5T suggested that *in vivo* MRS at 1.5T for the study of thyroid nodules was not going to be useful for diagnosis. To improve the inherent resolution and SNR of ^{1}H MR spectra, improvements in technique and an increase in magnetic field strength were indicated.

6.3.2 *In Vivo* ^{1}H MR Spectroscopy of the Thyroid Gland at 3T

In addition to the SNR and resolution advantages of a 3T system, the development of the multi-ring surface coil and implementation of the FASTMAP autoshimming technique further improved the 3T method over the 1.5T method.

For *in vivo* spectroscopy near the surface of the body where a layer of fat often resides, lipid contamination of localized spectra is often unavoidable (6). The multi-ring surface coil not only improves the B_1-homogeneity over the VOI, as compared to the standard single-ring surface coil, leading to volume coil-style voxel profiles, but also adds the possibility of reduced contamination from the surface of the sample. The

reduced sensitivity to signals located near the surface of the coil/sample is due to the B_1-nulling effect near the surface of the coil. The two multi-ring surface coils used in thyroid studies have slightly different B_1 responses. The two-ring surface coil was not designed specifically for B_1-nulling at the surface, and therefore its nulling point extends into the sample, leaving some sensitivity to surface contamination similar to that of a standard surface coil. This can be seen in the low flip angle FLASH image in Fig. 6.3 (left) from a normal subject. Notice that as the second ring (responsible for the nulling effect) is only 2.5 cm in diameter, the nulling region is somewhat limited. The three-ring surface coil was designed not only for uniform sensitivity across the voxel but also for near-zero B_1 exactly at the surface over a larger area than the two-ring surface coil. This is easily seen in the image on the right of Fig. 6.3.

Figure 6.3 Axial FLASH image at 3T from the thyroid gland of a normal subject using the two-ring surface coil (left) and the three-ring surface coil (right).

It should be pointed out that the placement of the multi-ring surface coil is very important. The sensitivity to surface tissue contamination is dependent on B_1 magnitude and on the position of the slice selection planes. With respect to the B_1 field strength at the voxel location, the B_1 at the surface of the coil on either side of the null field near the

conductor of the largest ring is larger than that of a standard surface coil. Therefore, the coil should be placed such that at least two of the three slice selection planes pass through the B_1-nulled region, and the area of B_1-nulling should extend beyond the edge of the slice. That is, the B_1-nulling area should be larger than the maximum slice thickness required. The B_1-nulling region of the three-ring surface coil is well suited for the purposes of this study, whereas the smaller B_1-nulling region of the two-ring coil is limited to smaller voxel sizes and the coil position relative to the slice selection planes is more critical.

Using the methods developed in this thesis at 3T, and with proper placement of the multi-ring surface coil, excellent quality *in vivo* ^{1}H MRS spectra were obtained from the thyroid gland of healthy volunteers. Five examples of "normal" spectra are shown in Fig. 6.4.

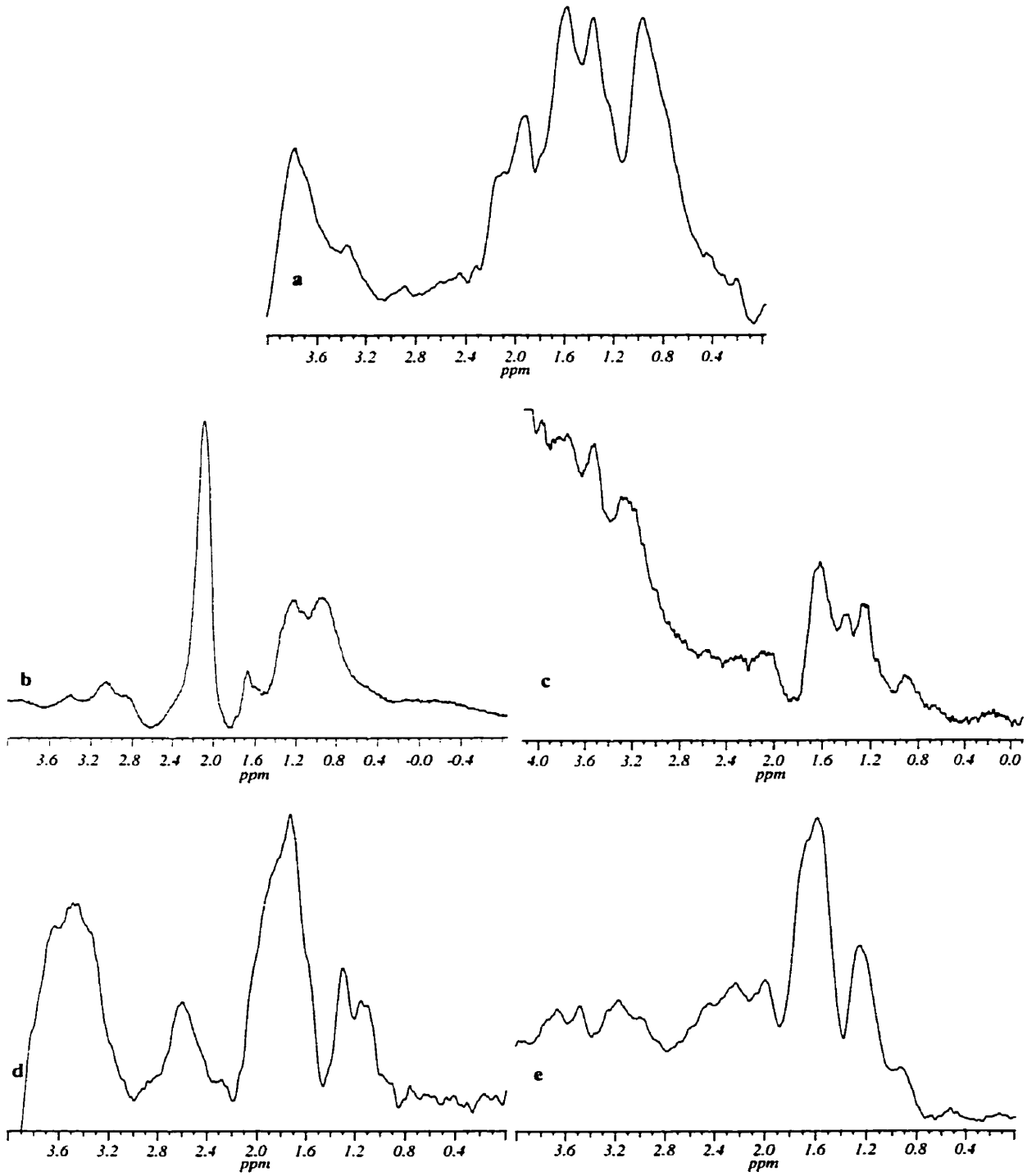

Figure 6.4 Water suppressed ^{1}H MR spectra at 3T from the thyroid gland of five normal subjects (DS = 4, NS = 128). There is no evidence of contamination in these spectra or corresponding voxel images. (a), (b), (d), and (e) were obtained with the three-ring surface coil, and (c) with the two-ring surface coil.

Notice that the water suppression in the spectrum obtained with the two-ring surface coil (Fig. 6.4c) is not as good as that obtained with the three-ring surface coil (Fig. 6.4a,b,d,e), in part due to the slightly degraded B_1-homogeneity.

Looking at these spectra more closely, one notices good resolution of the metabolite peaks at 0.9 ppm, 1.3 ppm, 1.7 ppm, and 2.0 ppm, with additional resonaces in the 2.2-2.5 ppm region where glutamine resonaces are found and the 2.8-4.0 regions where choline and creatine metabolites are found. The resolution and SNR of these spectra resemble those obtained *ex vivo* on thyroid biopsies at 8.5T. With only five subjects, an attempt to group these normal spectra is not justified. Despite this, if the criteria used for classification of the *ex vivo* spectra discussed in Ch.2 are applied to these *in vivo* spectra obtained from normal volunteers, all would be classified as "normal". This suggests that *in vivo* spectroscopy using the 3T method described in this thesis shows excellent diagnostic potential.

6.3.3 *In Vivo* ^{1}H MR Spectroscopy of Thyroid Nodules at 3T

With the methods in place to produce high quality *in vivo* spectra from the thyroid gland of healthy subjects, patients with thyroid nodules were recruited for comparison. A total of five patients participated in this on-going research protocol. Additional unexpected difficulties arose, and therefore only a few spectra of acceptable quality were obtained.

CASE 1:

The first patient presented with a 1.5-cm left thyroid nodule located very close to the surface of the neck. This study was performed using the three-ring surface coil. An axial FLASH image is shown in Fig. 6.5, with an image of the selected VOI shown on the right. It is clear that the coil should have been moved off the surface of the patient since the region of optimum homogeneity appears to be peaked slightly further from the surface than the center of the tumor. A signal-free fine-needle biopsy track is also visible in both the FLASH and voxel images, extending in the y-direction (vertically in the image). A thin layer of fat is seen at the anterior surface of the neck, but no contamination was visible in the voxel image.

Figure 6.5 Axial FLASH image from patient #1, with the three-ring surface coil (left) and corresponding image of the localized VOI (right). Notice the superficial nature of this nodule and the dark track left behind from the fine-needle biopsy.

Unfortunately the resulting ^{1}H MR spectrum has a large contamination artifact (Fig. 6.6), seen as an irregular-shaped baseline. The source of this artifact is likely due to

the extreme close proximity of the VOI to the surface and/or a susceptibility artifact created by the biopsy track.

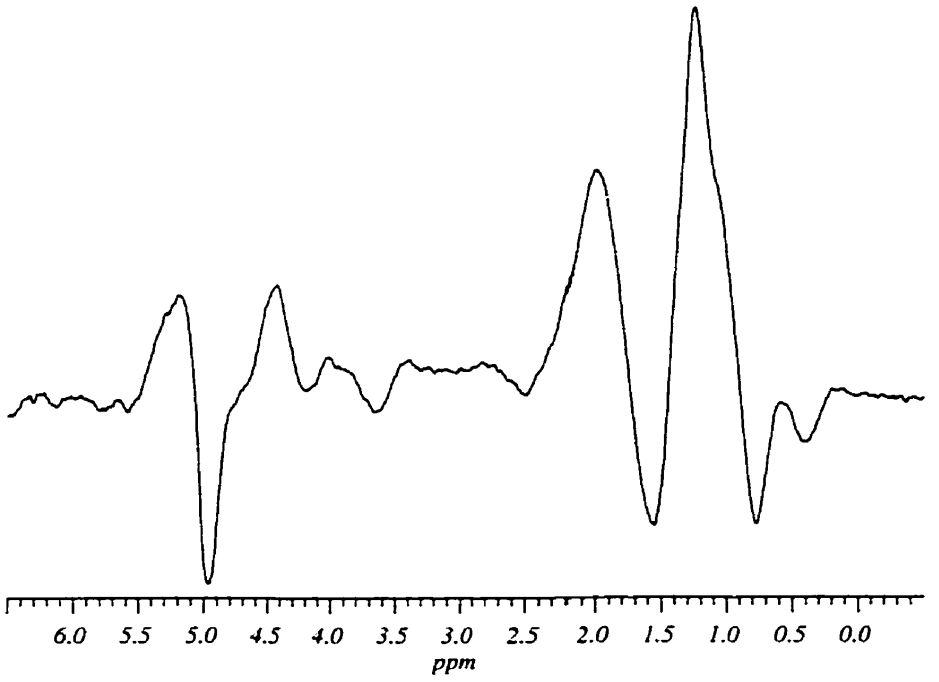

Figure 6.6 *In vivo* ^{1}H MR spectrum obtained from patient #1, using the three-ring surface coil.

Pathological Diagnosis:

Follicular adenoma in the left lobe of the thyroid gland, consisting of well differentiated follicular cells showing Hurthle cell metaplasia.

CASE 2:

The second patient presented with a 1.5-cm right thyroid nodule. Prior clinical palpation revealed that the nodule was small, so the study was performed using the two-ring surface coil for improved SNR characteristics. An axial FLASH image is shown in

Fig. 6.7, with an image of the selected VOI shown to the right. Direct evidence of lipid contamination resulting from subcutaneous fat was seen in the voxel image.

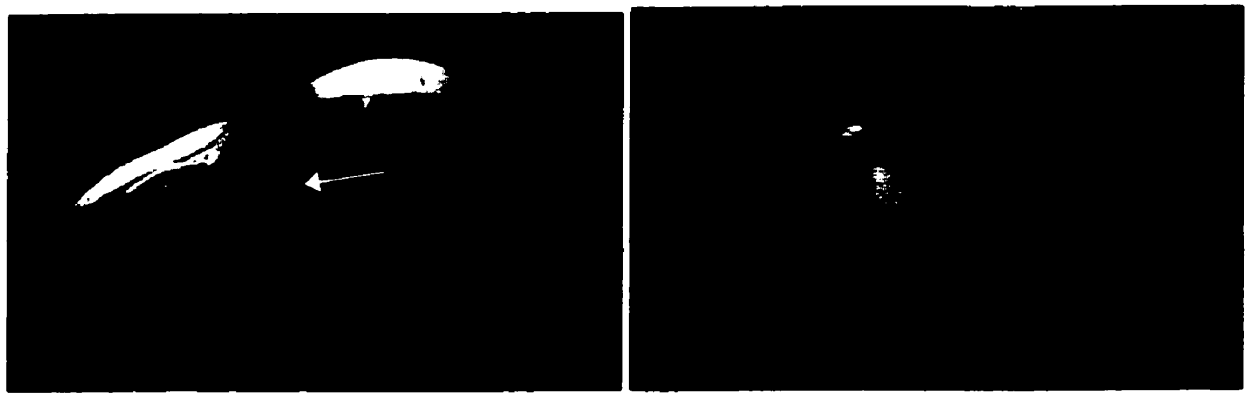

Figure 6.7 Axial FLASH image from patient #2, using the two-ring surface coil (left) and corresponding image of the localized VOI (right) from a 1.5 cm^3 voxel (1.0 cm x 1.0 cm x 1.5 cm) . Notice the fat signal appearing at the surface due to improper placement of the coil.

This contamination artifact may have been avoided if the coil had been placed further to the patient's right (left on image). Even better, use of the three-ring surface coil would have eliminated the contamination without such strict dependence on coil placement.

The resulting ^1H MR spectrum (Fig. 6.8) shows a large lipid resonance, likely due to contamination from the surface layer of fat seen in Fig. 6.7. Therefore, although this spectrum does look different from the "normal" spectra of the previous section, it cannot be considered reliable for a classification study.

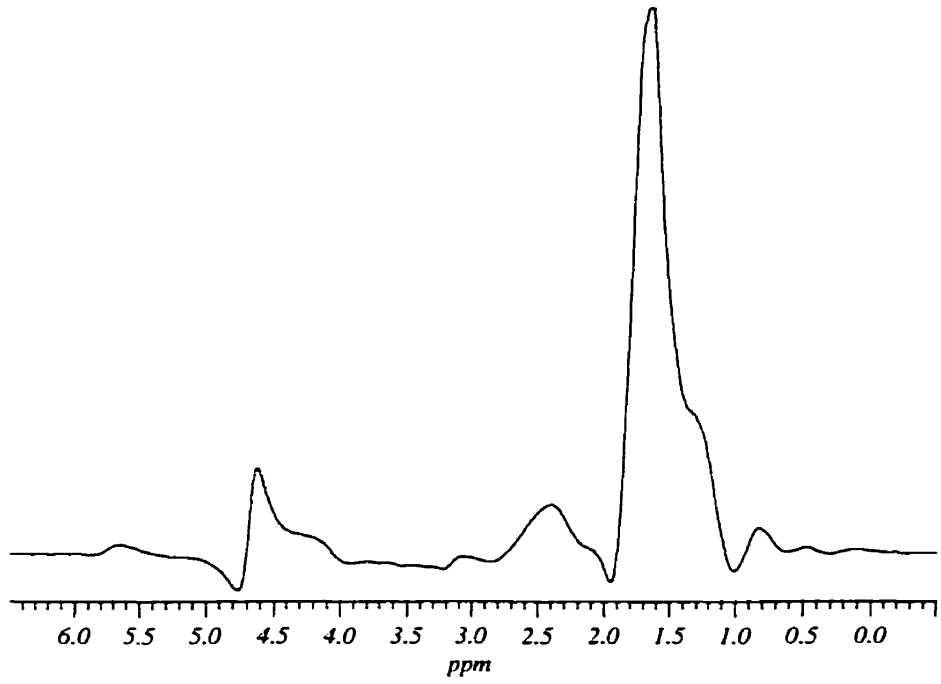

Figure 6.8 *In vivo* ^{1}H MR spectrum obtained from patient #2, using the two-ring surface coil.

Pathological Diagnosis:

Follicular carcinoma, microinvasive type, with associated mild Hashimoto's thyroiditis.

CASE 3:

The third patient was a female of approximately 200 lbs. Despite several efforts at imaging this patient, motion artifacts made it impossible to locate the thyroid nodule and, therefore, the spectrum obtained was not useful. An axial FLASH image, obtained on the third attempt after urging the patient not to move during the acquisition, is shown in Fig. 6.9.

Figure 6.9 Axial FLASH image from patient #3. Motion blurring does not allow identification of the nodule.

Pathological Diagnosis:

Thyroid (total thyroidectomy specimen)
- Papillary carcinoma of thyroid in right lobe
- Tumor extending into adjacent isthmus and adjacent fat
- Nodular (adenomatous) goitre in thyroid tissue generally
- Mild chronic thyroiditis.

No tumor found in resected lymph nodes (paratracheal, Delphian, pretracheal).
No tumor found in left upper and right upper parathyroid glands.

CASE 4:

The fourth patient presented with a large (2.0 to 2.5 cm) right thyroid nodule. This study was performed using the three-ring surface coil. An axial FLASH image is shown in Fig. 6.10, and the corresponding ^{1}H MR spectrum is shown in Fig. 6.11. A thin layer of subcutaneous fat is seen, but no contamination is visible in the spectrum. Notice from the structure within the nodule that there seems to be a distinct border between where the typical normal thyroid would exist and the additional tissue creating the enlarged nodule.

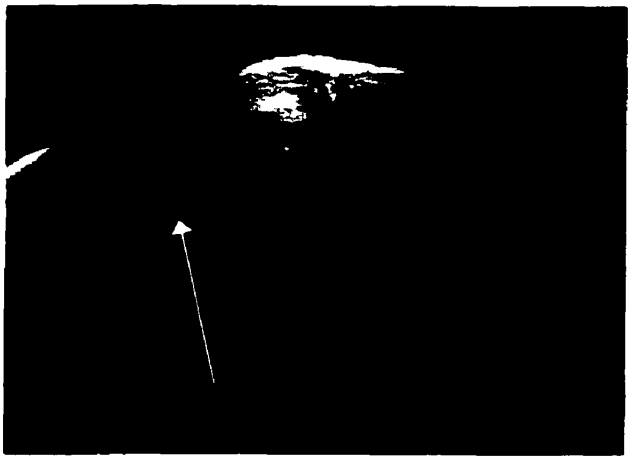

Figure 6.10 Axial FLASH image from patient #4, using the three-ring surface coil. Notice that the B_1-nulling region of the three-ring surface coil does not allow lipid signal from the surface to contaminate the spectrum (Fig. 6.11).

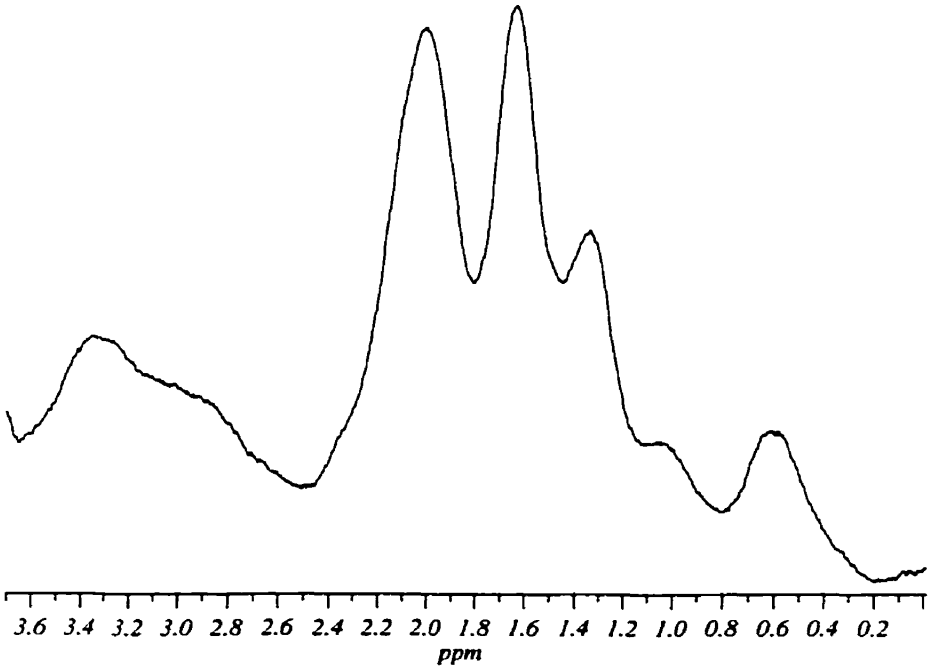

Figure 6.11 *In vivo* ^{1}H MR spectrum obtained from patient #4, using the three-ring surface coil, from a 3.8 cm^3 voxel (1.5 cm x 1.5 cm x 1.7cm) centered within the nodule.

The spectrum obtained from this nodule had excellent SNR and resolution, comparable to those obtained *ex vivo* on thyroid biopsies at 8.5T, and therefore also shows excellent classification potential. Looking at this spectrum more closely, the metabolite peak height ratios at both 1.7 ppm and 2.0 ppm to the 0.9 ppm peak height are greater than 1.1 and 1.12 respectively (see Section 2.5), which would classify this spectrum as a "normal".

Pathological Diagnosis:

Nodular goitre in specimens from right and left lobe. Focal areas in the thyroid gland showing changes consistent with Hashimoto's thyroiditis.

CASE 5:

The fifth patient presented with two right thyroid nodules, 2.5-cm and 1.2 cm in diameter. This study was performed using the three-ring surface coil. Again, considerable structure can be seen in the axial FLASH image of Fig. 6.12, and in this case, two nodules are present in the right thyroid gland. The corresponding ^{1}H MR spectrum, with the 2.7 cm^3 voxel placed such that it contained most of both nodules, is shown in Fig. 6.13. Again, no contamination is visible in the spectrum, even though a thin layer of subcutaneous fat is seen.

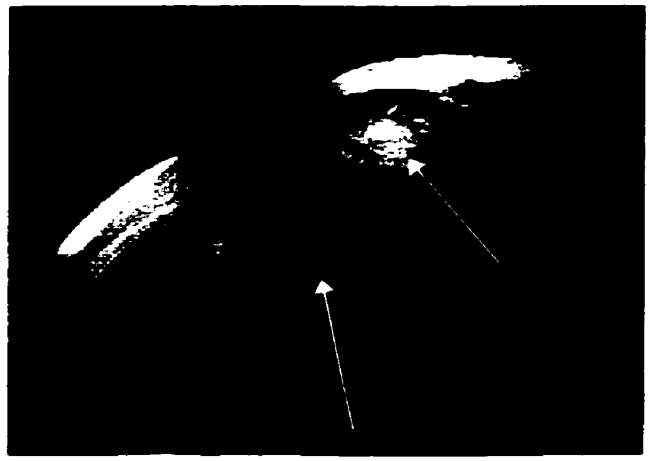

Figure 6.12 Axial FLASH image from patient #5, using the three-ring surface coil. In this case, the patient has two nodules both in the right thyroid.

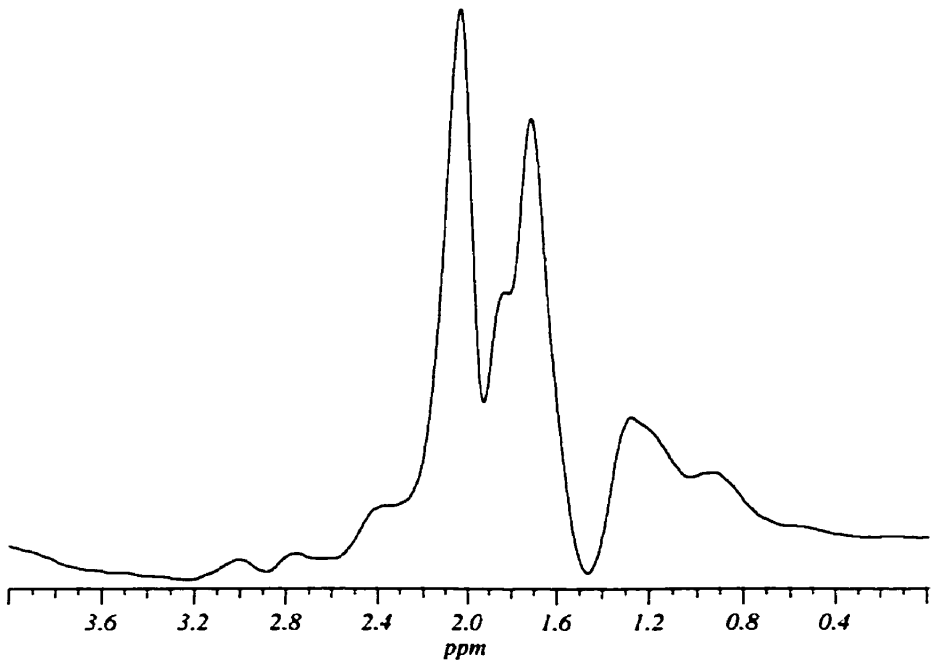

Figure 6.13 *In vivo* ^{1}H MR spectrum obtained from patient #5, using the three-ring surface coil, from a 2.7 cm^3 voxel (1.0 cm x 1.8 cm x 1.5 cm).

The spectrum obtained from this nodule again had excellent SNR and resolution, comparable to those obtained *ex vivo* on thyroid biopsies at 8.5T, and therefore also shows excellent classification potential. The metabolite peak height ratios at both 1.7 ppm and 2.0 ppm to the 0.9 ppm peak height is greater than 1.1 and 1.12 respectively (see Section 2.5), which would classify this spectrum as a "normal".

Pathological Diagnosis:

Adenomatoid goitre with two dominant atypical (microfollicular and trabecular) nodules, right lobe of thyroid gland.

6.4 Conclusions

A method has been developed for producing high quality ^{1}H MR spectra of thyroid tumors *in vivo*.

Imaging using FLASH was fast and produced images with adequate SNR and contrast to differentiate both normal and neoplastic thyroid tissue from the surrounding muscle. Although there was ghosting from blood flow in the carotid artery and jugular veins, it did not hinder the ability to locate the thyroid/nodule.

The spectra obtained at 1.5T had poor SNR, resolution and/or water suppression. It was concluded, therefore, that the quality of ^{1}H MR spectra of the thyroid at 1.5T would not allow for classification of thyroid spectra *in vivo*.

Considerable improvement in SNR and resolution was apparent at 3T compared to 1.5T. Optimizing the slice-selection order as well as automatic localized shimming and frequency/phase correction were necessary for achieving optimal spectral resolution. Using increased spoiler gradients with a large difference between TE and TM gradient areas minimized the amount of contamination present in the spectra from unwanted coherences. Imaging of the selected VOI not only confirmed the placement of the voxel with respect to the tissue of interest but also identified possible surface lipid contamination.

The combined use of STEAM localization and a multi-ring surface coil offered the SNR advantages of a surface coil with homogeneous volume localization, comparable to volume coils. With optimized multi-ring surface-coil design and placement, there was reduced sensitivity to lipid contamination from a subcutaneous layer of fat in the anterior

neck. Together, these characteristics of multi-ring surface coils allowed high quality spectra of excellent resolution to be obtained.

In vivo ^{1}H MR spectra from normal thyroid at 3T had characteristics similar to those of *ex vivo* biopsy spectra at 8.5T. Specifically, if the criteria used for classification of the *ex vivo* spectra discussed in Ch.2 are applied to these *in vivo* spectra obtained from normal volunteers, all would have been classified as "normal". Unfortunately, of the five patients with thyroid nodules that participated in the study, only two produced acceptable spectral results, both having a benign pathological diagnosis. However, for both of these benign cases, the 1.7ppm/0.9ppm and the 2.0ppm/0.9ppm metabolite peak height ratios were greater that 1.1 and 1.12, respectively, which would classify them as "normal" if the same diagnostic parameters determined from the *ex vivo* classification results were used. Therefore, the ^{1}H MR spectra obtained from normal thyroid and thyroid nodules confirm that there is potential for classification of thyroid tumors *in vivo* using these 3T methods.

Future work will involve collecting more spectra from thyroid nodules, particularly malignant nodules, so that *in vivo* diagnostic parameters can be determined and classification accuracy tested. Further studies should also include studies with patients having other conditions, which frequently coexist, such as Hashimoto's thyroiditis, hypothyroidism and cystic degeneration.

6.5 References

1. P. Russell, C. L. Lean, L. Delbridge, G. L. May, S. Dowd, C. E. Mountford, Proton magnetic resonance and human thyroid neoplasia I: discrimination between benign and malignant neoplasms. *Am. J. Med.* **96**, 383-388 (1994).
2. L. Delbridge, C. L. Lean, P. Russell, G. L. May, S. Roman, S. Dowd, T. S. Reeve, C. E. Mountford, Proton magnetic resonance and human thyroid neoplasia II: potential avoidance of surgery for benign follicular neoplasms. *World J. Surg.* **18**, 512-517 (1994).
3. R. L. Somorjai, A. E. Nikulin, N. Pizzi, D. Jackson, G. Scarth, B. Dolenko, H. Gordon, P. Russell, C. L. Lean, L. Delbridge, C. E. Mountford, I. C. P. Smith, Computerized consensus diagnosis: a classification strategy for robust analysis of MR spectra. I. Application to ^{1}H spectra of thyroid neoplasms. *Magn. Reson. Med.* **33**, 257-263 (1995).
4. A. Rutter, B. Künnecke, S. Dowd, P. Russell, L. Delbridge, C. E. Mountford, Proton magnetic resonance and human thyroid neoplasia III. Ex vivo chemical-shift microimaging. *J. Magn. Reson., Series B* **110**, 240-248 (1996).
5. L. Friesen, Ph. D. Thesis, University of Manitoba, 1999.
6. D. C. Shunghu, J. D. Glickson, Band-selective spin echoes for *in vivo* localized ^{1}H NMR spectroscopy. *Magn. Reson. Med.* **32**, 277-284 (1994).

APPENDIX I

PRO b0_shim,fov,read_size,tau,x0,y0,z0,data_dir,xy0file,order,bar_length,sw,kk, PSPLOT = psplot

This IDL program reads the 12 FASTMAP projection data and calculates the phase difference after byte-order swapping and correcting for $\pm\pi$ phase jumps. The B0-field distribution is determined by fitting the data to an nth order polynomial (n=order, chosen in the command line).
Inputs are: the FOV used, the number of points collected per projection, the delay time used in the 2nd run through of the FASTMAP sequence, the position of the voxel, the data directory, the first experiment number, the degree of the polynomial fit, the initial bar length, sw related to the amount of noise reduction (typically 60), and an output variable kk
The program will ask for six different bar lengths to do the polynomial fitting

```
;Example input line:  b0_shim,20.0,256,5.0e-3,0.90,0.39,-0.1,'S13-95-26.NQ1','5',2,4.0,60

print, 'Shimming to order ',order
common plot_index, count, plot_num

print,"Enter new Bar_Length (cm) for Projections #1-#6."
read, bar1
read, bar2
read, bar3
read, bar4
read, bar5
read, bar6

count = 1
; plot_num = 0 - 5 to plot only one projection
; plot_num = 99 to print all 6 projections

;plot_num = 4
plot_num = 99

if (plot_num eq 99) then !P.MULTI = [0,3,6,0,0] $
else !P.MULTI = [0,3,1,0,0]
!P.MULTI = [0,2,6,0,0]

;xy = Cor_sag_ob: Slice angle = 135 degrees
;yx = Cor_sag_ob: Slice angle = 45 degrees
;xz = Trans_sag_ob: Slice angle = 135 degrees
;zx = Trans_sag_ob: Slice angle = 45 degrees
;zy = Trans_cor_ob: Slice angle = 135 degrees
;yz = Trans_cor_ob: Slice angle = 45 degrees

xyTfile = xy0file +1
yx0file = xy0file +2
yxTfile = xy0file +3
xz0file = xy0file +4
xzTfile = xy0file +5
zx0file = xy0file +6
zxTfile = xy0file +7
zy0file = xy0file +8
zyTfile = xy0file +9
yz0file = xy0file +10
yzTfile = xy0file +11

;output into shims_f.sbk in following order
;shim_name(0) = x
;shim_name(1) = y
```

```
;shim_name(2) = z
;shim_name(3) = 2xy
;shim_name(4) = xz
;shim_name(5) = yz
;shim_name(6) = x2-y2
;shim_name(7) = z2
;shim_name(8) = z2x
;shim_name(9) = z2y
;shim_name(10) = 2zxy
;shim_name(11) = z3

;********************** for printing to postscript ****************************

; save current device
                    prev_plot = !D.NAME
                    prev_multi = !P.multi
if KEYWORD_SET(psplot) then begin
   set_plot, 'ps'
   device, /ENCAPSUL, filename = 'b0shim.eps', XSIZE = 15.25 ,YSIZE = 21.2725
   endif else begin
     set_plot, prev_plot
     ;window, 7, XSIZE = 800, YSIZE = 800, Title = 'Phase Diff vs r (cm)'
      window, 7, XSIZE = 550, YSIZE = 450, Title = 'Phase Diff vs r (cm)'
   endelse

aa = make_array(6,4, /float)
;
; Read xy projections for both Tau=0 and Tau=?? msec
;
title1 = "Projection #1 - XY"
read_data,data_dir,xy0file,fov,bar_length,256,read_size,fspace_xy0,sw
read_data,data_dir,xyTfile,fov,bar_length,256,read_size,fspace_xyT,sw
;
; Determine xy coefficients
;
t=0
b0_fit,t,title1,bar1,fov,read_size,fspace_xy0,fspace_xyT,a0_xy,a1_xy,a2_xy,a3_xy,order
aa(t,0) = a0_xy
aa(t,1) = a1_xy
aa(t,2) = a2_xy
aa(t,3) = a3_xy
;
; Read yx projections for both Tau=0 and Tau=?? msec
;
title1 = "Projection #2 - YX"
read_data,data_dir,yx0file,fov,bar_length,256,read_size,fspace_yx0,sw
fspace_yx0=reverse(fspace_yx0)
read_data,data_dir,yxTfile,fov,bar_length,256,read_size,fspace_yxT,sw
fspace_yxT=reverse(fspace_yxT)
;
; Determine yx coefficients
;
t=1
b0_fit,t,title1,bar2,fov,read_size,fspace_yx0,fspace_yxT,a0_yx,a1_yx,a2_yx,a3_yx,order
aa(t,0) = a0_yx
aa(t,1) = a1_yx
aa(t,2) = a2_yx
aa(t,3) = a3_yx
;
; Read xz projections for both Tau=0 and Tau=?? msec
;
title1 = "Projection #3 - XZ"
```

```
read_data,data_dir,xz0file,fov,bar_length,256,read_size,fspace_xz0,sw
fspace_xz0=reverse(fspace_xz0)
read_data,data_dir,xzTfile,fov,bar_length,256,read_size,fspace_xzT,sw
fspace_xzT=reverse(fspace_xzT)
;
; Determine xz coefficients
;
t=2
b0_fit,t,title1,bar3,fov,read_size,fspace_xz0,fspace_xzT,a0_xz,a1_xz,a2_xz,a3_xz,order
aa(t,0) = a0_xz
aa(t,1) = a1_xz
aa(t,2) = a2_xz
aa(t,3) = a3_xz
;
; Read zx projections for both Tau=0 and Tau=?? msec
;
title1 = "Projection #4 - ZX"
read_data,data_dir,zx0file,fov,bar_length,256,read_size,fspace_zx0,sw
read_data,data_dir,zxTfile,fov,bar_length,256,read_size,fspace_zxT,sw
;
; Determine zx coefficients
;
t=3
b0_fit,t,title1,bar4,fov,read_size,fspace_zx0,fspace_zxT,a0_zx,a1_zx,a2_zx,a3_zx,order
aa(t,0) = a0_zx
aa(t,1) = a1_zx
aa(t,2) = a2_zx
aa(t,3) = a3_zx
;
; Read yz projections for both Tau=0 and Tau=?? msec
;
title1 = "Projection #5 - YZ"
read_data,data_dir,yz0file,fov,bar_length,256,read_size,fspace_yz0,sw
read_data,data_dir,yzTfile,fov,bar_length,256,read_size,fspace_yzT,sw
;
; Determine yz coefficients
;
t=4
b0_fit,t,title1,bar5,fov,read_size,fspace_yz0,fspace_yzT,a0_yz,a1_yz,a2_yz,a3_yz,order
aa(t,0) = a0_yz
aa(t,1) = a1_yz
aa(t,2) = a2_yz
aa(t,3) = a3_yz
;
; Read zy projections for both Tau=0 and Tau=?? msec
;
title1 = "Projection #6 - ZY"
read_data,data_dir,zy0file,fov,bar_length,256,read_size,fspace_zy0,sw
fspace_zy0=reverse(fspace_zy0)
read_data,data_dir,zyTfile,fov,bar_length,256,read_size,fspace_zyT,sw
fspace_zyT=reverse(fspace_zyT)
;
; Determine zy coefficients
;
t=5
b0_fit,t,title1,bar6,fov,read_size,fspace_zy0,fspace_zyT,a0_zy,a1_zy,a2_zy,a3_zy,order
aa(t,0) = a0_zy
aa(t,1) = a1_zy
aa(t,2) = a2_zy
aa(t,3) = a3_zy

;********** end postcript plotting **********
```

```
if keyword_set(psplot) then begin
                device, /close_file
endif
set_plot, prev_plot
!p.multi = prev_multi
;
; Determine Associated Spherical Harmonic Coefficients, k(n,i)
; k11 -> X shim or r*sin(theta)*cos(phi)
; k12 -> Y shim or r*sin(theta)*sin(phi)
; k13 -> Z shim or r*cos(theta)
; k21 -> Z^2 shim or r^2(3cos^2(theta)-1)/2
; k22 -> ZX shim or r^2*sin(theta)*cos(theta)*cos(phi)
; k23 -> ZY shim or r^2*sin(theta)*cos(theta)*sin(phi)
; k24 -> X^2-Y^2 shim or r^2*sin^2(theta)*cos(2*phi)
; k25 -> 2XY shim or r^2*sin^2(theta)*sin(2*phi)

;conv = 1/(2.0*!pi*Tau)              ;in Hz/cm^n
conv = 1/(2.0*!pi*Tau*127.76)       ;in ppm/cm^n
r8 = sqrt(8.0)
k = fltarr(8)
;print,'conv = ',conv

k11 = conv*(a1_xy - a1_yx - a1_xz + a1_zx)/r8
k12 = conv*(-a1_xy - a1_yx + a1_yz - a1_zy)/r8
k13 = conv*(a1_xz + a1_zx + a1_yz + a1_zy)/r8
k21 = conv*( -2.0*a2_xy -2.0*a2_yx + a2_xz + a2_zx + a2_yz + a2_zy)/3.0
k22 = conv*(-a2_xz + a2_zx)
k23 = conv*(a2_yz - a2_zy)
k24 = conv*(a2_xz + a2_zx - a2_yz - a2_zy)/2.0
k25 = conv*(-a2_xy + a2_yx)/2.0
;
; Correct for displacement of voxel
;
k11 = k11 + (-k21*x0 + k22*z0 + k24*2.0*x0 + k25*2.0*y0)
k12 = k12 + (-k21*y0 + k23*z0 - k24*2.0*y0 + k25*2.0*x0)
k13 = k13 + (k21*2.0*z0 + k22*x0 + k23*y0)

k(0)= k11
k(1)= k12
k(2)= k13
k(3)= k25
k(4)= k22
k(5)= k23
k(6)= k24
k(7)= k21

;
; prepare q and sigma for calculation of actual shim values using re_shim.pro
; the shim corrections needed, k(ppm/cm^n), are converted to Gauss/cm^n and
; reordered to be the same as re_shim.pro wants
; zero is put into shims not calculated with b0_fit
;
gyro = 42.5749e6            ;Hz/Tesla
gyro_gauss = gyro/1e4               ;in Hz/Gauss since 10^4 Gauss = 1Tesla
;kk = (k*127.76)/gyro_gauss         ;in Gauss/cm^n
kk = k                              ;in ppm/cm^n
sigma = make_array(12, /float)
sigma(*) = 0.0
q = make_array(12, /float)
re_shim_order = [0,1,2,3,4,5,6,7,-1,-1,-1,-1]

for i = 0, 11 do begin
```

```
if (re_shim_order(i) lt 0) then q(i)=0.0
j = re_shim_order(i)  &  if (j ge 0) then q(j) = kk(i)
endfor
re_shims, 'shims_i.sbk', 'shims_f.sbk', A, Aerr, q, sigma, Set,Err,check_lim, flag

END

;;;;;;;;;;;;;;;;;;;;;;;;;;;;;;;;;;;;;;;;;;;;;;;;;;;;;;;;;;;;;;;;;;;;;;;;;;

PRO b0_fit,t,title1,bar_length,fov,read_size,fspace1,fspace2,a0,a1,a2,a3,order

common plot_index, count, plot_num

res = fov/read_size
bar_pts = ROUND(bar_length/res)             ;nearest integer
bar_length = bar_pts*res
r = res*(findgen(bar_pts) - float(bar_pts/2))
roi1 = make_array(bar_pts, /complex)
roi2 = make_array(bar_pts, /complex)
phase_diff = make_array(bar_pts, /float)

for i = 0, bar_pts-1 do begin
    roi1(i) = fspace1(read_size/2-bar_pts/2+i)
    roi2(i) = fspace2(read_size/2-bar_pts/2+i)
endfor

if (count eq plot_num) then begin
            plot, r, abs(roi1),xrange=[MIN(r),MAX(r)], color = 0, background =255, $
            XCHARSIZE = 1.2, YCHARSIZE = 1.2, CHARTHICK = 1.2, $
            xstyle=1,ystyle=2,xtitle = 'Distance (cm)', ytitle = 'Relative Signal', $
            THICK = 1.2, XTHICK=1.2, YTHICK =1.2, $
            YTICKLEN=0.02, XTICKLEN=0.04, $
            title=title1

endif else $
if (plot_num eq 99) then begin
            plot, r, abs(roi1)/MAX(abs(roi1)),xrange=[MIN(r),MAX(r)], color = 0, background =255, $
            XCHARSIZE = 1.2, YCHARSIZE = 1.2, CHARTHICK = 1.2, $
            xstyle=1,ystyle=2,xtitle = 'Distance (cm)', ytitle = 'Relative Signal', $
            THICK = 1.2, XTHICK=1.2, YTHICK =1.2, $
            YTICKLEN=0.02, XTICKLEN=0.04, $
            title=title1

endif

;B0 is proportional to the phase difference of two projections with diff. Tau
; phase difference is equivalent to the phase obtained by complex division
; (x1+j*y1)/(x2+j*y2) = a1*exp(j*phi1)/a2*exp(j*phi2) =
; (a1/a2)*exp(j*(phi1-phi2)

phase_diff = atan(roi2/roi1)

; do phase unwrapping
unwrap,phase_diff,phase_map
;
;weighting for SNR
;
w = fltarr(bar_pts)
wtemp = fltarr(bar_pts)
; weight according to SNR
temp1=(abs(roi1)/abs(roi1(bar_pts/2)))^2
temp2=(abs(roi2)/abs(roi2(bar_pts/2)))^2
```

```
wtemp(*) = temp1
w(*) = wtemp
izero1 = 9999
izero2 = -1
for i =  bar_pts-1, bar_pts/2, -1 do begin
        if (w(i) le 0.01) then izero1 = i
endfor
for i =  0, bar_pts/2-1 do begin
        if (w(i) le 0.01) then izero2 = i
endfor

for i = 0, bar_pts-1 do begin
        if (i le izero2) then w(i) = 0
        if (i ge izero1) then w(i) = 0
endfor

poly_fit = POLYFITW(r,phase_map,w,order,yfit,yband,sigma)

;do polynomial fit
a0 = poly_fit(0)
a1 = poly_fit(1)
if (order eq 1) then a2 = 0.0
if (order ge 2) then a2 = poly_fit(2)
if (order ge 3) then a3 = poly_fit(3) else a3 = 0

if (count eq plot_num) then begin
        plot, r,phase_map,xrange=[MIN(r),MAX(r)], color = 0, $
        xstyle=1,ystyle=2,xtitle = 'Distance (cm)', ytitle = 'B!D0!N (rad)', $
        XCHARSIZE = 1.2, YCHARSIZE = 1.2, CHARTHICK = 1.2, $
        THICK = 1.2, XTHICK=1.2, YTHICK =1.2, $
        YTICKLEN=0.02, XTICKLEN=0.04, $
        title=title1
        oplot, r,yfit,linestyle=2, color = 0
endif else $
if (plot_num eq 99) then begin
        plot, r,phase_map,xrange=[MIN(r),MAX(r)], color = 0, $
        XCHARSIZE = 1.2, YCHARSIZE = 1.2, CHARTHICK = 1.2, $
        xstyle=1,ystyle=2,xtitle = 'Distance (cm)', ytitle = 'B!D0!N (rad)', $
        THICK = 1.2, XTHICK=1.2, YTHICK =1.2, $
        YTICKLEN=0.02, XTICKLEN=0.04, $
        title=title1
        oplot, r,yfit,linestyle=2, color = 0
endif

count = count +1

RETURN
END

;;;;;;;;;;;;;;;;;;;;;;;;;;;;;;;;;;;;;;;;;;;;;;;;;;;;;;;;;;;;;;;;;;;;;;;;;;;;;;

PRO read_data,data_dir,file,fov,bar_length,read_sizei,read_size,fspace,sw
;PRO read_data, file,read_size,fspace,rspace,ispace,phase
;IDL image reconstruction program
;by Brian Wowk, Sept. 1995
;Modified by S.B. King Dec/97 for reading 1-D FID-image projections
;Reconstructs images
;from Bruker fid files

path = '/usr/people/king/3t/data/'
dir = data_dir+'/'
data = '/fid'
```

```
if (file lt 10) then file= string(format='(i1)',file)
if (file gt 9 and file lt 100) then file= string(format='(i2)',file)
if (file ge 100) then file= string(format='(i3)',file)

if keyword_set(verbose) then $
    message, /informational, /noname, 'Reading ' + file
name = path+dir+file+data
openr, unit, path+dir+file+data, /get_lun
fid = lonarr(2*read_sizei)
readu, unit, fid
byteorder, fid, /lswap
free_lun, unit

; form the data into complex pairs
;
raw_fid = make_array(read_sizei, /complex)
  for i = 0, read_sizei-1 do $
    raw_fid(i) = complex(fid(2*i),fid(2*i+1))

;********** do a baseline correction ******************************
kr=float(raw_fid)
meankr = total(kr(read_size-10:read_size-1)) / 10.0
ki=IMAGINARY(raw_fid)                          ;imaginary part of k space
meanki = total(ki(read_size-10:read_size-1)) / 10.0
kspace = raw_fid
kspace = kspace-complex(meankr,meanki)
raw_fid = kspace
;********** end baseline correction ******************************

;***************** zero fill to read_size*nzero *************************
nzero = 1
read_size2 = read_sizei*nzero
raw_fid2 = make_array(read_size2, /complex)
temp = read_size2/2-read_sizei/2
;help, temp
;print, temp
;print, 896
;plot, abs(raw_fid)
for i = 0, read_size2/2-read_sizei/2-1 do $
          raw_fid2(i) = 0.0
for i = read_size2/2-read_sizei/2, read_size2/2+read_sizei/2-1 do $
          raw_fid2(i) = raw_fid(i-temp)
for i = read_size2/2+read_sizei/2, read_size2-1 do $
          raw_fid2(i) = 0.0

read_size = read_size2
raw_fid = raw_fid2
;********************** end zero filling ********************************

;************ Noise Reduction :  ***********************
; Filter #1: Gaussian
index = findgen(read_size) - float(read_size/2)
filter1 = EXP(-!pi*(index*index)/float(sw*sw))

; Filter #2 : Bandpass
index2= findgen(read_size)
center = read_size/2
filt_width = sw/2
if (sw le 50) then slope_width = sw/10 $
else slope_width = 5
filter2 = (1+EXP(-filt_width/slope_width))/(1+EXP((ABS(index2-center)-filt_width)/slope_width))
```

```
;**** Toggle filtering with " ; " infront of next line ****************
filter = filter2
raw_fid = raw_fid*filter
; ********** end Noise reduction ************************************

kift = COMPLEXARR(read_size)
lkift = COMPLEXARR(read_size*2)
lki = FLTARR(read_size)
kr=float(raw_fid)
ki=IMAGINARY(raw_fid)                        ;imaginary part of k space
kspace = raw_fid

;********** correction for qseq ADC mode ****************************

          kift=FFT(ki(*),1)              ;FT of a ki line
          lkift(*)=0.0
          lkift(0:(read_size/2)-1)=kift(0:(read_size/2)-1)
          lkift(read_size*3/2:(read_size*2)-1)=kift(read_size/2:read_size-1)          ;zero-padded expansion
          lki=FFT(lkift,-1)              ;FT back to larger size
          lki=SHIFT(lki,1)               ;shift to get sinc interp
          ki(*)=lki(INDGEN(read_size)*2)*2    ;interp values back to ki
          kspace=COMPLEX(kr,ki)

;*****************************************************

fspace = m1dfft(kspace)
fspace = reverse(fspace)


res = fov/read_size
bar_pts = ROUND(bar_length/res)              ;nearest integer
bar_length = bar_pts*res
r = res*(findgen(bar_pts) - float(bar_pts/2))

roi = make_array(bar_pts, /complex)

for i = 0, bar_pts-1 do begin
   roi(i) = fspace(read_size/2-bar_pts/2+i)
endfor

RETURN
END

;;;;;;;;;;;;;;;;;;;;;;;;;;;;;;;;;;;;;;;;;;;;;;;;;;;;;;;;;;;;;;;;;;;;;;;;

PRO unwrap, image, result
;
; program to unwrap a 1D phase profile
;
check = size(image)
;--------------1D input-----------------
if (check(0) eq 1) then begin
xsize = check(1)
mask = make_array(xsize, /int)
mask(*) = 0
;
; start with a line along x
;
for x = xsize/2+1, xsize-1 do begin
  diff = round((image(x)-image(x-1))/(2.0*!pi))
  mask(x) = mask(x-1) - diff
endfor
```

```
for x = xsize/2-1, 0, -1 do begin
  diff = round((image(x)-image(x+1))/(2.0*!pi))
  mask(x) = mask(x+1) - diff
endfor
endif
result = image + float(mask)*2.0*!pi

RETURN
END
```